CORA Cork Open Research Archive
Cartlann Taighde Oscailte Chorcaí

Title	The design of sensor interface circuits for electrochemical impedance spectroscopy
Authors	Wang, Zhongzheng
Publication date	2025
Original Citation	Wang, Z. 2025. The design of sensor interface circuits for electrochemical impedance spectroscopy. PhD Thesis, University College Cork.
Type of publication	Doctoral thesis
Rights	© 2025, Zhongzheng Wang. - https://creativecommons.org/licenses/by-nc/4.0/
Download date	2026-11-15 17:32:54
Item downloaded from	https://hdl.handle.net/10468/18412

UCC
University College Cork, Ireland
Coláiste na hOllscoile Corcaigh

The Design of Sensor Interface Circuits for Electrochemical Impedance Spectroscopy

A thesis presented to the

National University of Ireland, Cork

for the degree of

Doctor of Philosophy

by

Zhongzheng Wang

Head of Department: Prof. Liam Marnane

Advisor: Dr. Gerardo Salgado

Supervisors: Dr. Daniel O'Hare, Dr. Ivan O' Connell (external)

and Prof. Alan O'Riordan

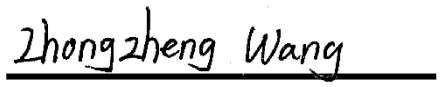
Tyndall National Institute,

National University of Ireland, Cork

April, 2025

Declaration

"This is to certify that the work I am submitting is my own and has not been submitted for another degree, either at University College Cork or elsewhere. All external references and sources are clearly acknowledged and identified within the contents. I have read and understood the regulations of University College Cork concerning plagiarism and intellectual property."



Zhongzheng Wang
April, 2025

Abstract

Electrochemical Impedance Spectroscopy (EIS) has gained attention in biomedical applications—such as DNA, antigen–antibody, and virus detection—due to its label-free nature and high sensitivity. The development of EIS circuits with low power consumption, reduced complexity, and faster measurement times has been a particularly active area of research. However, the lengthy measurement times and the complexity of traditional EIS systems limit their adoption in real-time, portable, and low-cost point-of-care (PoC) applications. In addition, conventional RC-based equivalent AC impedance electrochemical sensor models, namely, models consisting of a resistor and a capacitor in parallel structure, cannot accurately reflect realistic sensor behavior; therefore, they do not support essential simulation analyses (e.g., transient, DC sweep, or DC operating point) and fail to facilitate accurate EIS sensor interface design.

To address these challenges, this research introduces a dynamic model of an Ultra-Microband (UMB) sensor, implemented in Verilog-A, and proposes a fast, high-accuracy methodology for conducting EIS based on the Fast Fourier Transform (FFT). This approach aims to fulfill the requirements of portable, real-time, label-free EIS biomedical detection.

The work begins by reviewing fundamental electrochemical principles and examining the electrode–electrolyte interface, represented by the Randles model. A static three-electrode small-signal impedance model of the UMB sensor is then analyzed to illustrate its application in small-signal scenarios such as EIS, thereby bridging the gap between

electrochemists and electronic engineers. Subsequently, a dynamic model of the UMB sensor is developed and implemented in Verilog-A, enabling comprehensive simulations—such as AC stability, AC sweep, transient, and DC sweep—within Electronic Design Automation (EDA) tools like Cadence Spectre. This model thus captures more realistic sensor behavior and enhances design accuracy and robustness.

Finally, a square-wave-based EIS approach is proposed by identifying the conditions under which the UMB sensor behaves as a Linear Time-Invariant (LTI) system. A circuit comprising a control amplifier and a Trans-Impedance Amplifier (TIA) is designed and fabricated in a 65 nm CMOS process to validate its feasibility for on-chip integration. The proposed square-wave EIS shortens the measurement time by 91.7% across frequencies ranging from 0.5 Hz to 500 Hz, with only a 2.73% average Mean Absolute Percentage Error (MAPE) compared to a commercial instrument (AutoLab). Tests using five premodified electrodes with four different concentrations of Ferrocene Carboxylic Acid (FcCOOH) demonstrate that this method is suitable for portable, real-time EIS biomedical detection and related applications.

Acknowledgements

From March 2020 until now, over five years have slipped by. These five years feel like a whole different era: we've gone through pandemic lockdowns, academic confusion and pressure, a deep sense of homesickness, countless late-night study sessions, and all-nighters. But in that time, I've also learned resilience, a better way to tackle problems, and stronger time and stress management skills. I feel incredibly fortunate to be at the final stop of this journey.

First, I'd like to thank my father and mother. I come from an ordinary family without much wealth, and they've toiled and saved their whole lives to give me the chance to embark on—and complete—this journey. They've always stayed optimistic and encouraged me, supporting every decision I made. Their understanding and love gave me the strength to overcome challenges and keep moving forward. In many ways, it wasn't just me who completed this stage of study—it was all three of us, together, conquering every obstacle along the way.

Next, I want to thank my supervisor, Dr. Daniel O'Hare. His patience, understanding, and generosity gave me the space I needed to keep pushing forward and thinking critically. Whether it was the anxiety I felt at the end of 2022 when my previous advisor left, or the uncertainty and pressure that came after, Danny was always there with encouragement and empathy, helping me navigate every hurdle. He's truly an amazing mentor—almost more like a friend. I'm also really grateful that in 2024, we got to travel to China together. Even though time was tight and we could only visit a few spots, I'll always cherish our

photos on the Great Wall and with the Terracotta Warriors. Those moments will be precious memories for a lifetime. I hope someday we can meet again, whether in China or somewhere else around the world, to explore even more wonderful sights.

I'd also like to thank my first PhD advisor, Dr. Ivan O'Connell, for giving me so much practical advice and guidance on my studies, work, and even on life itself—especially back when I was still a bit of a naive student. You patiently showed me how the world really works, and those insights were invaluable then and remain so now.

I want to thank my advisor, Prof. Alan O'Riordan. You always give such a firm handshake—it really hurts! I later found out you practice karate. I hope one day you can come to China to try out some Chinese kung fu! Thank you so much for supporting me during my PhD. I know those sensors are expensive, and I was breaking at least two a day—but that definitely wasn't my fault!

I'm also grateful to John Morrissey, the head of MCCI, for helping me after Ivan left, and to my external advisor, Alan Bannon, my advisor, Gerardo Salgado, and my current manager, Paraic Brannick. Thank you for taking time out of your busy schedules to guide me in my research. My thanks go as well to all my colleagues at MCCI.

I'd like to express my appreciation to my friends—Han Shao, Javier, Minda Wen, Madhan Venkatesh, Cian O'Donnell, Jaekyum Lee—and everyone else I worked with at MCCI. You've all made my PhD life so much richer. I've learned so much from you, and I wish you all the very best for the future. I also want to thank the UCC School of Music for letting me practice piano there. I miss those hours I spent absorbed in the music rooms.

Finally, I'd like to thank my piano teacher, Maestro David Syme—your playing is always so moving and immersive. Studying piano under your guidance brought sunshine and excitement to my PhD journey.

To everyone who has helped and supported me along the way—thank you.

Contents

Abstract 1

Acknowledgements 3

Contents 6

List of Figures 10

List of Tables 15

List of Acronyms 16

1. Introduction 19

2. Electrochemical Sensors, Systems and Measurement Techniques 23

2.1. Chemical Sensors and Electrochemical Sensors 23

2.2. Ultra-microband Electrochemical sensors 25

2.3. Electrochemical Sensor System 27

2.3.1. Single-electrode system 27

2.3.2. Two-electrode Electrochemical System 28

2.3.3. Three-electrode Electrochemical System 29

2.4. Electrochemical Measurement Techniques 31

2.4.1. Potentiometry 31

2.4.2. Voltammetry 33

2.4.3. Amperometry Measurement 35

2.4.4. Electrochemical Impedance Spectroscopy 35

2.5. Conclusion 38

3. Equivalent Small-signal Impedance Models for Electrochemical Ultra-microband Sensor-based Integrated System Design 39

3.1. Equivalent Small-signal Models for Single Electrode – Randles Model 40

3.1.1. The Double-layer at the Electrode-electrolyte interface 40

3.1.2. Modelling of the electrode-electrolyte interface 42

3.1.3. The Randles Model 45

3.2. Model of the two-electrode system 46

3.3. Model of a three-electrode System 47

3.4. Application of the model in small-signal analysis for typical electrochemical sensor interfaces 50

3.4.1. Op-Amp and TIA-Based Potentiostat 52

3.4.2. Current-Mirror-Based Potentiostat 55

3.5. Conclusion 58

4. A Fast Electrochemical Impedance Spectroscopy with A Square Wave as Excitation Signal for Impedance-based Biomedical Applications 59

4.1. Introduction 59

4.2. Models and the Time-Invariant Linear Region of UMB Electrode Sensors 63

4.2.1. UMB Sensors and their Diffusion Mechanisms 63

4.2.2. Charge-transfer Rate Model of UMB Electrode Sensors and its Small-signal Linear Approximation 65

4.2.3. Practical Time-Invariant Linear Region of UMB Electrode Sensors for EIS 71

4.3. The Proposed Square Wave EIS and its Circuit Implementation 74

4.3.1. Proposed Square-wave EIS via an FFT 74

4.3.2. Verilog-A Model of UMB Sensor for Circuit Design 76

4.3.3. Design of the Amplifier 80

4.3.4. Design of TIA 82

4.4. Experimental Results 89

4.4.1. Electrical Validation of the Chip with Dummy Sensor 89

4.4.2. The Pre-modification of the UMB Electrodes 91

4.4.3. Electrochemical Validation of the Proposed Square-wave EIS with Pre-deposited UMB Electrodes 96

4.5. Error Evaluation 101

5.6. Conclusion 104

5. Discussion and Future Work 105

5.1. Contributions/Outputs of this Work 105

5.2. The Applicability of the Proposed Square Wave-based EIS 106

5.3. The Impact of the Proposed Verilog-A model. 108

5.4. The Required Specification of the Amplifier and TIA 108

6. Reference 110

7. Appendices 129

7.1. MATLAB Code for Computing Impedance 129

7.2. Measurement PCB Schematics and Layouts 131

7.2.1. Chip Measurement PCB 131

7.2.2. Dummy Sensor PCB 134

7.2.3. Mini-HDMI UMB Sensor PCB Adaptor 136

7.2.4. Mini-HDMI to Micro SD Adaptor 139

List of Figures

Figure. 2.1 The indicated diagram of the receptor and transducer components of a chemical sensor 24

Figure. 2.2 A typical configuration of a three-electrode electrochemical sensor..... 25

Figure 2.3. The UMB electrode electrochemical sensor with Mini HDMI compatible pin-outs, and the microscopic photo of the working electrode 26

Figure 2.4. The single-electrode system: sensing or applying an electrode potential, where a probe of an instrument serving as a CE. 27

Figure 2.5. The two-electrode system: sensing or applying an electrode potential, where the probe is replaced with an RE, providing a constant reference electrode potential. .. 28

Figure. 2.6. The three-electrode sensor system, with a CE for conducting the current. . 30

Figure. 2.7. The indicated applied electrode potential for one cycle of CV scan, and a typical resultant shape of sensor current with CV. 33

Figure. 2.8. The EIS for an RC complex impedance. 37

Figure 2.9. The Nyquist diagram of a RC complex impedance. 38

Figure 3.1. The electrode-electrolyte interface for a single electrode..... 40

Figure 3.2. The electrode-electrolyte interface and the electrode potential. 41

Figure 3.3 The equivalent double-layer capacitor model at the electrode-electrolyte interface..... 42

Figure 3.4. The equivalent model of an electrode-electrolyte interface: (a) an equivalent model with a capacitor and faradaic impedance in parallel; (b) equivalent with faradaic impedance represented by a charge-transfer resistance and the WI..... 43

Figure. 3.5. Equivalent Small-signal Models for Single Electrode – Randles Model 45

Figure 3.6. The model of the two-electrode sensor system, with a DC voltage source representing the reference electrode potential..... 46

Figure 3.7 The approximated simplified small-signal model for a two-electrode system with tiny current. 47

Figure 3.8. The equivalent small-signal model of a three-electrode electrochemical sensor, with the comparison of sensor electrode-electrolyte interface of each electrode. 48

Figure. 3.9 The AC impedance model of UMB three-electrode sensor system for electrochemical sensor interface design. 49

Figure 3.10. The diagram of a three-electrode electrochemical system. 51

Figure. 3.11. Op-amp and TIA-based potentiostat 51

Figure 3.12 A two-stage folded-cascode amplifier [72] 52

Figure. 3.13. The rail-to-rail folded-cascode with floating class AB controlled output stage [78] 52

Figure. 3.14. The equivalent model for stability analysis of a TIA 53

Figure 3.15 The stability analysis for TIA 54

Figure 3.16 The current mirror-based potentiostat and current-to-frequency converter. 55

Figure 3.17. The equivalent small-signal model for stability analysis [83]. 56

Figure 3.18. The stability analysis for current-mirror based potentiostat. 57

Figure 4.1 The overall diagram that indicates the contribution of this work 61

Figure 4.2. (a). A silicon wafer substrate with eight individual UMB electrodes. (b). The measurement results of CV with an UMB electrode sensor in 1 mM FcCOOH dissolved in 10 mM PBS at 25° C, SR = 50 mV/s. 64

Figure 4.3. The measurement results of CV for one cycle with an UMB electrode sensor in 1 mM FcCOOH dissolved in 10 mM PBS at 25° C, SR = 0.001 V/s, and the Model predicted data. 68

Figure 4.4. The CV measurement result under experimental conditions of 1 mM FcCOOH dissolved in 10 mM PBS at 25° C, with a SR of 50 mV/s. 70

Figure 4.5. The determination of the conditions where Rct is an LTI component. (a). The conductance of the UMB electrode sensor is potential-dependent. (b). Determination of the practical time-invariant linear region. 71

Figure 4.6. EIS results of UMB electrode with AC amplitude increasing from 5 mV to 100 mV, with an incremental step of 5 mV at 0.1 V DC potential..... 72

Figure 4.7. The system level diagram of the proposed square-wave EIS. 74

Figure 4.8. The block diagram of the circuit for the proposed square-wave EIS. 75

Figure 4.9. Models of electrochemical sensor electrode-electrolyte interfaces: (a). Randle's Model. (b). Randle's Model with Warburg Impedance omitted. (c). Model with CPE, where Rct is dynamic. 77

Figure 4.10. EIS measurement results with an amplitude of 10 mV over a frequency range of 0.1 Hz to 100 kHz, vs. Verilog-A model-predicted results from Cadence, on the DC biases of 0.105 V, 0.125 V, 0.135 V, 0.155 V, 0.175 V, 0.185 V and 0.205 V over the same frequency range..... 78

Figure 4.11. PMOS-input folded-cascode amplifier topology, complemented by a CS output stage with Miller compensation. 81

Figure 4.12. (a). Stability analysis, and (b). input-referred voltage noise density spectrum and the noise source contribution of the in-band integrated noise. 82

Figure 4.13. The equivalent models for TIA design. (a). The simplified equivalent model with noise source contributions, and (b). the equivalent model for analyzing stability and bandwidth. 83

Figure 4.14. (a). The SNR analysis of TIA at a DC bias of 0.125 V, 0.135 V, 0.155 V, 0.175 V and 0.185 V. (b). The stability analysis of TIA with overcompensation. Note that the transimpedance has a unit of Ohm. 84

Figure 4.15. The noise analysis considering the FFT demodulation; (a). the simulated time-domain response of the Verilog-A model, with a DC potential ($VWE - VRE$) of 155 mV, and an AC amplitude of 40 mV, and (b). the FFT results of the current, by converting the TIA output with an Rf of 4 $MOhm$. 85

Figure 4.16. The measurement setup and the die micrograph: (a). The test setup, and (b). the die micrograph. 89

Figure 4.17. The PCB setup for electrical validation, with an Rct = 50 MOhm, and a Ceq = 1 nF. 90

Figure 4.18. The time-domain results of the sensor input and TIA output for a dummy sensor, with an Rct = 50 MOhm, and a Ceq =1 nF. 91

Figure 4.19. The FFT results of the measured square-wave EIS with a dummy sensor: (a). the FFT results of the applied potential at RE, and (b). the FFT results of the current converted from TIA output. 92

Figure 4.20. The chip-tested results of square-wave EIS and simulated results of a dummy sensor, with an $Rct = 50$ MOhm, and a $Ceq = 1$ nF. 93

Figure 4.21. Microscopic images of five electrodes with different deposited thicknesses of gold. 93

Figure 4.22. The CV results performed by AutoLab in (a). 1 mM FcCOOH, (b). 2 mM FcCOOH, (c). 3 mM FcCOOH, and (d). 4 mM FcCOOH, in a 10 mM PBS supporting electrolyte at 25°, with a SR of 50 mV/s from -0.1 V to 0.4 V, showing different electrode characteristics for the electrochemical validation. 94

Figure 4.23. The EIS results performed by AutoLab in (a). 1 mM FcCOOH, (b). 2 mM FcCOOH, (c). 3 mM FcCOOH, and (d). 4 mM FcCOOH, in a 10 mM PBS supporting95

Figure 4.24 The PCB setup for chemistry test with deposited UMB electrodes. 96

Figure 4.25. The chip-tested results of CV across (a). 1 mM FcCOOH, (b). 2 mM FcCOOH, (c). 3 mM FcCOOH, and (d). 4 mM FcCOOH, in a 10 mM PBS supporting electrolyte at 25°, with a SR of 50 mV/s for electrode potential from -0.1 V to 0.4 V. The results shows that the UMB sensor is working as expected..... 97

Figure 4.26. The determination of AC and DC conditions for square-wave EIS across a). 1 mM FcCOOH, b). 2 mM FcCOOH, c). 3 mM FcCOOH, and d). 4 mM FcCOOH, in a 10 mM PBS supporting electrolyte at 25°. The DC bias of the sensor is chosen where the conductance of the sensor reaches minimum, namely, the half potential, and the AC amplitude is chosen to be 40 mV as mentioned in Section 4.2.3, where the sensor working in a linear region. 98

Figure 4.27. The time-domain results of the sensor input and TIA output for E1. 99

Figure 4.28. The FFT results of the chip-measured square-wave EIS with E1 in 1 - 4 mM FcCOOH: (a). the FFT results of the applied potential at RE, and (b). the FFT results of the current converted from the TIA output..... 100

Figure 4.29. The comparison of EIS results of the square wave EIS, the traditional EIS performed by AutoLab, and the EIS optimized fitted model. 101

List of Tables

Table I. MAPE of the impedance with scanning AC amplitude 73

[113]Table II. The absolute percentage error 80

Table III. The operation regions of transistors 82

Table IV. Error evaluation 103

Table V. Comparison with relevant published works 104

List of Acronyms

EIS: Electrochemical Impedance Spectroscopy

PoC: Point-of-Care

UMB: Ultra-Microband

CPE: Constant Phase Element

MPD: Magnitude-Phase Detection

SCE: Saturated Calomel Electrode

FFT: Fast Fourier Transform

DACs: Digital-to-Analog Converters

LTI: Linear Time-Invariant

TIA: Trans-Impedance Amplifier

MAPE: Mean Absolute Percentage Error

PM: Potentiometry

VM: Voltammetry

AM: Amperometry

CV: Cyclic Voltammetry

CA: Chrono Amperometry

WE: Working Electrode

RE: Reference Electrode

CE: Counter Electrode

SR: Scan Rate

FT: Fourier Transform

IHP: Inner Helmholtz Plane

OHP: Outer Helmholtz Plane

WI: Warburg Impedance

DDS: Direct Digital Synthesis

SNR: Signal to Noise Ratio

PBS: Phosphate Buffered Saline

CAD: Computer-Aided Design

AAA: Adaptive Antoulas–Anderson

MORA: Modified Oustaloup Recursive Approximation

APE: Absolute Percentage Errors

CS: Common Source

GBW: Gain Bandwidth

UGB: Unit Gain Bandwidth

ADC: Analog-to-Digital Converter

Chapter 1

1. Introduction

Electrochemical sensors are devices that transduce chemical or biochemical information—ranging from the concentration of a specific analyte to the presence of particular chemical species—into an electrical signal. By measuring electrode current, potential, or impedance, electrochemical sensors provide insights into reaction kinetics, analyte concentrations, and charge-transfer dynamics, which enables the quantitative and/or qualitative assessment of target analytes, such as glucose concentration [1, 2] or the presence of certain viruses [3, 4]. Owing to their high sensitivity and rapid response [5–8], electrochemical sensors have been widely applied in areas such as biomedical detection [9], environmental monitoring [10], and food quality [11].

Among the various electrochemical measurement techniques—including voltammetry, amperometry, and potentiometry—Electrochemical Impedance Spectroscopy (EIS) has gained particular attention in the biomedical domain. EIS enables sensitive, label-free characterization of biological interactions occurring at the electrode interface. By monitoring impedance changes induced by binding events—such as antigen–antibody interactions [12, 13], DNA hybridization [14], or cell attachment [15, 16]—biosensors using EIS can rapidly detect critical biomarkers in complex biological media (e.g., blood [17], or saliva [18]), making this technique especially valuable for biomedical diagnostics.

Owing to advances in CMOS technology, handheld EIS measurement devices have become feasible and are widely used in biomedical applications, including disease detection and point-of-care (PoC) diagnostics [19, 20]. However, the lengthy measurement time required to obtain a complete frequency sweep (spanning from millihertz to a few kilohertz), coupled with the circuit complexity of conventional EIS methodologies and the associated increase in cost [21], has hindered the deployment of EIS in real-time, low-cost, portable, or PoC devices.

This thesis aims to address these challenges by designing an interface for EIS measurement that utilizes an UMB electrochemical sensor, focusing on both reducing circuit complexity and shortening measurement duration. Several research questions have motivated this work:

1. **Unclear Model Topologies and Explanations (up to 2020):** While various studies [22–25] have proposed different electrochemical sensor models for EIS circuit design, they often provide limited explanations regarding the underlying principles. A lack of overlap in chemistry and electronics knowledge complicates collaboration between chemists and electronics engineers in developing new sensor interfaces.

2. **Limitations of the AC Impedance Model:** The traditional AC impedance model [26] represents the electrode–electrolyte interface with electrical components and supports small-signal analyses (e.g., AC, stability, and noise). However, it does not capture large-signal behaviors—such as transient or DC responses—thereby

complicating the accurate design of sensor interface ICs, including the determination of bandwidth, stability, and the common-mode range. Moreover, the double-layer capacitor used in models, though effective in describing charge accumulation at the electrode surface, does not account for constant phase element (CPE) behavior, introducing potential inaccuracies in circuit design.

3. **Lengthy EIS Circuit Readout Techniques:** Techniques such as I/Q detection or Magnitude-Phase Detection (MPD) can achieve high accuracy in noisy environments, owing to the lock-in amplifier [27–31]. However, the required frequency-sweep steps and complex circuitry lead to prolonged measurement times, rendering these methods unsuitable for low-cost, real-time EIS detection. Although Fast Fourier Transform (FFT)-based techniques can shorten measurement time by applying a wideband signal [32–37], they demand high-precision Digital-to-Analog Converters (DACs) for signal generation, thereby increasing circuit complexity and cost.

To overcome these limitations, this work first investigates the three-electrode AC impedance model of an UMB sensor to provide a more comprehensive understanding of its behavior. A dynamic model is then developed and implemented in Verilog-A, enabling broader simulation capabilities—including small-signal, large-signal, and DC analyses—by incorporating both a fitted charge-transfer resistance and an approximation of the CPE. This approach yields a more realistic representation of sensor behavior for circuit analysis and design. Finally, by identifying a linear region in which the sensor functions as an LTI

system, this thesis proposes a square-wave EIS method that circumvents the need for a high-precision DAC to generate wideband signals.

Comparisons with a commercial electrochemical instrument (AutoLab) using five premodified electrodes across four different concentrations of ferrocene carboxylic acid (FcCOOH) demonstrate that the proposed square-wave EIS approach shortens the measurement time by 91.7% over a frequency sweep from 0.5 Hz to 500 Hz, while obtaining only a 2.73% average Mean Absolute Percentage Error (MAPE). These results indicate that the proposed method is well-suited for portable, real-time EIS biomedical detection and related applications.

Chapter 2

2. Electrochemical Sensors, Systems and Measurement Techniques

This chapter reviews fundamental concepts of electrochemical sensors, including UMB electrode sensors, and examines both two-electrode and three-electrode electrochemical systems. It also introduces major electrochemical measurement techniques—such as potentiometry (PM), voltammetry (VM), amperometry (AM), and EIS—with the aim of providing necessary background information. A portion of the material in this chapter was previously published as a book chapter in *Biomedical Electronics, Noise Shaping ADCs, and Frequency References* (DOI: https://doi.org/10.1007/978-3-031-28912-5_5)

2.1. Chemical Sensors and Electrochemical Sensors

A chemical sensor is a device that converts chemical information into electrical signals, such as voltage or current. As illustrated in Figure 2.1, a typical chemical sensor comprises two main components: a receptor and a transducer. In the receptor section, the chemical information is transformed into a form of energy (e.g., electrical charge) that can be detected by the transducer. The receptor often exhibits selectivity toward specific chemical species, thereby ensuring that the sensor responds primarily to the analyte of interest. In the transducer section, the energy conveyed from the receptor is converted into

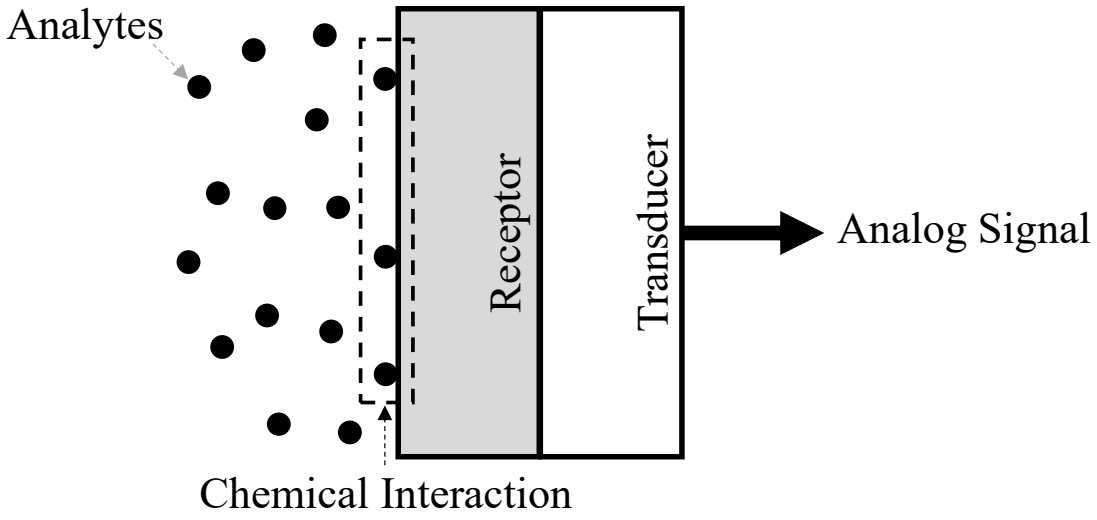


Figure. 2.1 The indicated diagram of the receptor and transducer components of a chemical sensor

an analog signal, which is subsequently digitized for quantitative analysis. Typically, the transducer itself does not exhibit selectivity toward particular species.

By integrating selective receptors with reliable transducers, chemical sensors enable rapid, accurate, and cost-effective analyses across diverse applications. For instance, breathalyzers [38] measure blood alcohol content by detecting alcohol levels in exhaled breath. Carbon monoxide sensors provide critical safety alerts by measuring CO concentrations in residential and industrial settings [39], and gas sensors [40], more generally, facilitate air quality monitoring and control.

Distinct from general chemical sensors, electrochemical sensors constitute a specialized category in which the transducer is an electrode typically immersed in a test medium (liquid or gas) to detect specific chemical reactions. Their primary distinction lies in the ability to establish and analyze quantitative relationships between electrical signals

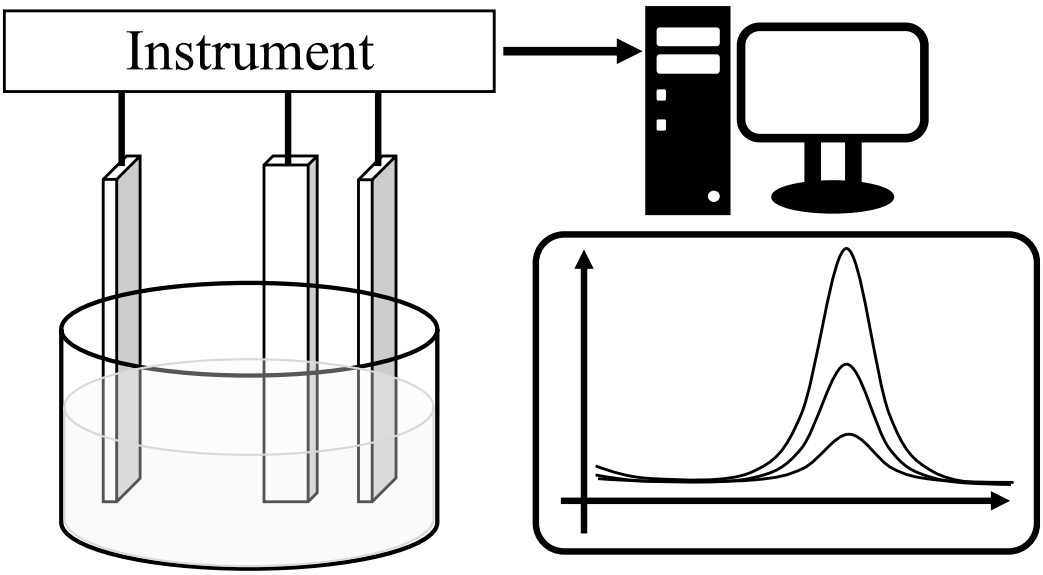


Figure. 2.2 A typical configuration of a three-electrode electrochemical sensor

and chemical processes, often with the aid of electronic devices such as a computer or a microcontroller, as illustrated in Figure 2.2.

Electrochemical sensors (and their associated systems) support multiple measurement techniques—including Cyclic Voltammetry (CV), Chrono Amperometry (CA), and EIS—thereby enabling precise monitoring of electron-transfer kinetics, current–potential relationships, and interfacial properties at the electrode surface, respectively.

2.2. Ultra-microband Electrochemical sensors

The electrochemical sensors used in this work are UMB sensors manufactured at Tyndall National Institute, whose electrodes are micro-scale band-shaped, often with widths on the order of micrometers to tens of micrometers. The UMB sensors are manufactured on a silicon wafer substrate where a ~300nm silicon dioxide layer is

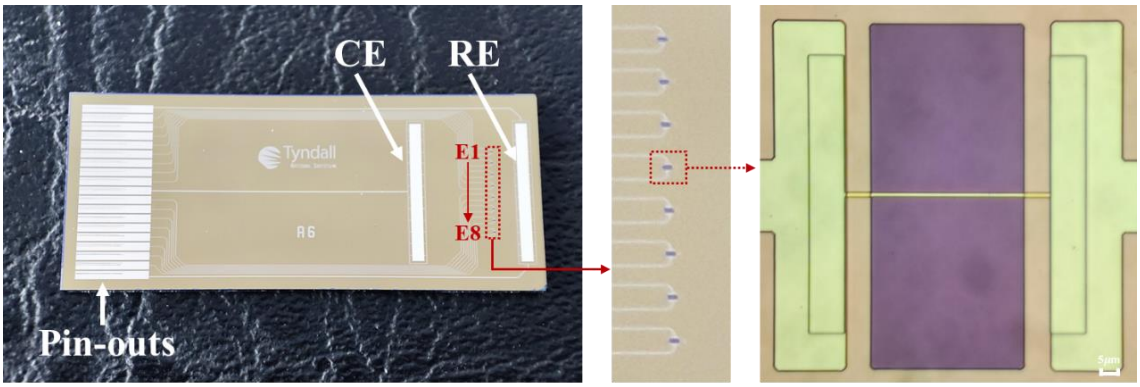


Figure 2.3. The UMB electrode electrochemical sensor with Counter Electrode (CE), Reference Electrode (RE), Mini HDMI compatible pin-outs, and the microscopic photo of the working electrode.

thermally grown on the wafer. The UMB Working Electrode (WE) is fabricated via optical lithography, metal evaporation (Ti 10 nm /Au 150 nm), and lift-off processes, yielding stacked metallic Ti/Au microbands (1 µm width, 150 nm height, 45 µm length); then the lithography and metal deposition (Ti 10 nm /Au 100nm /Ti 10nm /Pt 100 nm) are performed to create the chip pin-outs, interconnection tracks, Reference Electrodes (RE) (500 µm x 10 mm) and Counter Electrodes (CE) (500 µm x 10 mm). Finally, the SiN_X passivation layer is deposited by Pressure Enhanced Chemical Vapor Deposition (PECVD) and selectively etched to expose electrode areas and the pin-outs. The chip contains eight individual UMB electrodes, each of which has an active area of 5.85e-11 m^2, and a 19-pin Mini HDMI-compatible pin-out is integrated at the edge of the chip, allowing for electrical connections to external electronics, as shown in Figure 2.3. A more detailed illustration of the UMB fabrication process is introduced in [41–43].

UMB electrode electrochemical sensors are currently being developed by several groups worldwide [44–47] and show numerous advantages. For example, the microscale

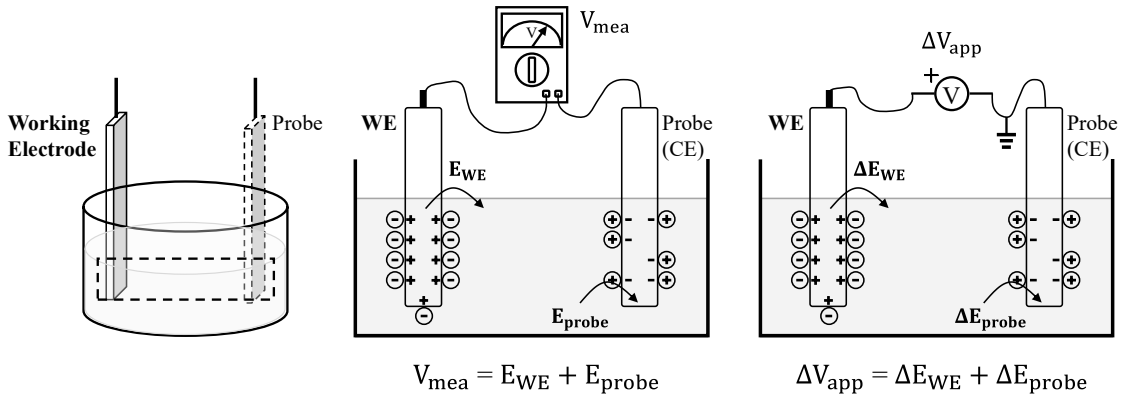


Figure 2.4. The single-electrode system: sensing or applying an electrode potential, where a probe of an instrument serving as a CE.

size electrode, as shown in Figure 2.3, promotes radial diffusion of analytes, leading to more efficient analyte transport, which results in enhanced current density, higher SNR and more stable voltammogram during an electrochemical reversible redox process [43]. Owing to the rapid mass transfer, shorter analysis time, low-volume analysis and high-speed kinetic studies become enabled, which broaden their application scope and fields.

2.3. Electrochemical Sensor System

In this section, a single electrode system is explained, building on this two-electrode system and finally three-electrode system will be introduced.

2.3.1. Single-electrode system

When measuring the potential of a single-electrode system with a voltmeter, as shown in Figure 2.4, the meter's probe effectively serves as the counter electrode. This configuration induces a potential difference between the probe surface and the bulk electrolyte. Consequently, the measured potential, V_{mea}, is expressed as in (2.1),

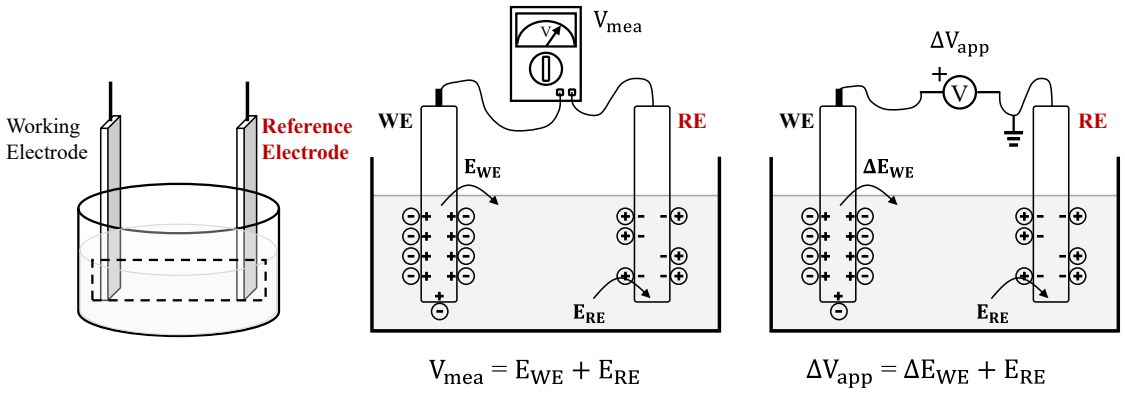


Figure 2.5. The two-electrode system: sensing or applying an electrode potential, where the probe is replaced with an RE, providing a constant reference electrode potential.

$$V_{mea} = E_{WE} + E_{probe} \tag{2.1}$$

where E_{WE} is the working electrode potential (i.e., the potential between the electrode and the electrolyte at the electrode–electrolyte interface), and E_{probe} is the probe potential (i.e., the potential across the probe and the electrolyte).

According to Equation (2.1), the electrode potential, E_{WE}, which is typically of primary interest, cannot be precisely determined because, E_{probe}, is inherently uncertain and governed by the Nernst equation [48, 49]. Furthermore, any applied potential change, ΔV_{app}, can be expressed as shown in (2.2),

$$\Delta V_{app} = \Delta E_{WE} + \Delta E_{probe}, \tag{2.2}$$

which implies that, in a single-electrode sensor system, it is neither feasible to measure the absolute potential of a single electrode nor to accurately apply a known potential change to the electrode of interest.

2.3.2. Two-electrode Electrochemical System

To address the issue of uncertain working electrode potential described previously, a RE is developed and introduced to replace the voltmeter probe, as illustrated in Figure 2.5. The electrode potential of the RE will stay constant and is determined by its material composition. In an Ag/AgCl reference electrode, for example, the electrode potential, $E_{RE,AgCL}$, is approximately 0.199 V [50]; thus, it provides a fixed reference electrode potential, which enables the control of the electrode potential change at WE, $\Delta E_{WE} = E_{WE1} - E_{WE2}$, as is expressed in (2.3):

$$\Delta V_{app} = E_{WE1} - E_{RE} - (E_{WE2} - E_{RE}) = \Delta E_{WE} \tag{2.3}$$

However, for a large current flowing through the RE, the reference electrode potential may shift as it may drive the $Ag/AgCl \rightleftharpoons Ag^{+} + Cl^{-}$ equilibrium away from Nernst conditions, adding kinetic overpotential. Consequently, two-electrode systems function reliably only if the current drawn from the RE remains minimal, limiting them to applications where the electrochemical reactions require relatively small currents.

2.3.3. Three-electrode Electrochemical System

To overcome the limitation of the two-electrode system, a CE is introduced, forming the three-electrode system together with a WE and an RE, as shown in Figure. 2.6. The CE works as an electrode sinking or sourcing all current from the WE [26], such that a negligible amount of current may leak through the RE by connecting it with a high-impedance equipment. Due to the tiny current, the potential of RE will remain constant even in the presence of large current flowing through the WE.

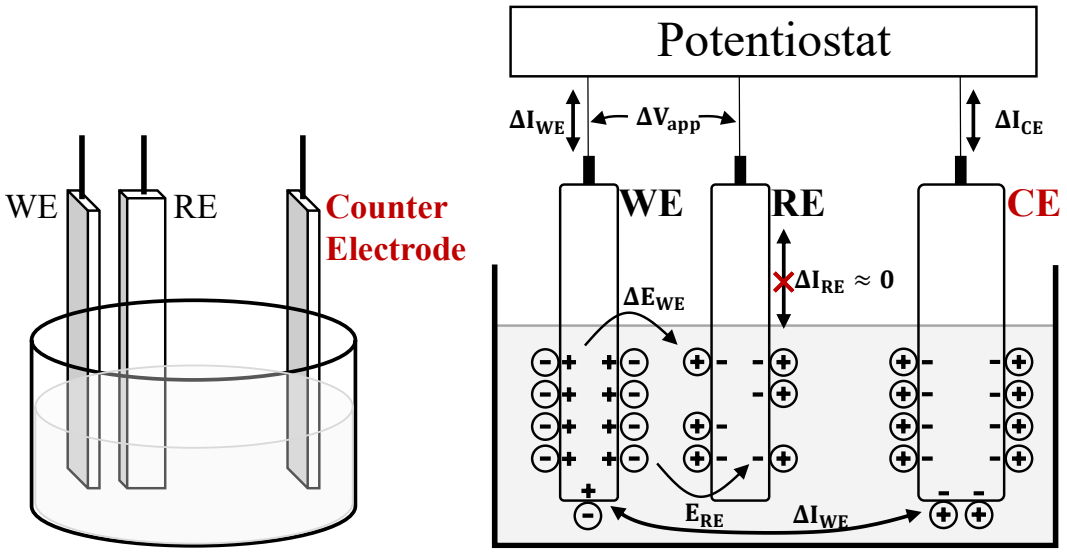


Figure. 2.6. The three-electrode sensor system, with a CE for conducting the current.

The operation of the three-electrode sensor system can be represented by (2.4), (2.5) and (2.6):

$$\Delta I_{WE} = \Delta I_{CE} \tag{2.4}$$

$$\Delta V_{app} = \Delta E_{WE} \tag{2.5}$$

$$\Delta I_{RE} \approx 0. \tag{2.6}$$

where ΔI_{WE} is the change in current of the working electrode, and ΔI_{CE} is the change in current of the counter electrode. ΔI_{RE} represents the change in current of the reference electrode.

As is the case with the two-electrode system, all potential changes are applied to the WE only, with the RE remaining at constant potential, and the relationship between the

current change, ΔI_{WE}, and voltage change, ΔE_{WE}, is quantitatively controlled, while there are fewer restrictions on the current strength.

As previously mentioned, the potential applied to RE is controlled via high impedance device known as potentiostat, which maintains the potential of the RE while restricting current flow through it, and simultaneously driving current through the CE. The potentiostat ensures precise control of the WE electrode potential, yielding both accuracy and versatility in applications such as electroanalysis, corrosion studies, and sensor development.

2.4. Electrochemical Measurement Techniques

Potentiometry, voltammetry, amperometry, and electrochemical impedance spectroscopy are four of the most common electrochemical measurement methods. This section gives an overview of these topics and more details of these techniques can be found in [51].

2.4.1. Potentiometry

Potentiometry is an electroanalytical method where the potential (voltage) between two electrodes is measured while drawing negligible current. Typically, one uses an indicator (or working) electrode that is selective to the analyte of interest, coupled with a reference electrode of known and stable potential. The indicator/working electrode is sensitive to the activity (effective concentration) of a specific ion or molecule, and the reference electrode maintains a constant potential, often via a well-defined redox couple or ionic equilibrium (e.g., the Ag/AgCl or the Saturated Calomel Electrode (SCE) [50]),

as mentioned in the previous section. In the ideal potentiometric measurement, the current flow is essentially zero, ensuring that the measured potential accurately reflects the electrochemical equilibrium at the indicator electrode.

Potentiometry relies heavily on the Nernst Equation [48, 49], as expressed in (2.7), which relates electrode potential to the activity (or concentration) of the target ion.

$$E = E^{\circ} + \frac{RT}{nF} ln\,(a) \tag{2.7}$$

Where:

E is the electrode potential;

E° is the standard electrode potential;

R is the universal gas constant ($8.314\ J \cdot mol^{-1} \cdot K^{-1}$);

T is the absolute temperature in Kelvin;

n is the number of electrons exchanged in the electrode reaction;

F is the Faraday constant ($96485\ C \cdot mol^{-1}$);

a is the activity of the ion, which can be approximated by the molar concentration of the specific ion of interest in solution at low ionic strength.

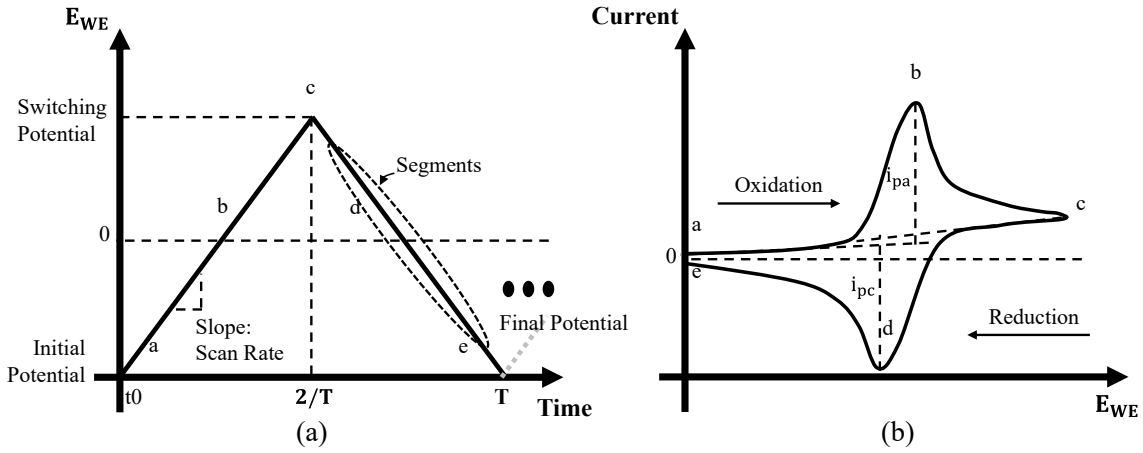


Figure. 2.7. The indicated applied electrode potential for one cycle of CV scan, and a typical resultant shape of sensor current with CV.

2.4.2. Voltammetry

Voltammetry measures the current that flows in an electrochemical cell as a function of an applied potential. Unlike potentiometry, where no current is drawn, voltammetry involves driving the system away from equilibrium by varying the electrode potential and recording the resulting current, and a three-electrode setup is commonly used as discussed in Section 2.3.3.

Cyclic voltammetry is one of the voltammetry techniques, where the potential is swept linearly from an initial potential, E_{ini}, to a switching potential, E_{sw}, with and then back to, E_{ini}, with a preset Scan Rate (SR), as is shown in Figure. 2.7(a). The SR ranges from 1 mV/sec to 50 V/sec, depending on the size of the electrode, material of the electrode, and the analyte under study, and the target of the test [51]. The SR is usually selected as a trade-off to provide a fast enough measurement while maintaining the lowest amount of acceptable charging currents.

The applied electrode potential typically ranges from -0.2V to 0.5V for UMB sensors [26, 43, 47, 51].

CV creates a voltammogram (forward and reverse sweep), providing information on redox processes, reaction kinetics, and diffusion coefficients [52–54]. In the case of a reversible redox reaction, the peak current, i_p, as is shown in Figure 2.7(b), in cyclic voltammetry is related to the analyte concentration by the Randles–Sevcik equation [55–58], as expressed in (2.8):

$$i_p = 0.4463nFAC\left(\frac{nFvD}{RT}\right)^{\frac{1}{2}} \tag{2.8}$$

Where:

A is the geometric area of the working electrode (cm^2);

C is the bulk concentration of the electroactive species in (mol/cm^3);

D is the diffusion coefficient of the electroactive species (cm^2/s);

v is the potential scan rate of the voltammetric sweep (V/s).

When reactions are kinetically controlled, the relationship between the current density j and the overpotential η is often given by the Butler–Volmer equation [51], as is expressed in (2.9):

$$j = j_0[exp\left(\frac{\alpha_a F\eta}{RT}\right) - exp\ (-\frac{\alpha_c F\eta}{RT})] \tag{2.9}$$

Where:

j_0 is the exchange current density;

α_a and α_c are the anodic and cathodic transfer coefficients;

$\eta = V_{app} - E_{eq}$ is the overpotential, the difference between the applied potential and the equilibrium potential E_{eq}.

2.4.3. Amperometry Measurement

Chronoamperometry measures the current response to a step change in the electrode potential. Unlike voltammetry, where potential is varied continuously, in chronoamperometry the potential is stepped (instantaneously, ideally) from one value to another and the resulting current is recorded over time.

When the potential is stepped such that an electroactive species is oxidized or reduced at the electrode, the current $i(t)$ decays over time as the concentration of the electroactive species at the electrode surface changes due to diffusion. For a simple diffusion-controlled reaction at a planar electrode, the current decay is described by the Cottrell equation [51, 59], as expressed in (2.10):

$$i(t) = \frac{nFAC^*}{\sqrt{\pi Dt}} \tag{2.10}$$

Where C^* is the bulk concentration of the electroactive species, D is the diffusion coefficient, and t is time after the potential step.

2.4.4. Electrochemical Impedance Spectroscopy

EIS is a frequency-domain technique that probes the dynamic response of an electrochemical system by applying small-amplitude sinusoidal perturbations, typically from 5mV to 10mV [23, 60, 61] on a chosen DC bias. The frequency of those perturbations is swept from sub-Hz to a few kHz, and the resulting current or voltage is analyzed to compute the sensor AC impedance.

To calculate the complex impedance, a time-dependent sinusoidal perturbation $v(t) = V_0 \sin(\omega t + \phi_v)$, where $\omega = 2\pi f$, is an angular frequency and ϕ_v is the initial phase, is applied as the excitation signal, the current response is expressed in (2.11):

$$i(t) = I_0 \sin(\omega t + \phi_i) \tag{2.11}$$

where ϕ_i is the phase shift introduced by the complex impedance.

Transforming to the complex plane via a Fourier Transform (FT), the impedance is computed as the ratio of the complex amplitudes, as is expressed in (2.12):

$$Z(\omega) = \frac{V(\omega)}{I(\omega)} = Z'(\omega) + jZ''(\omega) \tag{2.12}$$

where $V(\omega)$ and $I(\omega)$ are the FT of the applied perturbation, $v(t)$, and the resultant current of the complex impedance, $i(t)$, respectively. The real part, Z', represents the energy dissipation, while the imaginary part, Z'', accounts for energy storage.

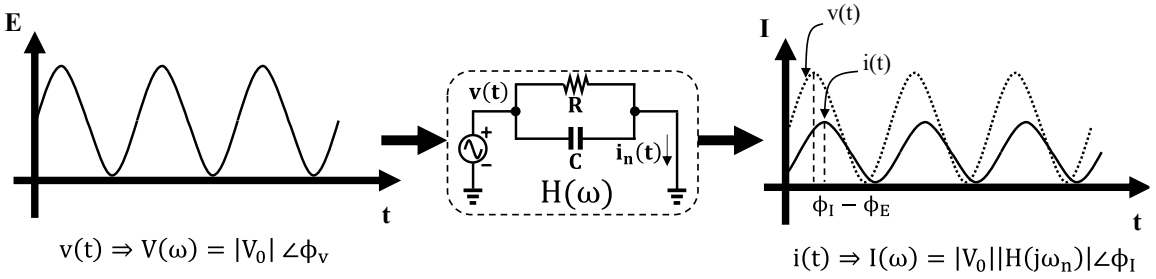


Figure. 2.8. The EIS for an RC complex impedance.

$$Z_{RC}(\omega) = \left[\frac{1}{R} + j\omega C\right]^{-1} = \frac{R}{1 + j\omega RC} = Z'(\omega) + jZ''(\omega). \tag{2.13}$$

where

$$Z'(\omega) = \frac{R}{1 + \omega^2 R^2 C^2} \tag{2.14}$$

and

$$Z''(\omega) = -\frac{\omega R^2 C}{1 + \omega^2 R^2 C^2}. \tag{2.15}$$

Considering a simple RC impedance shown in Figure 2.8, the total impedance of this network is expressed in (2.13), and the real and imaginary parts are expressed in (2.14) and (2.15), respectively.

A Nyquist plot of $Z_{RC}(\omega)$ is shown in Figure 2.9. The R and C can be readily obtained from the plot, as expressed in (2.16) and (2.17):

$$R = \frac{R}{1 + \omega^2 R^2 C^2}\Big|_{\omega \approx 0} \tag{2.16}$$

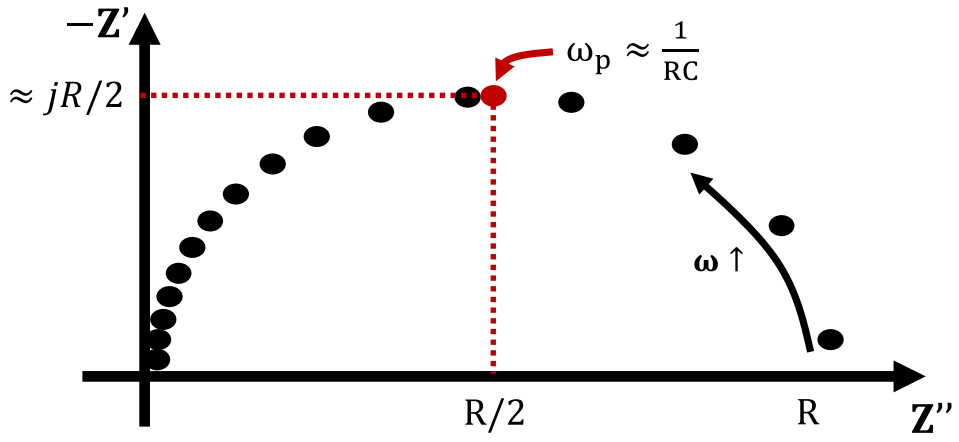


Figure 2.9. The Nyquist diagram of a RC complex impedance.

$$C \approx \frac{1}{\omega_p R} \tag{2.17}$$

As a consequence of the high operating frequency and very low resultant current (hundreds of pA level for UMB), designing interfaces for EIS is a significant challenge, and developing new topologies for EIS with better accuracy, sensitivity, and higher resolution but smaller-scale IC area has been an active area of research.

2.5. Conclusion

This section introduces the concepts of electrochemical sensor and electrochemical system, and the typical electrochemical measurement techniques, providing the necessary background information for the development of the electrochemical sensor models, and the design of EIS circuits.

Chapter 3

3. Equivalent Small-signal Impedance Models for Electrochemical Ultra-microband Sensor-based Integrated System Design

This chapter reviews and introduces the equivalent small-signal impedance model of UMB electrode sensors by extending the well-known single-electrode Randles model. It also discusses the model's application in AC small-signal stability analysis for two typical potentiostats, with the aim of bridging the knowledge gap between electronic engineers and electrochemical chemists. Part of the work presented in this chapter is based on previously publications: book chapter in *Biomedical Electronics, Noise Shaping ADCs, and Frequency References* (DOI: https://doi.org/10.1007/978-3-031-28912-5_5 *),* and the journal *Sensors, Equivalent Impedance Models for Electrochemical Nanosensor-Based Integrated System Design* (DOI: https://doi.org/10.3390/s21093259)

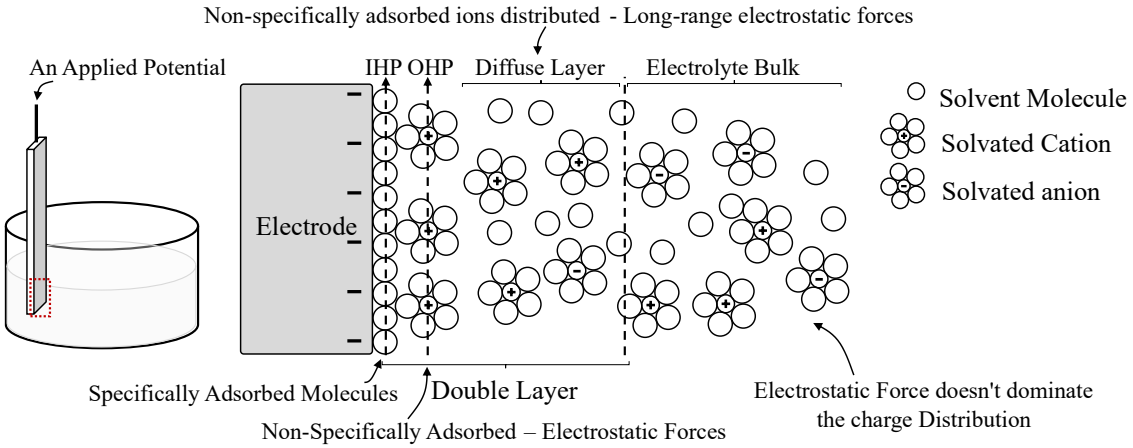


Figure 3.1. The electrode-electrolyte interface for a single electrode.

3.1. Equivalent Small-signal Models for Single Electrode – Randles Model

3.1.1. The Double-layer at the Electrode-electrolyte interface

The electrode-electrolyte interface is the interface between the electrode active surface and the electrolyte, when an electrode is immersed in the electrolyte under the test, as is shown in Figure 3.1. On the left is the electrode, and its surface with the electrolyte is on the right, containing some solvated molecules, solvated cations, and solvated anions [51].

When a potential is applied to the electrode relative to the electrolyte, the solvent molecules and ions are specifically adsorbed onto the surface of the electrode, forming a layer known as the Inner Helmholtz Plane (IHP). The ions with opposite polarity with respect to the potential at the electrode are adsorbed non-specifically due to the electrostatic forces. The locus of the center of the ions defined another layer known as the Outer Helmholtz Plane (OHP). Long-range electrostatic forces cause the cations and

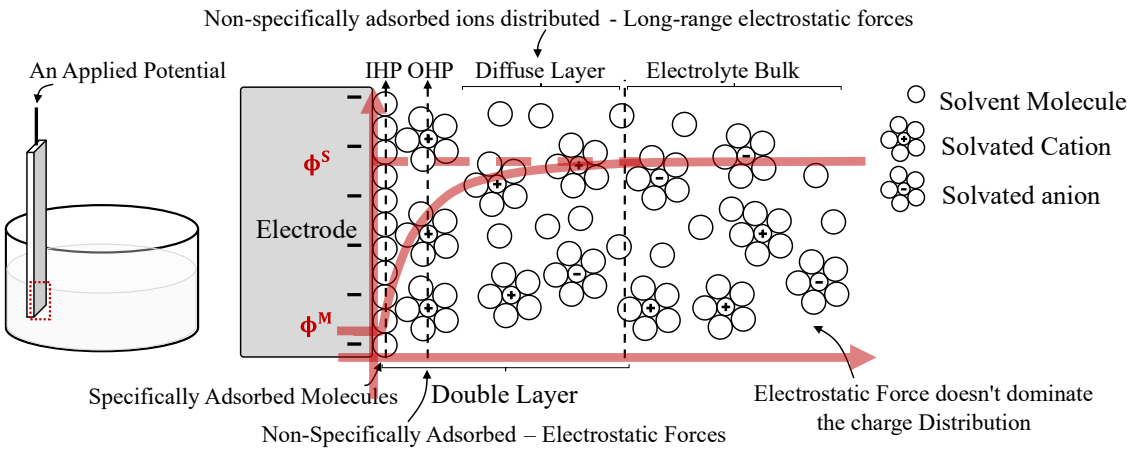


Figure 3.2. The electrode-electrolyte interface and the electrode potential.

anions to be distributed at longer distances from the electrode surface, which is known as the diffuse layer. The electrolyte bulk is the area where the long-range electrostatic force no longer dominates the ion distribution.

The IHP, OHP, and diffuse layer make up the double-layer at the electrode-electrolyte interface [62]. As a result of the charge distribution at the electrode-electrolyte interface, a potential difference arises between the electrode and the electrolyte bulk, which is defined as the electrode potential [51], as shown in Figure 3.2. The electrode potential, E, is described in (3.1):

$$E = \phi^M - \phi^S \tag{3.1}$$

where ϕ^M is the potential at the electrode and ϕ^S is the potential of the electrolyte bulk.

Due to the fact the charge near this double layer can be charged and discharged, showing a capacitor-like behavior, the double layer is physically modelled as a capacitor,

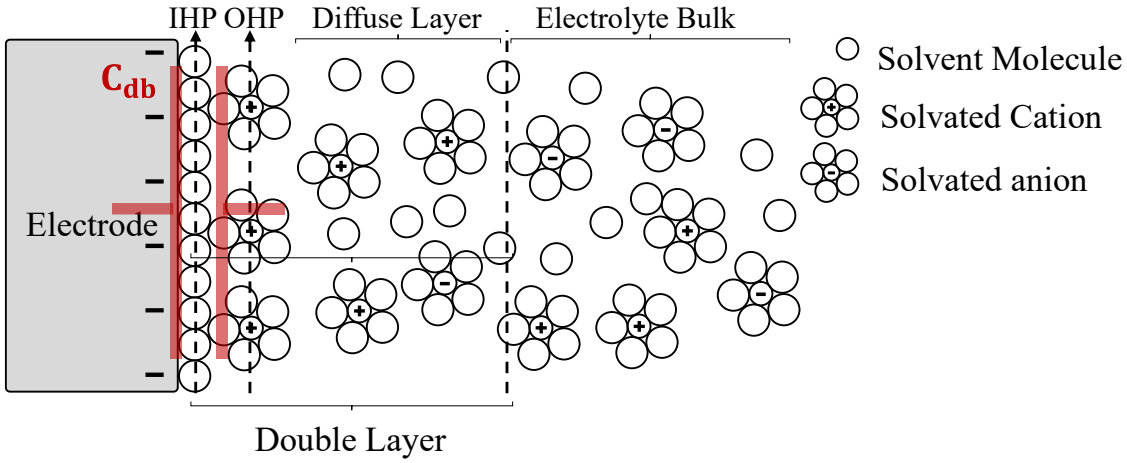


Figure 3.3 The equivalent double-layer capacitor model at the electrode-electrolyte interface.

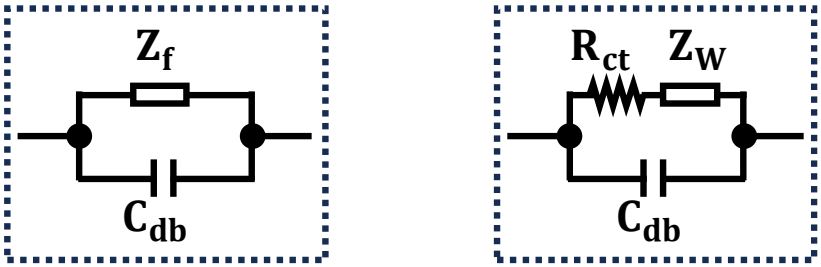
as is shown in Figure 3.3, defined as the double-layer capacitor. Typically, the value of this capacitor is within a range of 10 to 40 $\mu F/cm^2$ [51].

3.1.2. Modelling of the electrode-electrolyte interface

Electrochemical currents have two fundamentally different types: Faradaic currents and non-Faradaic currents.

Faradaic current flows only when electrons cross the electrode-electrolyte interface to drive an oxidation-reduction event, which follows Faraday's law, as is expressed in (3.2) [63, 64]. Its transient behavior depends on electron-transfer kinetics, described by the Butler–Volmer relations expressed in (2.9) and on mass transport of reactants and products [51].

$$Q = mnF. \tag{3.2}$$



a). b).

Figure 3.4. The equivalent model of an electrode-electrolyte interface: (a) an equivalent model with a capacitor and faradaic impedance in parallel; (b) equivalent with faradaic impedance represented by a charge-transfer resistance and the WI.

Non-Faradaic current, by contrast, is the capacitor-like current flow that accompanies rearrangement of ions and solvent dipoles in the electrical double layer or the reversible adsorption of species that do not change oxidation state. If the electrode potential is stepped or swept, the non-faradaic current is proportional to the rate of potential change, as is expressed in (3.3):

$$i_{non,f} = C_{db} \times \frac{dE}{dt} \tag{3.3}$$

Where dE/dt represents the electrode potential rate of change (Scan Rate, SR), and C_{db} is the equivalent capacitance value of the double-layer.

When a certain voltage is developed across the electrode-electrolyte interface, the faradaic current and non-faradaic current occur concurrently, and hence should be represented by separate current paths: the faradaic process current, i_f , and the double-layer capacitor charging current, i_{db}. Therefore, the structure of the equivalent circuit at the electrode-electrolyte interface should include a capacitor and an impedance in parallel, as is shown in Figure 3.4 (a).

The double-layer capacitor, C_{db}, experimentally behaves as a real capacitor and Z_f represents the faradaic impedance, which is related to the rate of charge transfer reactions at and near the electrode-electrolyte interface. The Faradaic impedance can be regarded as a combination of a charge-transfer resistance, R_{ct}, which reflects the resistance caused by the charge transportation across the electrode and the electrolyte, and an impedance Z_w denoted as the Warburg Impedance (WI), as is shown in Figure 3.4.(b), which describes the mass transport of the electroactive species.

Consider a small AC signal is applied to the electrode and consider the mass is diffusing in semi-infinite length diffusion, the faradaic AC impedance can be expressed in (3.4) [65]

$$Z_f = R_{ct} + Z_W = R_{ct} + \frac{\sigma}{\sqrt{\omega}}(1 - j) \tag{3.4}$$

Where σ is the Warburg coefficient ($\Omega \cdot s^{1/2}$) and ω is the angular frequency.

The real and imaginary parts of the WI are equal, so the phase is fixed at 45° for all ω, and σ links directly to the diffusion coefficients (D_o, D_R) and bulk concentrations (C_o^*, C_R^*) of the oxidized and reduced species, as expressed in (3.5):

$$\sigma = \frac{RT}{\sqrt{2}(nF)^2 A} \cdot \left[\frac{1}{\sqrt{D_O}C_O^*} + \frac{1}{\sqrt{D_R}C_R^*}\right] \tag{3.5}$$

The charge-transfer resistance can be linearized using a Talyor 1st series expansion when the potential at an electrode is at equilibrium potential, as expressed in (3.6) [51]

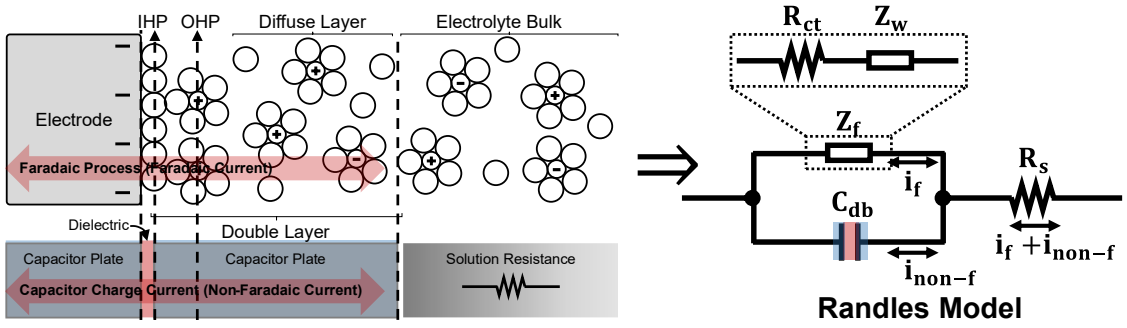


Figure. 3.5. Equivalent Small-signal Models for Single Electrode – Randles Model

$$R_{ct} = \frac{RT}{nFC^*_{O(R)}} \tag{3.6}$$

The model of the electrode-electrolyte interface plays as a unit element for the modeling of a two-electrode electrochemical system and a three-electrode electrochemical system.

3.1.3. The Randles Model

In addition to the electrode-electrolyte impedance, the solution has an associated series resistance, R_s, whose value is decided by the electrolyte in an electrochemical system. Combining all of these elements leads to an AC small-signal model, the Randles Model [57], which is presented in Figure 3.5.

Some studies [66, 67] have shown that the solution resistance, R_s, is related to the ionic concentration, type of ions, temperature, and the geometry of the solution. If the bounded area of the solution is A (m^2), and a uniform amount of current is carried whose length

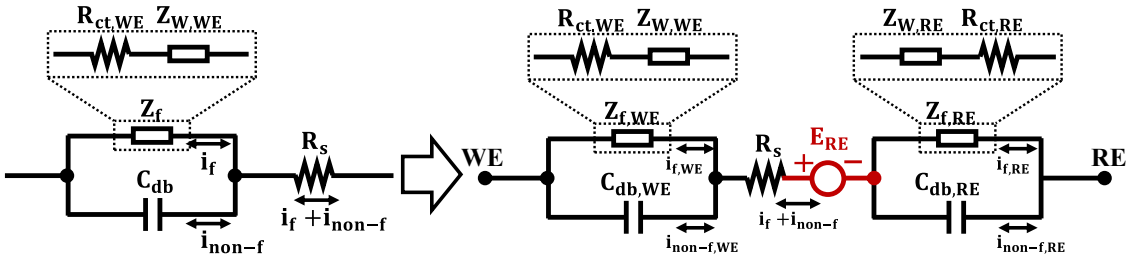


Figure 3.6. The model of the two-electrode sensor system, with a DC voltage source representing the reference electrode potential.

is $l(m)$, where ρ (Ω/m) is the solution resistivity, then the solution resistance can be expressed in (3.7) [51]:

$$R_s = \frac{\rho \cdot l}{A} \tag{3.7}$$

The Randles Model shows that the impedance of a simple redox reaction can be decomposed into an ohmic term, a capacitive term and a frequency-dependent diffusion term, which is the fundamental model in the circuit analysis for electrochemical sensor interface IC design.

3.2. Model of the two-electrode system

The Randles model effectively models the structure of a single electrode-electrolyte interface and its AC impedance, while a two-electrode sensor system has two separate electrode-electrolyte interfaces. As the oxidation reactions and reduction reactions take place at the CE and WE simultaneously, the model of those two electrodes should have the same structure, as is shown in Figure. 3.6. In a two-electrode sensor system, the RE

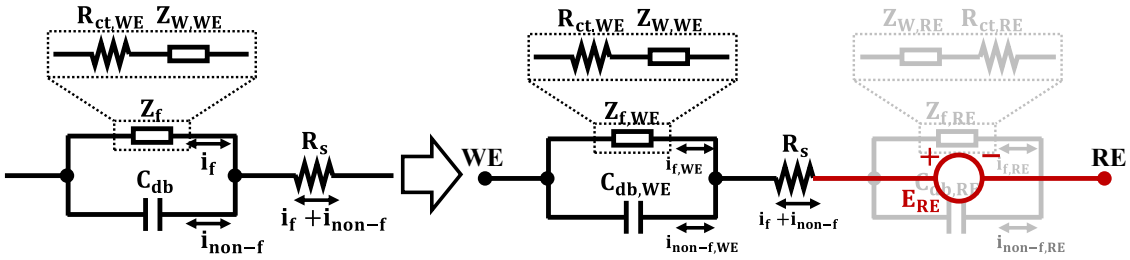


Figure 3.7 The approximated simplified small-signal model for a two-electrode system with tiny current.

should be placed as close as possible to WE, so that the IR drop across R_s is minimized [51].

As aforementioned in Section 3.1.2, due to the fact that the RE introduces an electrode potential, E_{RE}, a DC voltage source is added in series of the impedance model to represent the reference electrode potential, as is shown in Figure 3.6. When a change of potential is applied between RE and WE, if the current flowing through RE is tiny, the electrode potential change at the RE is negligible, which makes the impedance of RE is not significant in an impedance measurement. Finally, the two-electrode system can be approximated to a Randles Model in series with a DC voltage source (can be simplified for AC analysis), as is shown in Figure 3.7, if the sensor current is tiny enough to void an RE electrode potential shift, such as an UMB sensor.

3.3. Model of a three-electrode System

In a three-electrode electrochemical sensor system, as mentioned in Section 2.3.3, the oxidation and reduction reactions occur coherently on the working electrode and counter electrode, while the reaction of interest only occurs at the working electrode. A reference

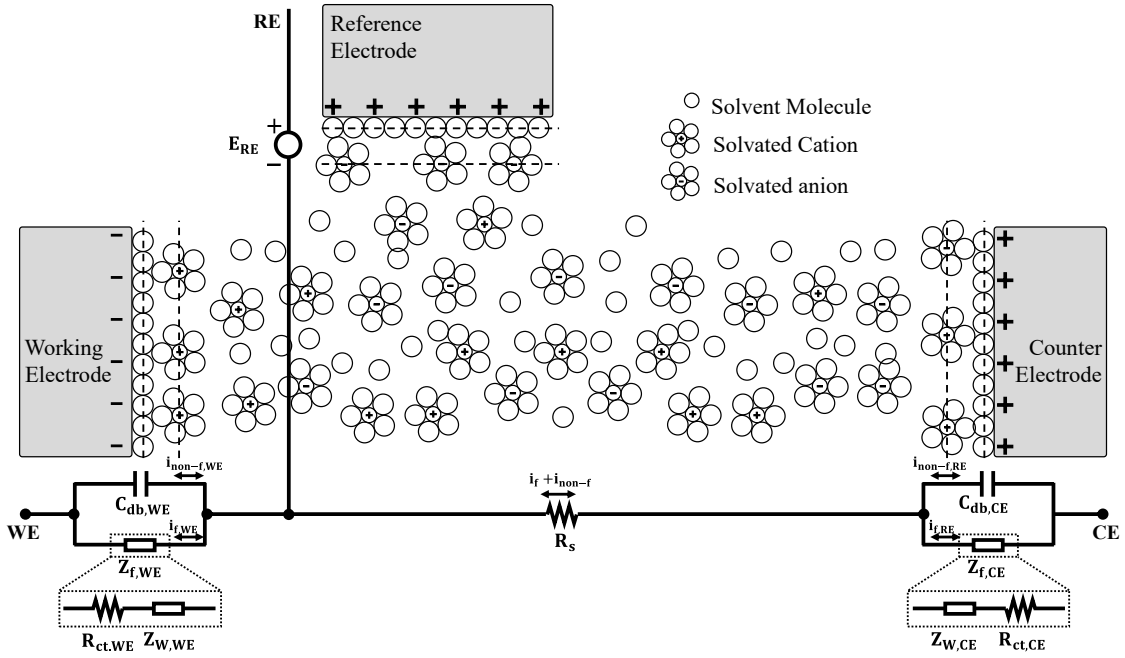


Figure 3.8. The equivalent small-signal model of a three-electrode electrochemical sensor, with the comparison of sensor electrode-electrolyte interface of each electrode.

electrode is added, but only sensing the electrolyte potential with a high DC impedance device, and will not get involved in chemical reactions. Hence, no electrons cross the electrode-electrolyte interface at the reference electrode, and the current to charge the double layer is negligible. Consequently, the structure of a three-electrode reaction cell is shown in Figure 3.8, where the proposed equivalent circuits of the working electrode and counter electrode are structurally symmetric to reflect the symmetry of oxidation and reduction reactions. As there will be no Faradaic current flowing through the electrode-electrolyte interface at RE, the model at the RE can be simplified to a DC voltage source in series representing the electrode potential of the RE, as illustrated in Figure 3.8.

In this model, the Warburg Impedance is included for both the WE and CE as they have complementary chemical reactions at their respective electrode-electrolyte interfaces

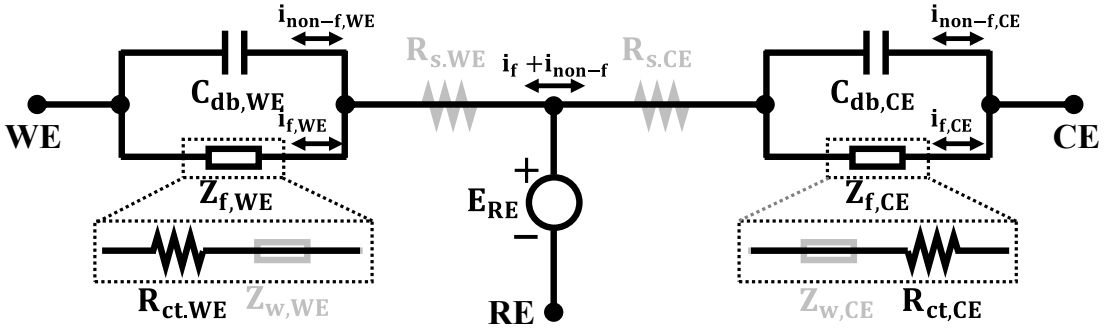


Figure. 3.9 The AC impedance model of UMB three-electrode sensor system for electrochemical sensor interface design.

to maintain the charge within the solution. The WI varies as a function of the applied electrical potential perturbation frequency as expressed in (3.4). At high frequencies, Z_W is small since diffusing reactants don't have to move very far. At low frequencies, the reactants have to diffuse further into the solution, increasing the resultant WI.

For UMB sensor-based electrochemical integrated systems, the sensor current is very tiny, typically ranging from several hundreds of pA to hundreds of nA; therefore, the IR drop caused by the solution resistance can be ignored, and the applied potential difference between the RE and WE, namely, $V_{WE} - V_{RE}$, is approximately equal to the working electrode potential, E_{WE}. In addition, due to the tiny electrode active area, the mass transport near the electrode-electrolyte shows three-dimensional radial diffusion mechanism, where the mass transport has negligible limitation to the sensor current. Consequently, the WI becomes negligible and the small-signal impedance model of an UMB electrode sensor can be reduced to a simple RC circuit as shown in Figure 3.9, where the solution resistance and the WI can be removed from the equivalent model.

The proposed equivalent electrical model in Figure 3.9 provides a model for the three-electrode UMB electrochemical sensor that reflects the reactions at both the WE and CE. Similarly, it demonstrates the significance of the RE electrode, while also providing an electrical model that can be used for AC small signal analysis with an electrochemical UMB sensor-based integrated system [1, 68–74]

With different considerations of the chemical process and electrode types, various types of modified Randles models are proposed in order to meet different research targets [75–77].

3.4. Application of the model in small-signal analysis for typical electrochemical sensor interfaces

The electrochemical sensor interface consists of two design targets, the potentiostat, as shown in Figure. 3.10, and the current digitation circuit, such as an ADC. The potentiostat stabilizes a known potential between RE and WE by sinking or sourcing the current at the CE (with a current control loop), while preventing any current flow into the RE, to avoid electrode potential shift. The other part, the current readout circuit, converts the sensor current into a signal (e.g. voltage, time delay, frequency) which can be digitized and further processed in the digital domain.

This section will discuss the small signal analysis with the three-electrode impedance model, for two typical sensor interfaces. One is an Op-amp and Trans-Impedance Amplifier (TIA)-based potentiostat. In this topology, an ADC is needed to digitize the output voltage (which is out of the scope of this chapter). The other is the current mirror-

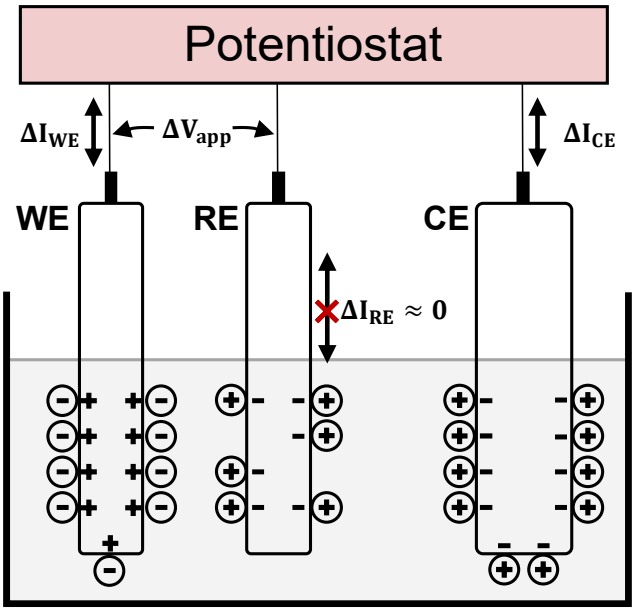


Figure 3.10. The diagram of a three-electrode electrochemical system.

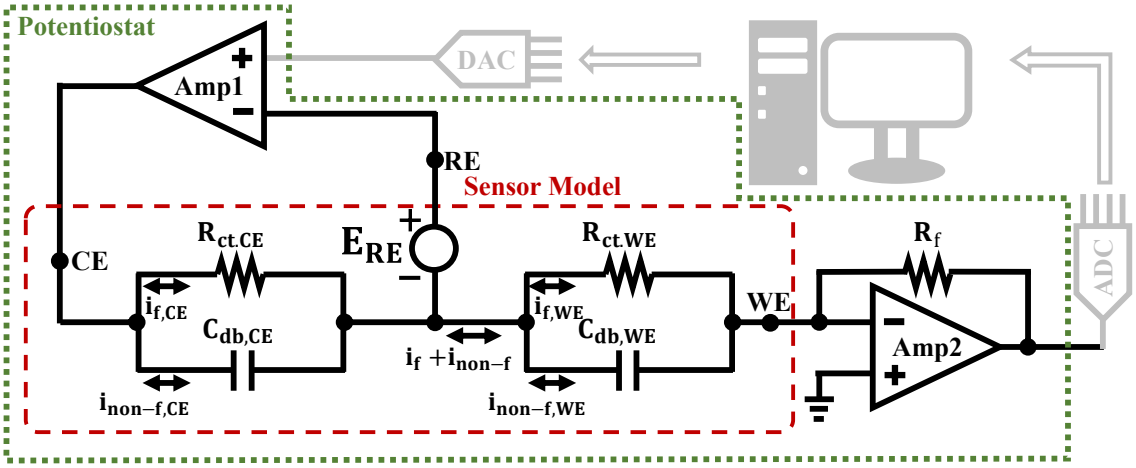


Figure. 3.11. Op-amp and TIA-based potentiostat

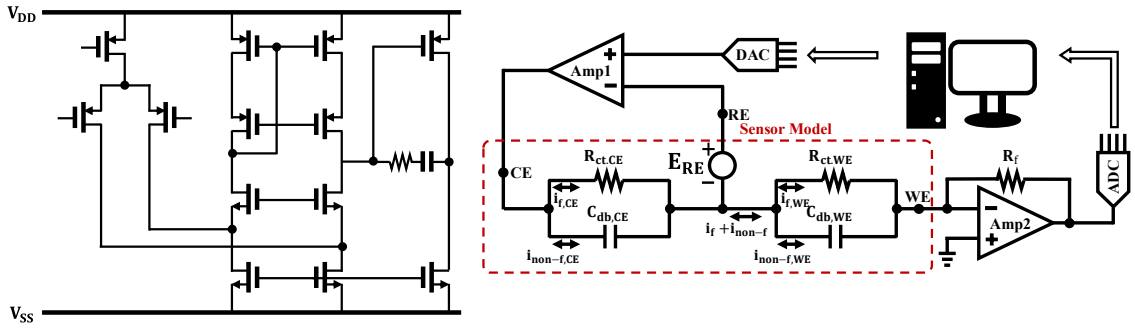


Figure 3.12 A two-stage folded-cascode amplifier [72]

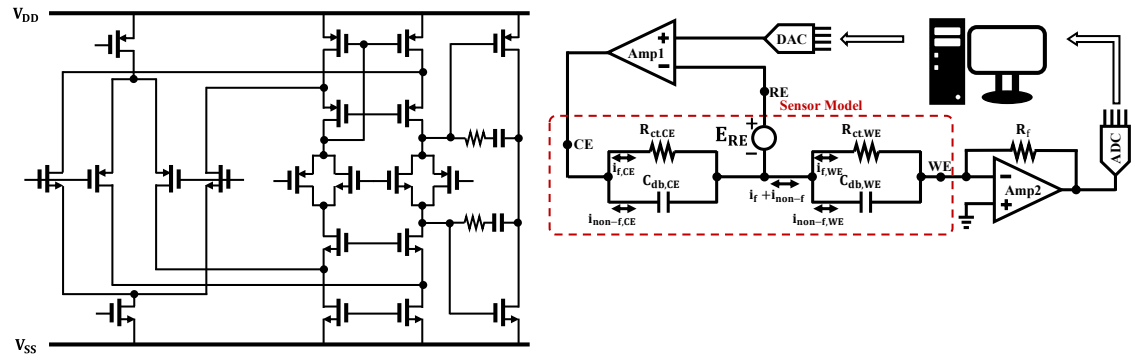


Figure. 3.13. The rail-to-rail folded-cascode with floating class AB controlled output stage [78]

based potentiostat, in which a current-to-frequency converter is applied to digitize the sensor current (which is out of the scope of this chapter).

3.4.1. Op-Amp and TIA-Based Potentiostat

In this topology, a control amplifier is utilized to create a negative feedback loop with the CE impedance in the path, as shown in Figure 3.11. Since Amp1 and Amp2 are capable of dealing with bidirectional current, this type of electrochemical sensor interface can handle both oxidation and reduction chemical reactions. The potential at RE is controlled by a current loop, while nearly no current flows through it, due to the high DC impedance

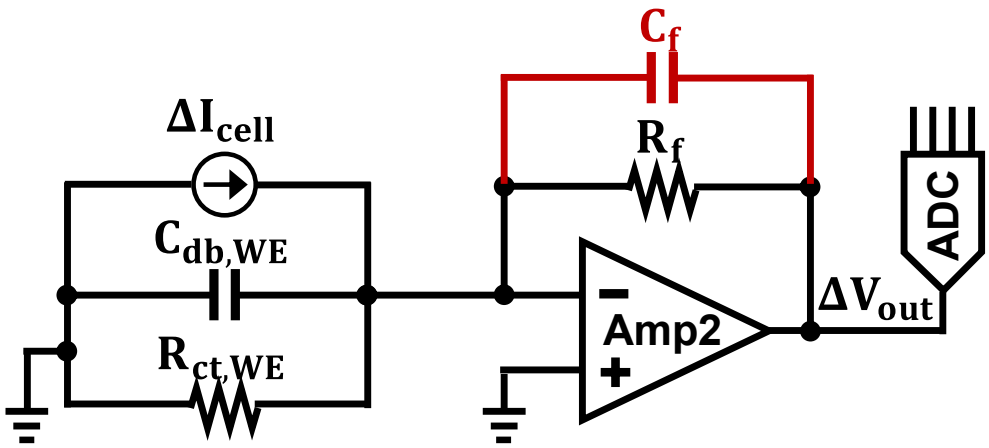
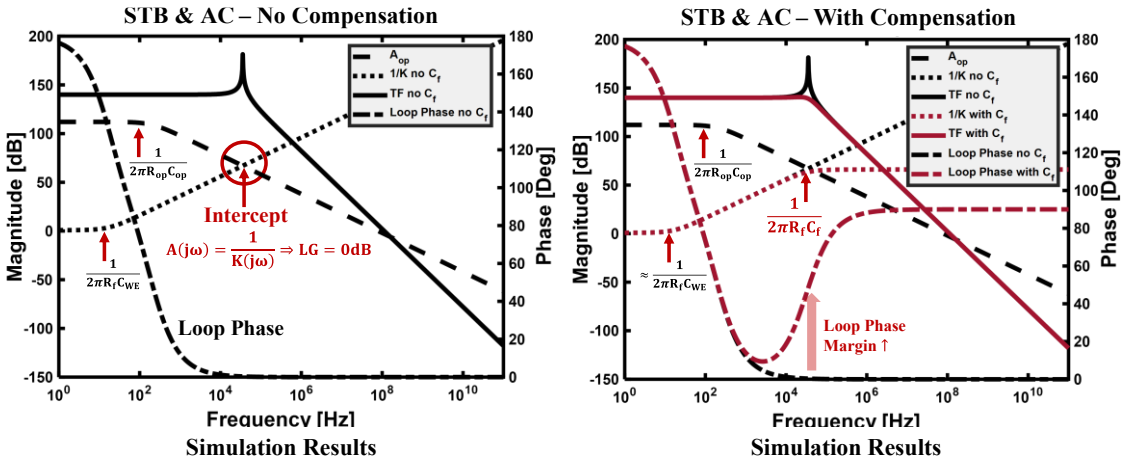


Figure. 3.14. The equivalent model for stability analysis of a TIA

looking into the amplifier input. The application of this circuit is widespread, including voltammetry and EIS.

For UMB electrode sensors, the AC charge-transfer resistor, $R_{ct,WE}$, ranges from approximately 1MΩ to 200MΩ, depending on the selected DC biasing and the sensor current strength [79], and the double-layer capacitor, $C_{db,WE}$, of an UMB electrode sensor can range from hundreds of pFs to tens of nFs [80, 81].

To realize this system using CMOS technology, Amp1 and Amp2 are often implemented as two-stage folded-cascode designs [72], as shown in Figure 3.12, for example, or as a rail-to-rail folded cascode with floating class AB controlled output stage for larger input and output range as the one shown in Figure 3.13 [78]. In order to optimize the specifications such as the Gain Bandwidth (GBW), power dissipation, and noise performance, the devices acting as current sources should be biased in saturation with a strong inversion and devices serving as amplifiers should be designed in saturation with



(a) (b)

Figure 3.15 The stability analysis for TIA

a weak inversion [82]. In addition, the common mode level should consider the potential introduced by the reference electrode.

The charge-transfer resistance and the double-layer capacitor of the electrode-electrolyte interface significantly affects the TIA's stability. Considering the fact that both the Amp1 and Amp2 are designed as a first-order system, their frequency response can be expressed in (3.8). R_{op} and C_{op} are the output resistance and load capacitance of the amplifiers, which introduce a pole at $1/2\pi R_{op}C_{op}$. A_{op} represents the DC gain of the amplifier.

$$A(\omega) = \frac{A_{op}}{(1 + j\omega R_{op}C_{op})} \tag{3.8}$$

The small-signal equivalent model for AC analysis is shown in Figure 3.14. The feedback factor $1/K_{w/o,Cf}(\omega) = 1 + j\omega R_f C_{WE}$ causes a pole at the frequency $1/$

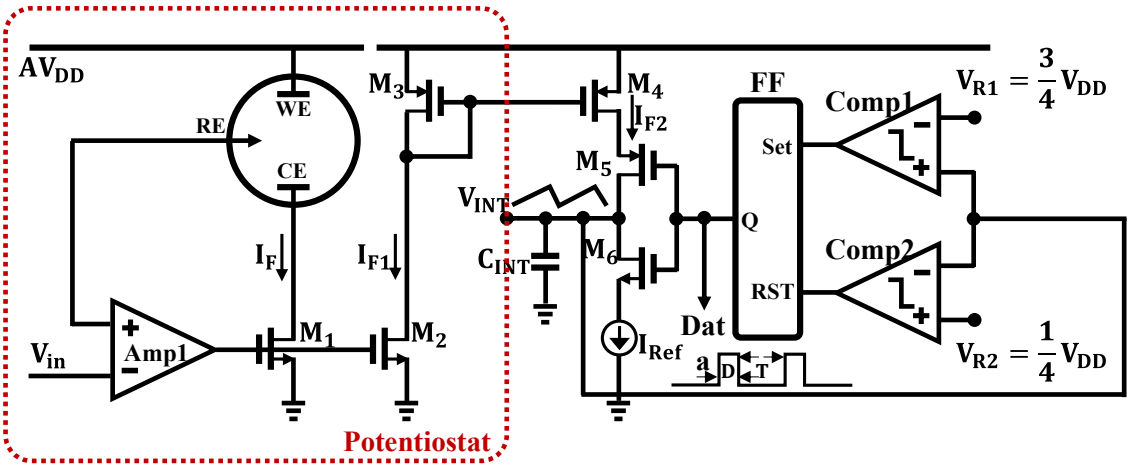


Figure 3.16 The current mirror-based potentiostat and current-to-frequency converter

$2\pi R_f C_{WE}$, and the instability occurs at the intercept frequency of $A(\omega)$ and $1/K_{w/o,Cf}(\omega)$, as shown in Figure 3.15(a). To solve this issue, a feedback capacitor, C_f, is introduced to place a zero at the frequency $1/2\pi R_f C_f$, whose value should be chosen at a lower value than the intercept of $A(\omega)$ and $1/K_{w/o,Cf}(\omega)$. This compensates the TIA that ensures a large phase margin to achieve higher stability, as is shown in Figure 3.15(b). The feedback factor after compensation is expressed in (3.9), with a practical consideration: $C_f \ll C_{WE}$.

$$\frac{1}{K_{w/,C_f}(\omega)} \approx \frac{1 + j\omega R_f C_{WE}}{1 + j\omega R_f C_f} \tag{3.9}$$

The drawback of this topology is that the amplifier needs to be designed with a large bandwidth for the applications requiring a higher bandwidth, such as EIS, and should be able to sink/source a current level ranging from several nA for the UMB sensors.

3.4.2. Current-Mirror-Based Potentiostat

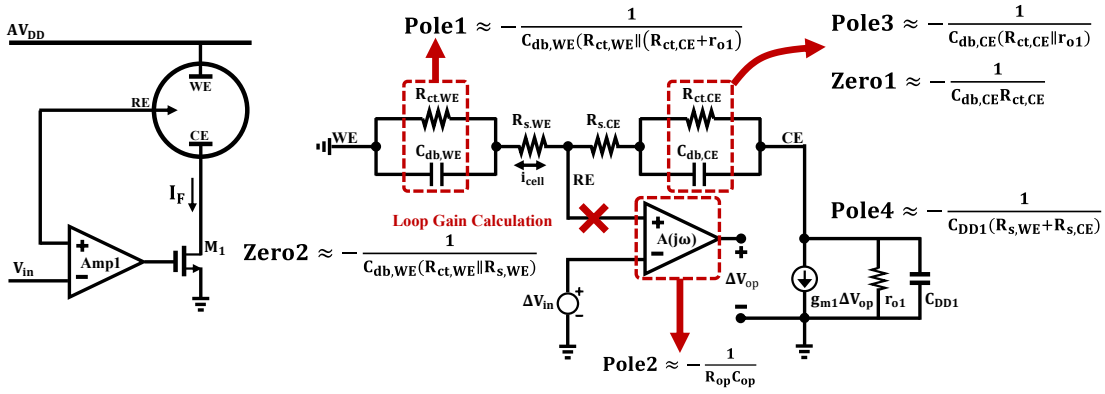


Figure 3.17. The equivalent small-signal model for stability analysis [83].

The current mirror-based potentiostat was first proposed in [83] for three-electrode electrochemical sensor systems, as shown in Figure 3.16, and for two-electrode systems, a current mirror-based potentiosat was proposed in [84]. In this architecture, a by-pass transistor M1 is introduced to pass the electrochemical sensor current and control the potential at the RE to match the applied voltage Vin, by establishing a negative feedback loop with an operational amplifier Amp1. To perform stability analysis, the circuit can be linearized to its small signal equivalent model, as seen in Figure 3.17.

$$LG(s) \approx -\frac{g_{m1}r_{o1}A_{op}(1+sR_{ct,CE}C_{db,CE})(R_{ct,WE}+R_{s,WE}+sR_{ct,WE}R_{s,WE}C_{db,WE})}{(1+sR_{op}C_{op})\{1+sC_{db,WE}[R_{ct,WE}||(R_{ct,CE}+r_{o1})]\}[1+sC_{db,CE}(R_{ct,CE}||r_{o1})][1+sC_{DD1}(R_{s,WE}+R_{s,CE})]} \quad (3.10)$$

The loop gain is calculated by breaking the loop at the non-inverting input. The Loop Gain (LG) is expressed in (3.10), where the amplifier is modeled as a first order low-pass filter with a DC gain A_{op}, as previously expressed in (3.8).

Some practical assumptions are made for the small-signal analysis i) The solution resistance R_s is much smaller than the charge-transfer resistance R_{ct}. ii) The parasitic capacitance C_{DD1} of M1 is much smaller than the double-layer capacitor. iii) For UMB

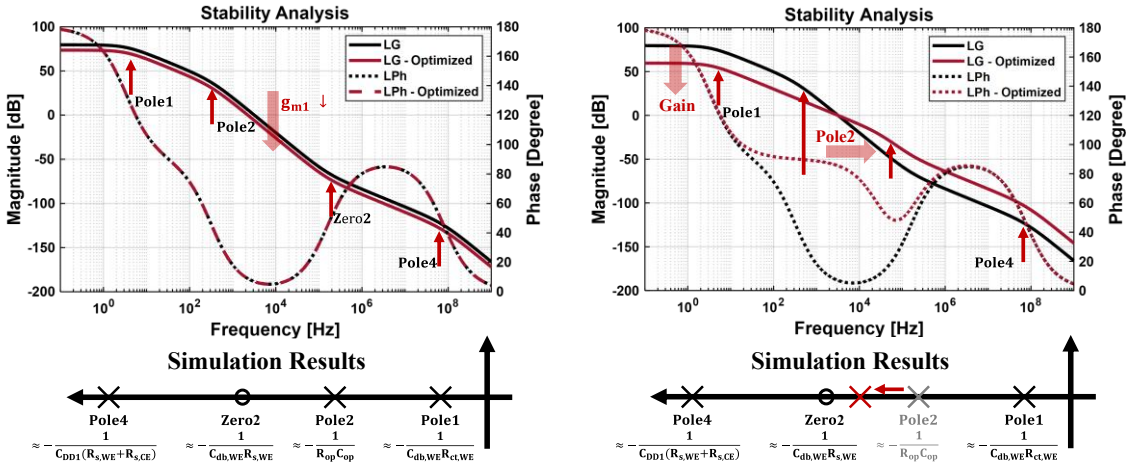


Figure 3.18. The stability analysis for current-mirror based potentiostat.

electrode electrochemical sensor systems, the cell current is very small yielding a large output resistance r_{o1} of M1, namely, $r_{o1} >> R_{ct}$. The system has two zeros and four poles as described from (3.11) to (3.16).

$$Zero1 \approx -\frac{1}{R_{ct,CE}C_{db,CE}} \tag{3.11}$$

$$Zero2 \approx -\frac{1}{(R_{ct,WE}||R_{s,WE})C_{db,WE}} \tag{3.12}$$

$$Pole1 \approx -\frac{1}{C_{db,WE}[R_{ct,WE}||(R_{ct,CE}+r_{o1})]} \tag{3.13}$$

$$Pole2 \approx -\frac{1}{R_{op}C_{op}} \tag{3.14}$$

$$Pole3 \approx -\frac{1}{C_{db,CE}(R_{ct,CE}||r_{o1})} \tag{3.15}$$

$$Pole4 \approx -\frac{1}{C_{DD1}\left(R_{s,WE} + R_{s,CE}\right)} \tag{3.16}$$

It can be seen that $Zero1 \approx Pole3$ when $r_{o1} \gg R_{ct,CE}$ and $Pole4$ is far away from other poles due to the small value of the parasitic capacitor of M1, C_{DD1}. $Pole1$ is dominated by the sensor electrode interface at WE, which will be the dominant pole. The second pole, $Pole2$, is the non-dominant pole caused by the amplifier. To ensure stability, the second pole must be located away from the dominant pole introduced by the sensor, as shown in Figure 3.18. The output resistance and parasitic capacitance of the amplifier must be selected with care, trading off against gain and phase margin, forcing the second pole to a higher frequency. At the same time, the reduction of the size of M1 contributes to ensuring stability by pushing the zero crossing to a lower frequency, but this sacrifices the gain and GBW.

3.5. Conclusion

This chapter introduced a model of the UMB electrode electrochemical sensor from the single-electrode system to two-electrode system, and finally the three-electrode system. The AC small signal stability analysis of two typical potentiostat topologies is discussed, to illustrate the challenges of the model in terms of the sensor interface design. The model is only suitable for small signal applications such as EIS, and a model that reflects the large-signal behavior is still required to develop more accurate sensor interfaces. Further work on the modelling of the UMB sensors will be presented in section IV.

Chapter 4

4. A Fast Electrochemical Impedance Spectroscopy with A Square Wave as Excitation Signal for Impedance-based Biomedical Applications

This chapter proposes a square-wave-based EIS technique for label-free, impedance-based biomedical applications, which shortens EIS measurement time and reduces the complexity of EIS interface circuitry. To start, a dynamic model of the UMB sensor is designed and implemented in Verilog-A. This model supports various types of simulations—including transient simulation, DC operating point simulation, DC sweep simulation, and AC small-signal simulation (e.g., AC sweep, noise, and stability analyses)—thus providing more realistic sensor characteristics for sensor interface design, compared to the conventional AC impedance model discussed in Chapter 3. The content presented in this chapter is based on work published in *IEEE BioCAS 2024* and in the *IEEE Transactions on Biomedical Circuits and Systems*.

4.1. Introduction

Electrochemical sensors are gaining popularity for a variety of biosensing applications, owing to their high sensitivity, high resolution and fast response [5, 8]. Among various electrochemical detection techniques, EIS plays a critical role in label-free impedance-

based biomedical applications [23]. In label-free sensors, such as those used for DNA detection [85], virus detection [80, 86] or antigen detection [13], particles typically bond to a pre-functionalized electrode, making the electrode surface more insulating and thus increasing the impedance at higher substrate analyte concentrations. In contrast, for an enzymatic or redox-active biosensor (e.g. glucose sensor [87]), the presence of enzymes enhances the redox turnover as the concentration rises, which lowers the electrode-electrolyte impedance at higher concentrations. The fundamentals of EIS can be found in tutorials such as [21, 61, 65].

Due to advances in CMOS technology, hand-held EIS measurement devices have become realizable and are widely utilized in biomedical applications, including human disease detection and PoC diagnostics [19, 20]. However, their development and popularity are limited by the long measurement time and circuit complexity of conventional EIS methodologies. The EIS employing In-Phase and Quadrature (I/Q Technique) mixing applies a sinusoidal signal to the sensor, and the resulting sensor signal is mixed with in-phase and quadrature reference signals, as discussed in [27–29, 31]. While I/Q technique-based EIS excels at detecting electrode impedance in noisy environments —owing to high-performance lock-in amplifiers— it requires mixers, quadrature clock generators and a sinusoidal excitation generator such as a Direct Digital Synthesis (DDS) [30], which adds further complexity to the circuit implementation. MPD EIS methodology uses a magnitude detector and a phase detector, each followed by a counter, avoiding the need for quadrature signal generation [88]. Nevertheless, as in I/Q-technique-based systems, the test frequency must be incremented sequentially until the

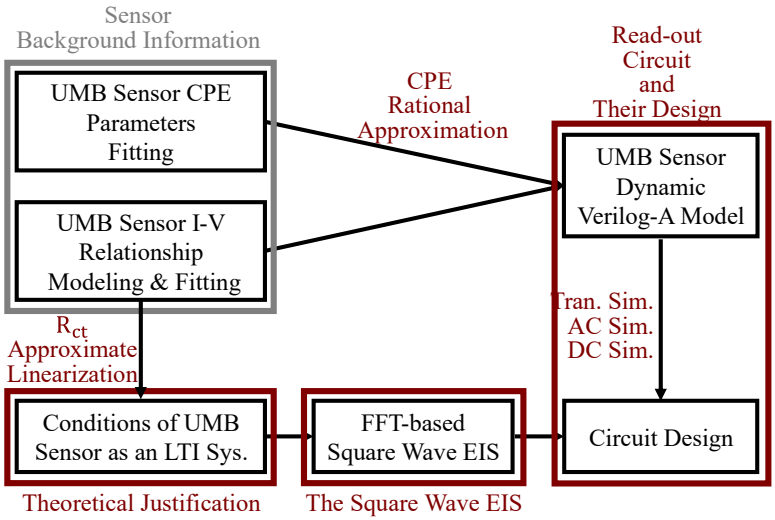


Figure 4.1 The overall diagram that indicates the contribution of this work

maximum desired frequency is reached, which prolongs the completion of a single EIS measurement and poses disadvantages for real-time EIS applications. FFT-based EIS employs white noise-like wide-band signals such as multi-sine signals [33, 37], chirp-signals [32], system noise [35], pseudo random sequences [34, 36] or other wideband signals [89] as stimuli for EIS measurements, and the impedance is computed by applying an FFT to the input and output sensor signals. This method significantly shortens the measurement time from several hours to a few minutes; however, it relies on a high-resolution, wide-band DAC or excitation generator to produce these wide-band signals, thus increasing the circuit complexity. Some bio-impedance techniques discussed in review works [90, 91] inject a square-wave current along with additional analog techniques to mitigate the impact of baseline impedance for a higher dynamic range and SNR [92–94], and to cancel the harmonic error [95] to achieve a higher accuracy or lower power [96, 97], but the proposed methods still need a frequency sweeping, and are not

applicable to a label-free EIS detection with a three-electrode system. Consequently, an EIS methodology with short measurement time, high accuracy, and low complexity is required to enable portable EIS for label-free biomedical applications.

This research introduces and validates an FFT-based time-domain square-wave EIS methodology that offers advantages in both reducing the measurement time and circuitry complexity. An overall diagram, as is shown in Figure. 4.1, virtualizes the contributions of this work. In this work, a square wave is used as the sensor excitation signal, and its harmonics are used for computing the EIS via an FFT. To avoid large distortion and the impedance variance due to decreasing AC amplitudes, the conditions where the UMB sensor is manipulated as a pseudo LTI system are determined by examining the linear region with both theoretical modeling and experimental tests. Based on the modeling of the charge-transfer resistance of the sensor and the rational approximation of the CPE, a dynamic UMB electrode sensor model is implemented in Verilog-A, offering more realistic UMB sensor behavior, which supports multiple simulation analyses for the circuit design. A circuit consisting of a control amplifier-based potentiostat and a TIA is designed and fabricated in a 65 nm CMOS process, to validate the proposed square-wave EIS approach.

The chip measurement results achieve a high accuracy of 2.73% MAPE, on average, for five pre-deposited UMB electrodes tested across four FcCOOH concentrations, compared with those from a commercial electrochemical instrument AutoLab. The measurement time is shortened by 91.7% (from 72 seconds to 6 seconds), in a frequency range of 0.5 Hz to 500 Hz. This fast measurement time and high accuracy successfully

validate the feasibility of the proposed square-wave EIS for portable, real-time label-free biomedical detection devices.

4.2. Models and the Time-Invariant Linear Region of UMB Electrode Sensors

This section begins by introducing the diffusion mechanisms of UMB electrode sensors, which provide properties essential for theoretical analysis. It then presents the charge-transfer rate model of UMB electrode sensors and its small-signal linearization. Finally, the practical linear region and the biasing conditions where square-wave EIS can be applied are experimentally verified.

4.2.1. UMB Sensors and their Diffusion Mechanisms

The UMB electrochemical sensors were fabricated on a silicon wafer substrate with eight individual gold UMB WEs (1 μm × 45 μm × 150 nm), a shared platinum pseudo RE (500 μm × 10 mm × 150 nm) and a shared platinum CE (500 μm × 10 mm × 150 nm), as is shown in Figure 4.2(a). 19-pin Mini HDMI-compatible pin-outs were integrated at the edge of the chip, allowing for external electrical connections.

A typical CV measurement of an UMB electrode sensor is shown in Figure 4.2(b). Unlike other electrodes, which typically exhibit a “duck-shaped” current response, UMB electrode sensors show a “sigmoidal” profile, due to their uniform three-dimensional radial diffusion mechanism near the electrode-electrolyte interface. In this radial diffusion mechanism, the diffusion layer thickness near the UMB electrode is thin, stable and

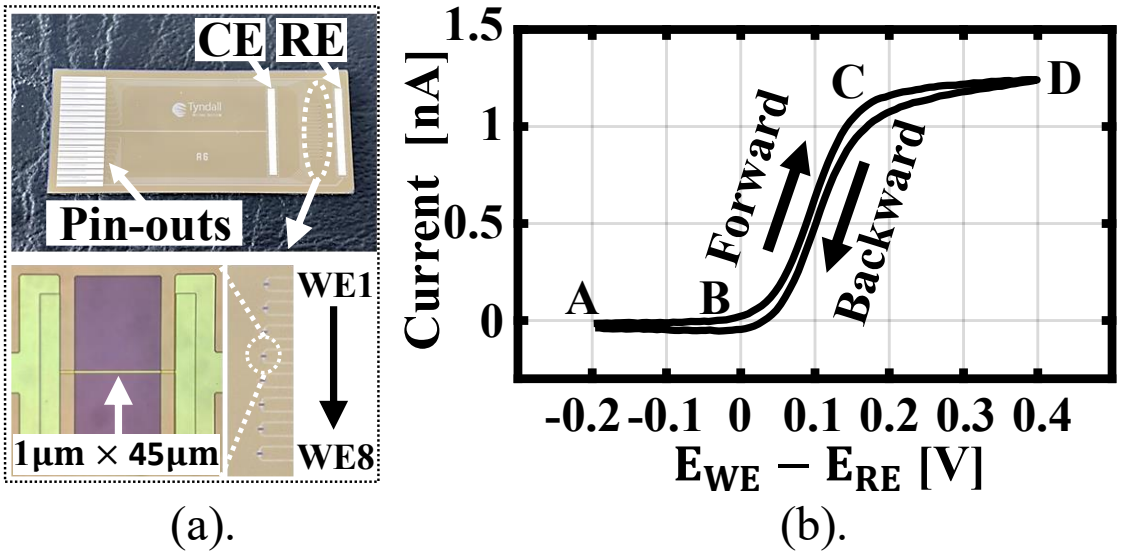


Figure 4.2. (a). A silicon wafer substrate with eight individual UMB electrodes. (b). The measurement results of CV with an UMB electrode sensor in 1 mM FcCOOH dissolved in 10 mM PBS at 25° C, SR = 50 mV/s.

exceeds the electrode physical size, which guarantees the mass can effectively transfer from the bulk to the electrode surface, as demonstrated in [54].

Consequently, the rate of the species replenishment is sufficiently rapid and stable to maintain an adequate analyte concentration at the electrode-electrolyte surface of the UMB electrodes, yielding a steady-state current as indicated from C to D in Figure 4.2(b), where the current level doesn't drop with higher electrode potential after the peak current during a CV measurement, unlike other macro electrodes such as [52, 98].

Due to the unique three-dimensional radial diffusion mechanism, the sensor current of an UMB electrode is no longer limited by the mass diffusion effect [99], which enables straightforward high-speed kinetic studies, and achieves enhanced current density, higher SNR, shorter analysis time and low-volume analysis for on-chip sensor integration [100].

4.2.2. Charge-transfer Rate Model of UMB Electrode Sensors and its Small-signal Linear Approximation

The charge-transfer rate at the electrode-electrolyte interface, at which the electrochemical reaction takes place, can be represented by the reciprocal current relation as described in (4.1) [101]:

$$I_{tot}(E) = \left(\frac{1}{I_{mt}(E)} + \frac{1}{I_{et}(E)}\right)^{-1}, \tag{4.1}$$

where $I_{mt}(E)$ is the mass-transportation-controlled current, $I_{et}(E)$ is the electron-transfer-controlled current, and E is the applied electrode potential.

In a static liquid, reactants are consumed at the electrode surface, producing a concentration difference between the electrode surface and the bulk solution. The established concentration gradient drives reactants toward the electrode surface while causing products to diffuse away into the bulk. In the case of a high-rate charge transfer at the electrode surface, the mass diffusion arising from this concentration gradient becomes the primary mechanism that limits the maximum current. Considering the scenario in which only the Reduced Species (Red) are initially present, and the Oxidized Species (Ox) are absent but produced at the electrode surface via electrochemical reactions, the net mass-transportation-limiting current, I_{mt}, is given by (4.2):

$$I_{mt} = nFAm_R[C_R^* - C_R(x = 0)], \tag{4.2}$$

and (4.3):

$$I_{mt} = nFAm_O C_O(x = 0). \tag{4.3}$$

For $C_R(x = 0) \ll C_R^*$, the maximum possible net oxidation current, also defined as the limiting current, I_l, is given by (4.4):

$$I_l = nFAm_R[C_R^* - C_R(x = 0)] \approx nFAm_R C_R^*, \tag{4.4}$$

where A is the active electrode area, F is the Faraday constant, n is the number of electrons transferred in the reaction, m_R and m_O are the mass-transfer coefficients of Red and Ox respectively, C_R^* and C_O^* are the bulk concentrations of Red and Ox respectively, and $C_R(x = 0)$ and $C_O(x = 0)$ are the Red and Ox concentrations at the electrode surface respectively.

Due to the high-efficiency mass transportation mechanism of UMB electrode sensors, the system can be approximated to a reversible, or a quasi-reversible system [99]. Consequently, by substituting (4.2), (4.3) and (4.4) into the Nernst Equation [51], the mass-transportation-controlled current can be approximated by (4.5), with a practical condition of $m_R \approx m_O$.

$$I_{mt}(E) = \frac{I_l}{1 + \frac{m_R}{m_O} e^{-\frac{nF(E-E_0)}{RT}}} \approx \frac{I_l}{1 + e^{-\frac{nF(E-E_{1/2})}{RT}}} \tag{4.5}$$

where E_0 is the formal potential, which is approximately equal to the half potential, $E_{1/2}$, [102] the applied potential where $I_{mt} = I_l/2$.

The charge-transfer kinetics at the electrode-electrolyte interface can be described with Butler-Volmer equations [51]:

$$I_{et}(E) = nFAk_0\left[e^{\frac{\alpha nF}{RT}(E-E_0)} - e^{\frac{(1-\alpha)nF}{RT}(E-E_0)}\right], \tag{4.6}$$

where k_0 is the standard rate constant of the electrode reaction, and α is the transfer coefficient, $0 < \alpha < 1$.

For voltammetry measurements conducted at slow scan rates ($\leq 50\ mV$ per second), each small applied potential step allows the system to nearly re-equilibrate owing to the high-efficient mass transportation, which ensures that the analyte concentration at the electrode surface closely tracks the bulk concentration. Consequently, the large-signal non-linear kinetic behavior of the UMB electrode sensors can be mathematically modeled via Butler-Volmer relationships and Nernst Equation considering equations (4.1), (4.5) and the oxidation counterpart of (4.6), as is described in (4.7) [103]:

$$I_{tot}(E) = \frac{I_{mt}}{1 + e^{-\frac{nF}{RT}(E-E_0)} + K_0 e^{-\frac{nF}{RT}(1-\alpha)(E-E_0)}}, \tag{4.7}$$

where $K_0 = I_{mt}/nFAC_R^* k_0$ is the dimensionless rate constant, whose smaller value indicates the system is more reversible.

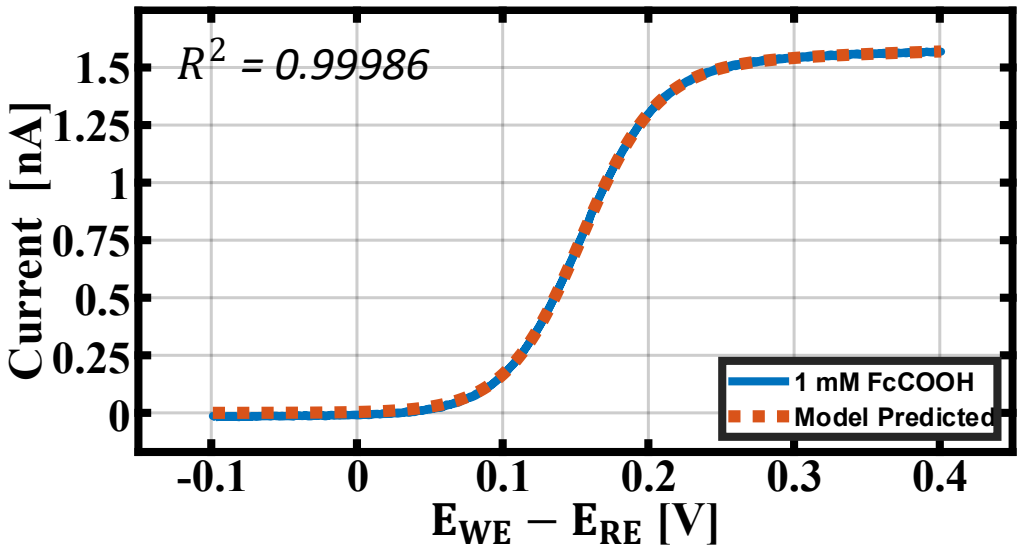


Figure 4.3. The measurement results of CV for one cycle with an UMB electrode sensor in 1 mM FcCOOH dissolved in 10 mM PBS at 25° C, SR = 0.001 V/s, and the Model predicted data.

This charge-transfer rate model of the UMB electrode sensor is validated using CV under the experimental conditions of 1 mM FcCOOH dissolved in 10 mM Phosphate Buffered Saline (PBS) at 25 °C, employing an extremely slow SR of 0.001 V/s to minimize double-layer charging currents. The model is fitted by applying the Levenberg–Marquardt algorithm, using an approximate active electrode area A of 5.85×10^{-11} m^2, and a constrain of α between 0 to 1. The fitted parameters I_{mt}, E_0, α and k_0 are 1.62 nA, 0.155 V, 0.90, and 0.3 cm/s, respectively, and yield an overall correlation coefficient of R^2 = 0.99986, demonstrating excellent agreement between the model and the experimental data, as is shown in Figure. 4.3.

To obtain the large-signal non-linear charge-transfer resistance model, $R'_{ct}(E)$, one first takes the derivative of (4.7) with respect to E, and then forms its reciprocal, as described in (4.8).

$$R'_{ct}(E) = 1/\frac{dI_{tot}(E)}{dE} = \frac{\left\{1 + e^{-\frac{nF(E-E_0)}{RT}} + K_0\left[e^{-\frac{nF(E-E_0)}{RT}}\right]^{1-\alpha}\right\}^2}{I_{mt}\left[\frac{nF}{RT}e^{-\frac{nF(E-E_0)}{RT}} + \frac{nF}{RT}K_0(1-\alpha)\left(e^{-\frac{nF(E-E_0)}{RT}}\right)^{1-\alpha}\right]} \tag{4.8}$$

For a reversible or quasi-reversible system, the standard rate constant $K_0 \ll 1$, and the equation is simplified to (4.9):

$$R'_{ct}(E) \approx \frac{2RT\left[1 + \cosh\frac{nF(E-E_0)}{RT}\right]}{nF \cdot I_{mt}}, \tag{4.9}$$

where the model shows non-linearities.

It can be seen that R'_{ct} reaches minimum around E_0, or $E_{1/2}$, indicating a maximum AC voltage-to-current gain (sensor transconductance) for a higher SNR at the sensor output current for the same small level of applied electrode potential perturbation. In addition, due to the symmetry of the hyperbolic cosine function, the maximum allowable potential swing over which R'_{ct} remains relatively constant is larger than at other selected potentials in the model. Therefore, $E_{1/2}$ has advantages in different aspects to be chosen as the DC bias in small-signal linearization.

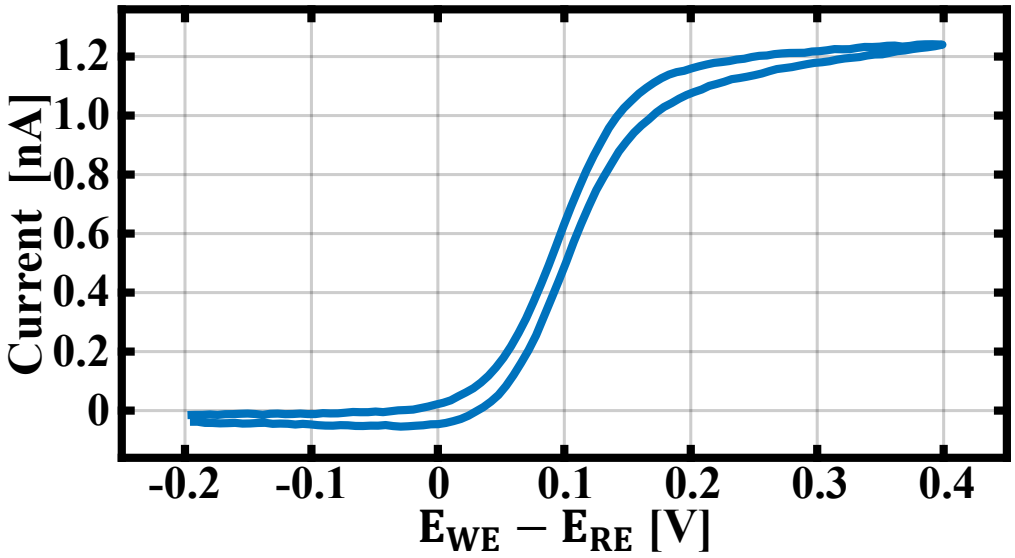


Figure 4.4. The CV measurement result under experimental conditions of 1 mM FcCOOH dissolved in 10 mM PBS at 25° C, with a SR of 50 mV/s.

To linearize the R'_{ct} to its corresponding small-signal linear charge-transfer resistance model, R_{ct}, a First Order Taylor Approximation is applied to (4.8) at $E_{1/2}$, as is shown in (4.10).

$$R_{ct}(E_{1/2}) \approx \frac{\Delta E}{I_{tot}(E_{1/2}+\Delta E/2) - I_{tot}(E_{1/2}-\Delta E/2)} = \frac{RT(2+K_0)^2}{nF \cdot I_{mt}(1+K_0-\alpha K_0)}$$

$$\approx \frac{RT4}{nF \cdot I_{mt}}\Big|_{K_0 \ll 1} \tag{4.10}$$

It can be seen that the R_{ct} around $E_{1/2}$ is linearly approximated as an electrode potential-independent value, enabling the use of a wideband signal containing harmonic frequencies of varying amplitude.

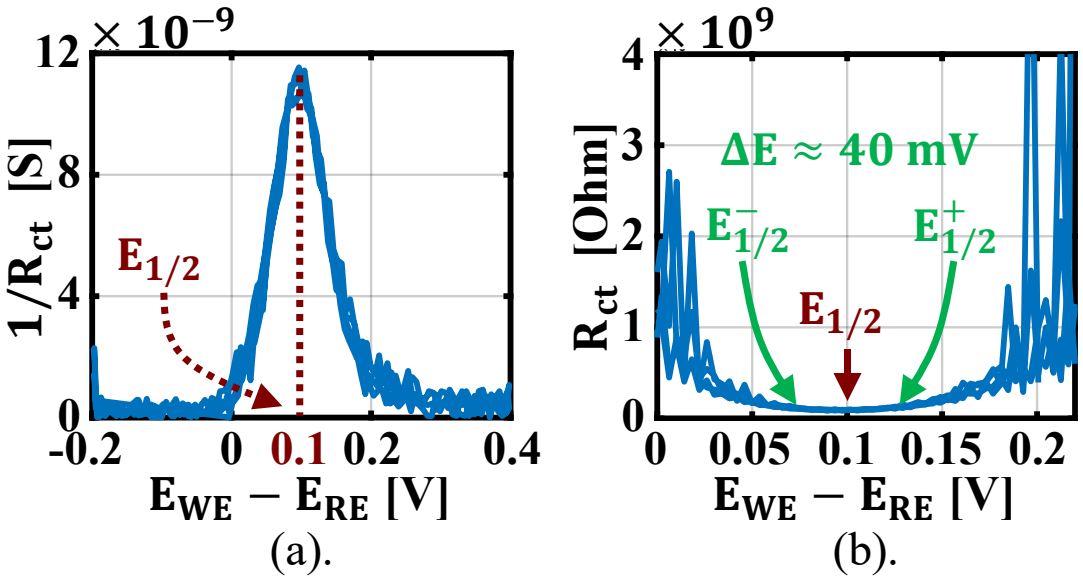


Figure 4.5. The determination of the conditions where R_{ct} is an LTI component. (a). The conductance of the UMB electrode sensor is potential-dependent. (b). Determination of the practical time-invariant linear region.

4.2.3. Practical Time-Invariant Linear Region of UMB Electrode Sensors for EIS

In a practical EIS measurement, the maximum allowable AC magnitude for EIS is constrained by the region in which R_{ct} remains independent of the electrode potential. In a CV measurement result under experimental conditions of 1 mM FcCOOH dissolved in 10 mM PBS at 25 °C, with a SR of 50 mV/s, shown in Figure. 4.4, the DC operating point, $E_{1/2}$, is chosen to be 0.1 V where the transconductance reaches maximum, as is shown in Figure 4.5(a). The maximum allowable AC potential amplitude, $\Delta E \approx E_{1/2}^{+} - E_{1/2}^{-}$, is determined to be 40 mV, where the vicinity of $E_{1/2}$ at which the R_{ct} remains relatively constant, as is shown in Figure 4.5(b).

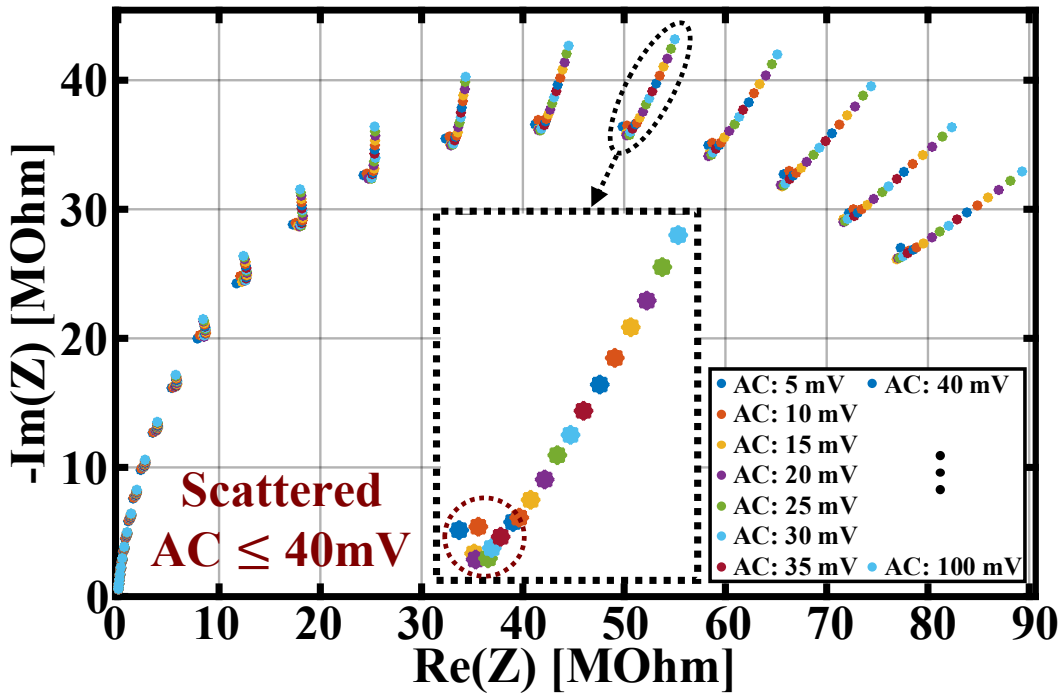


Figure 4.6. EIS results of UMB electrode with AC amplitude increasing from 5 mV to 100 mV, with an incremental step of 5 mV at 0.1 V DC potential.

The linear region is verified through EIS measurements on an AutoLab instrument at a DC potential of 0.1 V, while incrementing the AC amplitude from 5 mV to 100 mV in 5 mV steps. Figure 4.6 presents the resulting EIS data.

It can be observed that for AC amplitudes below 40 mV, the impedance exhibits a scattered distribution; however, as the AC amplitude increases beyond this threshold, a significant increase in impedance is noted, signaling a transition of R_{ct} into the non-linear region. To quantitatively characterize the sensor's impedance variations, the MAPE is computed using the impedance at an AC amplitude of 5 mV as a reference, as shown in Table I. The MAPE increases considerably (over 5% [34, 36, 104]) when the AC

amplitude is beyond 40 mV, indicating the upper limit of the acceptable AC amplitude. In addition, it can be seen that the double-layer near the electrode surface is relatively constant due to the negligible emergence of a phase shift. Consequently, within this identified region, the UMB electrode sensor can be treated as an LTI system, which underpins the use of a square-wave excitation —whose harmonic magnitudes diminish at higher harmonic frequencies— to perform EIS.

Table I. MAPE of the impedance with scanning AC amplitude

AC Amplitude	**MAPE**	**AC Amplitude**	**MAPE**
10 mV	**1.29 %**	60 mV	6.70 %
15 mV	**2.45 %**	65 mV	7.31 %
20 mV	**2.69 %**	70 mV	7.73 %
25 mV	**3.28 %**	75 mV	8.26 %
30 mV	**3.58 %**	80 mV	8.85 %
35 mV	**3.99 %**	85 mV	9.50 %
40 mV	**4.57 %**	90 mV	10.21 %
45 mV	5.14 %	95 mV	10.86 %
50 mV	5.65 %	100 mV	11.40 %
55 mV	6.12 %		

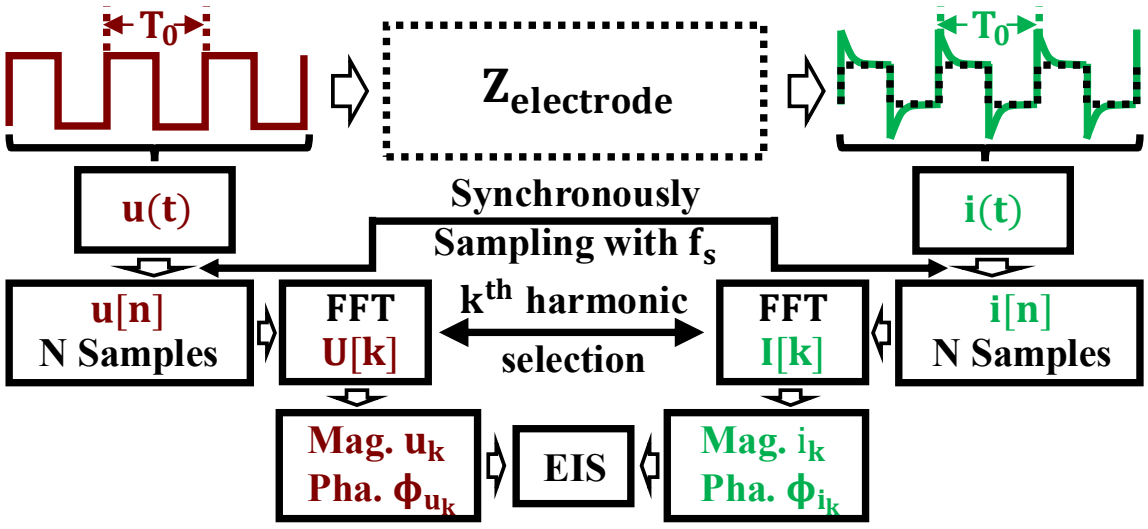


Figure 4.7. The system level diagram of the proposed square-wave EIS.

4.3. The Proposed Square Wave EIS and its Circuit Implementation

4.3.1. Proposed Square-wave EIS via an FFT

The proposed EIS employs a square-wave excitation, and the impedance at the electrode-electrolyte interface is calculated by dividing the complex value of the selected harmonic tones obtained after applying an FFT to both the input and output signals. Figure 4.7 shows the block diagram of the proposed approach, and Figure 4.8 shows the circuit blocks, where a control amplifier acts as the potentiostat and a resistive TIA converts the sensor current into voltage, which will then be sampled by a data acquisition circuitry like an ADC.

The DC operating point where the sensor is linearized is determined to be the potential where R_{ct} reaches minimum, and the maximum AC potential amplitude is determined by

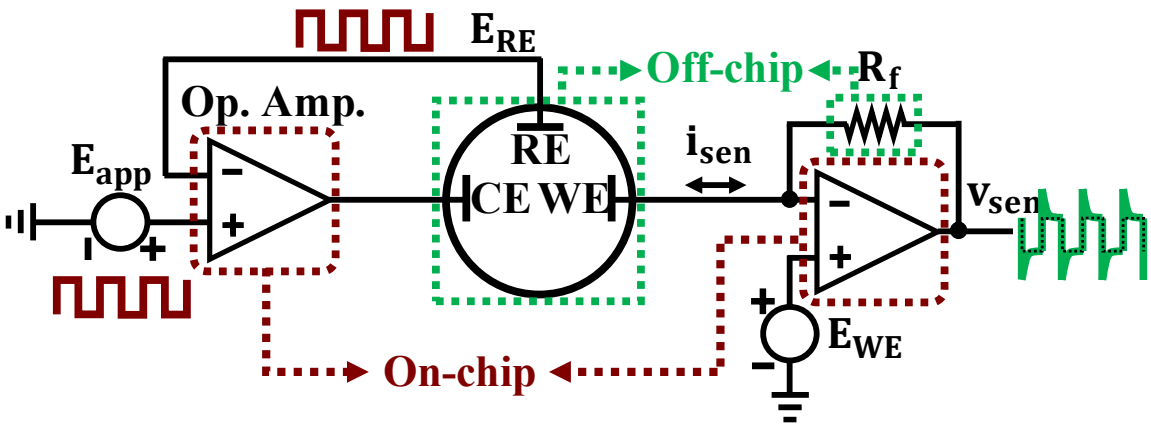


Figure 4.8. The block diagram of the circuit for the proposed square-wave EIS.

identifying the vicinity of the DC operating point at which R_{ct} remains relatively constant, as discussed in Section 4.2.3.

The input and output are synchronously sampled with a sampling rate of f_s for N samples, and the FFT, expressed in complex format in (4.11) through Euler's equation, is employed to compute the EIS:

$$X[k] = \sum_{n=0}^{N-1} s[n] \cos\left(2\pi \frac{kn}{N}\right) - j \sum_{n=0}^{N-1} s[n] \sin\left(2\pi \frac{kn}{N}\right) \qquad (4.11)$$

where $U[k]$ and $I[k]$ represent the k^{th} point in the FFT of the sampled input signal, $u[n]$, and the sampled response signal, $i[n]$, respectively. Since the FFT of a square wave has components only at odd harmonics of the fundamental frequency, f_0 , namely, $(2m-1)2\pi f_0$, where m is an integer number, the tones selected for computing the EIS are given by:

$$k = \frac{(2m-1)\cdot f_0}{f_s}\cdot N, \tag{4.12}$$

and the EIS of the electrode-electrolyte interface at each harmonic frequency of the square wave is determined by (13). The frequency range of square wave EIS is from f_0 to $f_s/2$:

$$Z_{(2m-1)^{th}} = \frac{U[k]}{I[k]} \tag{4.13}$$

Due to the fact that a square wave can be easily generated by a simple single-bit DAC, such as switches, the complexity of EIS circuitry can be considerably reduced, and the measurement time is significantly shortened, due to the quick computation of applying an FFT.

4.3.2. Verilog-A Model of UMB Sensor for Circuit Design

As described in Section 4.2.2, the charge-transfer resistance of an UMB sensor can be expressed in (4.10); therefore, providing a possibility to implement the sensor with Verilog-A in a simulator for a more accurate circuit design.

Unlike the conventional sensor models in Figure 4.9(a) and (b) [57], the model employed in this work comprises a dynamic charge-transfer resistance and a CPE, as shown in Figure 4.9(c).

This approach accommodates real world sensors and their associated variability, yielding greater robustness in the circuit design. The Warburg Impedance, Z_W, is omitted owing to the highly efficient mass transportation [26].

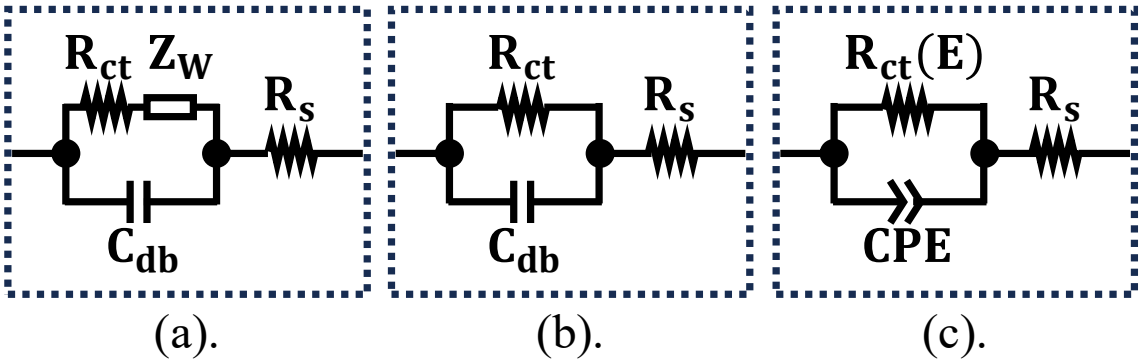


Figure 4.9. Models of electrochemical sensor electrode-electrolyte interfaces: (a). Randle's Model. (b). Randle's Model with Warburg Impedance omitted. (c). Model with CPE, where R_{ct} is dynamic.

CPE is a phenomenological mathematical equation, modeled by (4.14) [105], where Q and γ are the CPE parameters, and $s = j\omega$. It reflects an overall macroscopic response of the electrode surface's non-uniformity, roughness, and even porosity. It cannot be described by a finite number of discrete resistors or capacitors with frequency-independent values, due to the fact that each local sub-microscopic region effectively introduces its own RC combination.

$$CPE = \frac{1}{Q \cdot s^{\gamma}} \tag{4.14}$$

Since the fractional order factor, s^{γ}, cannot be directly simulated by Computer-Aided Design (CAD) tools such as Cadence, and its physical mechanism is still not clear [105, 106], the CPE must be approximated to a rational polynomial expression.

RC combinations have been proposed in [107–109] to model the CPE, but their inaccuracy limits their usability in most applications and circuit analysis. Another study [110] achieved a precise fitting of the CPE using Adaptive Antoulas–Anderson (AAA)

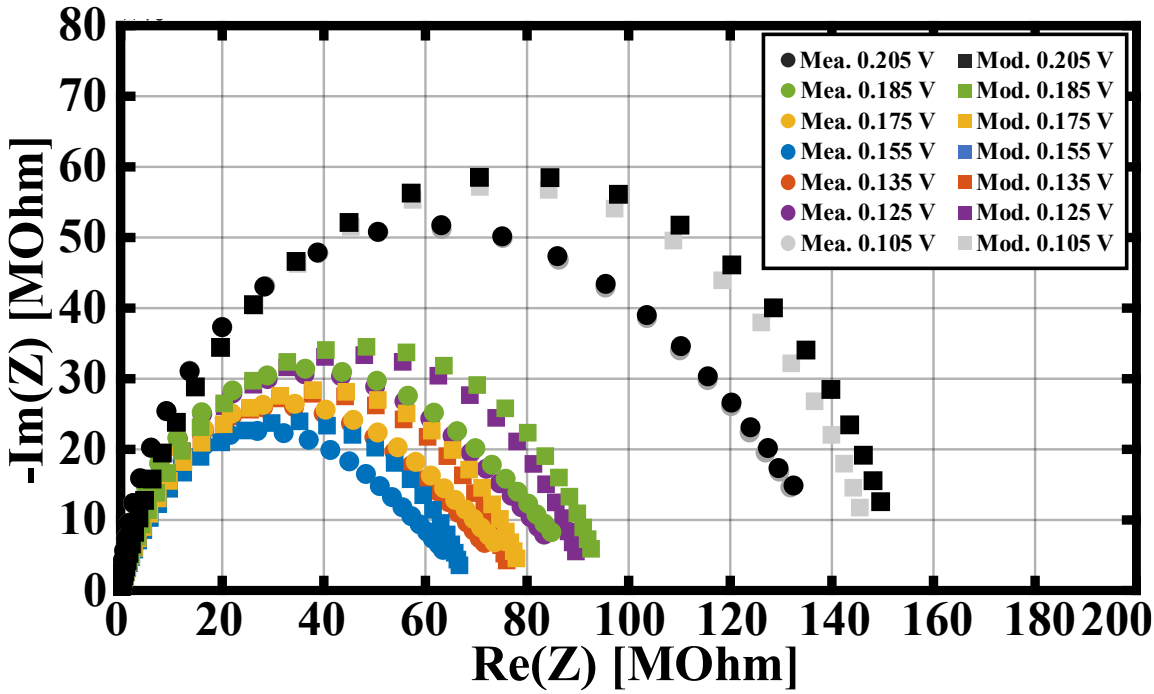


Figure 4.10. EIS measurement results with an amplitude of 10 mV over a frequency range of 0.1 Hz to 100 kHz, vs. Verilog-A model-predicted results from Cadence, on the DC biases of 0.105 V, 0.125 V, 0.135 V, 0.155 V, 0.175 V, 0.185 V and 0.205 V over the same frequency range.

algorithm with an approximate rational function over a broader frequency range; but a potential of none-convergence may exist like other fitting algorithms [111, 112] for a higher order of a rational function. To obtain an accurate approximation of the CPE in a sufficient bandwidth of 0.1 Hz to 1 GHz for the square-wave EIS circuitry design, for simplicity, Modified Oustaloup Recursive Approximation (MORA) is utilized, as expressed in (4.15) [113]. MORA is a numerical computation that avoids the potential non-convergence like a fitting algorithm, while still delivering a suitably accurate approximation.

$$s^{\gamma} \approx \left(9 \cdot \frac{\omega_h}{10}\right)^{\gamma} \left(\frac{9s^2 + 10\omega_h s}{9(1-\gamma)s^2 + 10\omega_h s + 9\gamma}\right) \prod_{k=1}^{N} \frac{s + \omega_k'}{s + \omega_k} \tag{4.15}$$

where $\gamma \in (0,1)$ to ensure the filter is stable, ω_h and ω_b are the upper bound and lower bound of the target angular frequency range respectively, and ω_k' and ω_k are the poles and zeros of the transfer function respectively:

$$\omega_k' = \omega_b \omega_u^{(2k-1-\gamma)/N}, \tag{4.16}$$

$$\omega_k = \omega_b \omega_u^{(2k-1+\gamma)/N}, \tag{4.17}$$

where $\omega_u = \sqrt{\omega_h/\omega_b}$, and the approximated CPE is expressed by (4.18):

$$CPE \approx Q^{-1}(s^{\gamma})^{-1} \approx Q^{-1} \left(\frac{9\omega_h}{10}\right)^{-\gamma} \left(\frac{9(1-\gamma)s^2 + 10\omega_h s + 9\gamma}{9s^2 + 10\omega_h s}\right) \prod_{k=1}^{N} \frac{s + \omega_k}{s + \omega_k'}. \tag{4.18}$$

Together with an implementation of equation (4.7) via a non-linear voltage-dependent current source, and a Laplace Impedance Filter for the approximated CPE, the model shown in Figure 4.9(c) thus can be realized in Verilog-A for running simulations that reflect practical sensor behavior. A validation of the proposed Verilog-A model is shown in Figure 4.10, whose DC operating points for running EIS are chosen to be 0.105 V, 0.125 V, 0.135 V, 0.155 V, 0.175 V, 0.185 V and 0.205 V from Figure 4.3, and the CPE parameters are obtained through optimized fittings with a commercial AutoLab instrument based on sensor-measured EIS data. The Absolute Percentage Errors (APE) between the measured charge-transfer resistance, $R_{ct,mea}$, and the simulated charge-

transfer resistance from the Verilog-A model, $R_{ct,mod}$, at 0.1 Hz, evaluated under various DC biases, are summarized in Table II.

[113]Table II. The absolute percentage error

DC (V)	$\boldsymbol{R_{ct,mea}}$ **(MΩ)**	$\boldsymbol{R_{ct,mod}}$ **(MΩ)**	APE %
0.105	**131.83**	**145.7**	**10.21**
0.125	**83.36**	**89.72**	**7.34**
0.135	**71.62**	**76.07**	**5.91**
0.155	**63.44**	**66.77**	**4.96**
0.175	**73.61**	**77.99**	**5.67**
0.185	**84.79**	**92.71**	**9.05**
0.205	**132.45**	**149.80**	**12.79**

It can be observed that the proposed dynamic Verilog-A model of the UMB electrode sensor exhibits stronger agreement with the measured sensor data in the linear region (1.55 mV $\pm$ 20 mV). In addition, compared to a model with a capacitor, the CPE more accurately reflects the double-layer behavior near the electrode-electrolyte interface [105, 110], which improves the accuracy of the circuit design.

4.3.3. Design of the Amplifier

The potentiostat and the TIA employ the same amplifier topology. To minimize the impact of flicker noise within the target bandwidth ranging from sub-Hz to 1 kHz, the amplifier is designed with a PMOS-input folded-cascode topology, complemented by a Common Source (CS) output stage to enlarge the DC gain and output swing, as is shown in Figure 4.11.

The transistors designated for amplification (M_1, M_2, M_7) and for cascode stage ($M_3 \sim M_6$) are biased in the moderate-inversion region for a larger g_m/I_d to ensure noise,

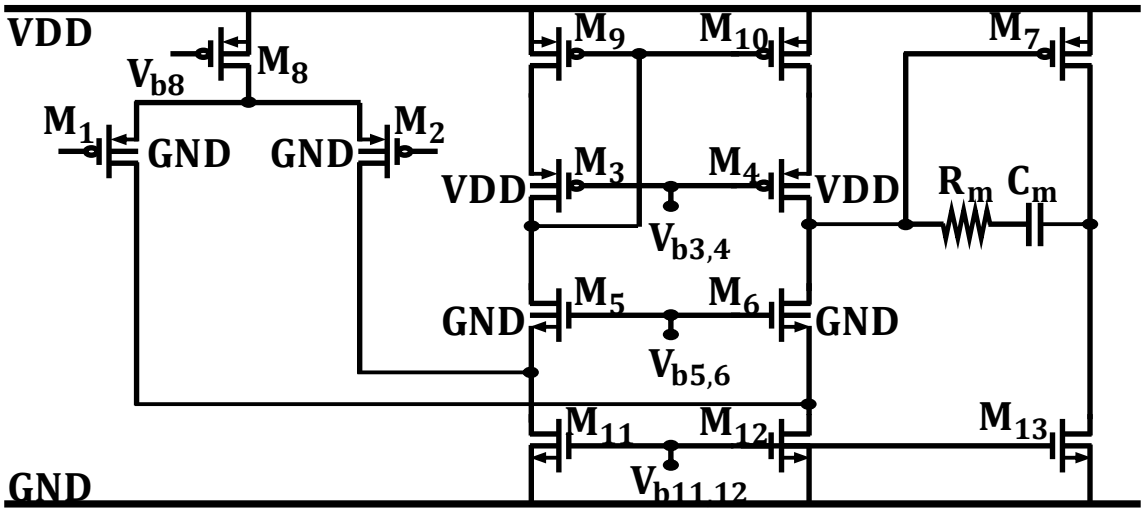


Figure 4.11. PMOS-input folded-cascode amplifier topology, complemented by a CS output stage with Miller compensation.

power and speed optimization, while the transistors ($M_8 \sim M_{13}$) serving as current sources are set to be in strong-inversion region for minimizing the current noise, with long transistor channel lengths to reduce the effects of random mismatches. Table III summarizes the regions of operation for the MOSFET devices within the amplifier. The GBW, attenuated due to the large aspect ratio of those transistors in moderate inversion, can be compensated with a larger g_m of input pairs of both two stages through a high DC biasing current. The Miller compensation is utilized to do the pole splitting and right-hand-side zero cancellation, ensuring its stability. Comprehensively, the amplifier achieves a GBW of 73.7 MHz with 77° of phase margin with a capacitive load of 2 pF, and a DC gain of 113 dB, as is shown in Figure 4.12(a). The dominant noise sources are the flicker noise contributions from the differential input pair and current sources, resulting in a total in-band input-referred voltage noise power of $4.12 \times 10^{-11}\ \mathrm{V}^2$,

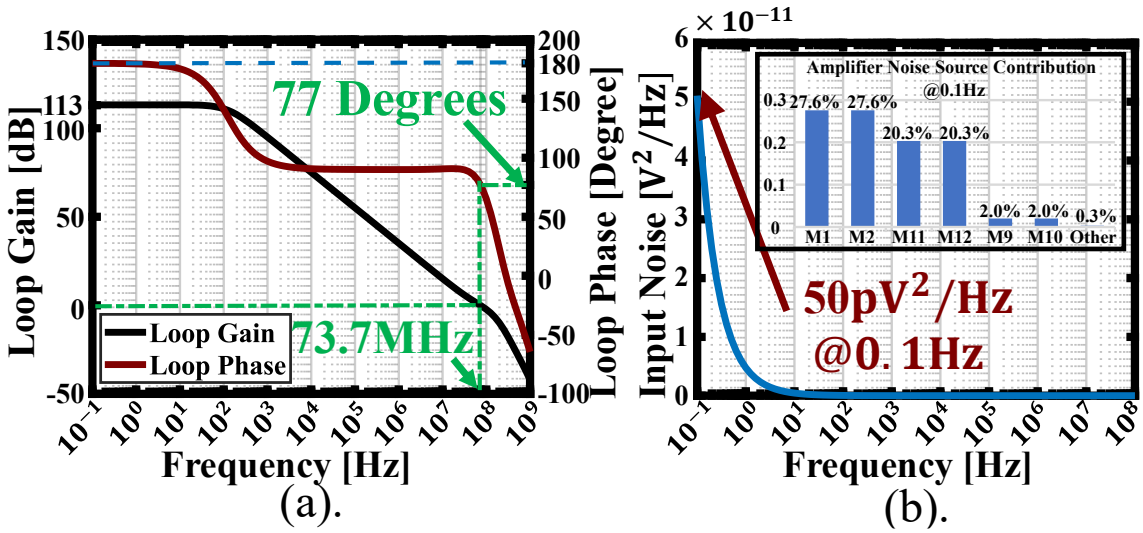


Figure 4.12. (a). Stability analysis, and (b). input-referred voltage noise density spectrum and the noise source contribution of the in-band integrated noise.

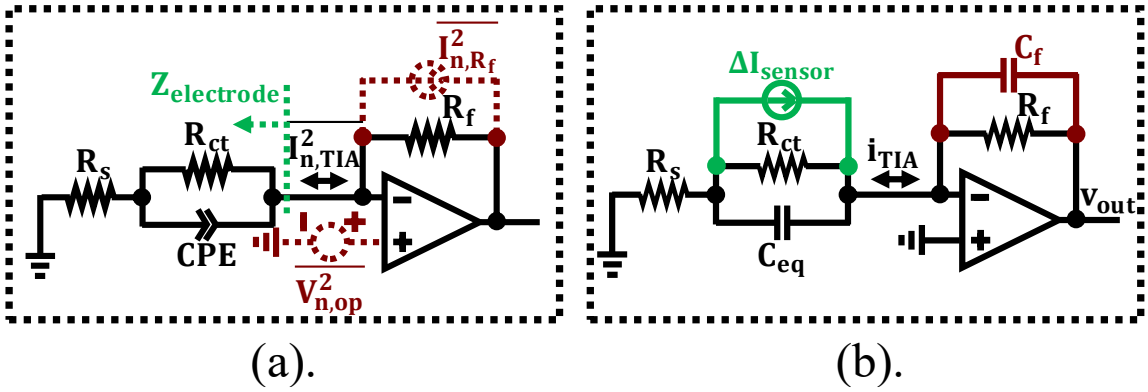
where the input-referred voltage noise density spectrum and the noise source contribution of the in-band integrated noise are shown in Figure 4.12(b). The total power is 1.25 mW.

Table III. The operation regions of transistors

Transistors	Region	g_m/I_d
M_1, M_2, M_7	Moderate inversion region	16
$M_3 \sim M_6$	Moderate inversion region	18
$M_8 \sim M_{13}$	Strong inversion region	10

4.3.4. Design of TIA

The design of the TIA entails the decision of the feedback capacitor, C_f, and feedback resistor, R_f, with an emphasis on noise, bandwidth and stability considerations.



(a). (b).

Figure 4.13. The equivalent models for TIA design. (a). The simplified equivalent model with noise source contributions, and (b). the equivalent model for analyzing stability and bandwidth.

The minimum value of R_f is determined by the noise requirements, and the corresponding simplified equivalent model for noise analysis of a TIA-based electrochemical system is shown in Figure 4.13(a). Taking into account noise contributions from the amplifier and the feedback resistor, the input-referred current noise power density of the TIA, $\overline{I^2_{n,TIA}}$, is expressed by (4.19):

$$\overline{I^2_{n,TIA}} = \overline{V^2_{n,op}} \cdot \left|1 + \frac{R_f}{Z_{electrode}}\right|^2 \cdot \frac{1}{R_f^2} + \frac{4KT}{R_f}$$

$$= \overline{V^2_{n,op}} \left[\frac{1}{R_{ct}^2} + \frac{1}{R_f^2} + \frac{2}{R_{ct}R_f} + Q^2\omega^{2\gamma} + \omega^{\gamma} 2Q \cos\frac{\alpha\pi}{2}\left(\frac{1}{R_{ct}} + \frac{1}{R_f}\right)\right]$$

$$+ \frac{4KT}{R_f}, \qquad (4.19)$$

where $\overline{V^2_{n,op}}$ represents the input-referred voltage noise power density of the amplifier, K is the Boltzmann constant, T is the temperature in Kelvin, and $Z_{electrode}$ represents the

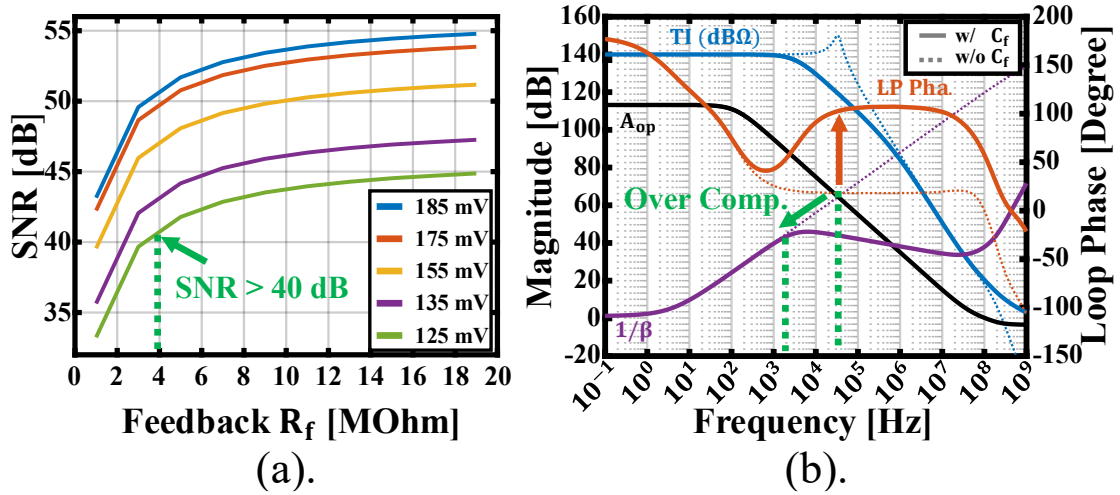
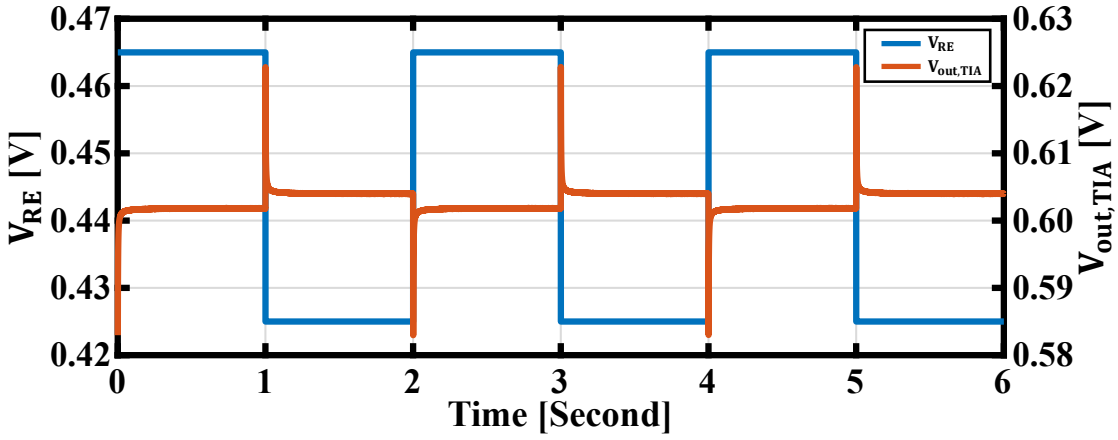


Figure 4.14. (a). The SNR analysis of TIA at a DC bias of 0.125 V, 0.135 V, 0.155 V, 0.175 V and 0.185 V. (b). The stability analysis of TIA with overcompensation. Note that the transimpedance has a unit of Ohm.

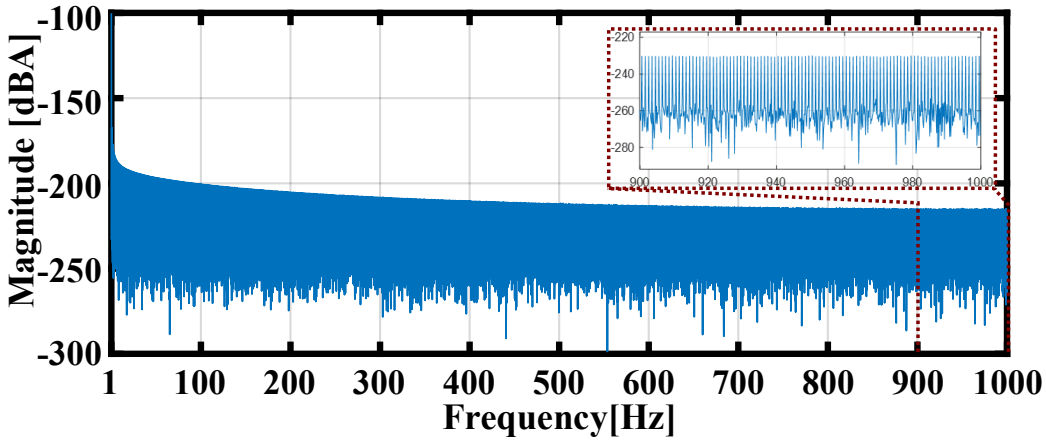
AC small-signal impedance looking into the working electrode, which is expressed by $R_{ct}/[1 + QR_{ct}(j\omega)^{\gamma}]$.

The feedback resistor, R_f, is determined by analyzing two noise-related aspects: (i). the SNR between the sensor's DC bias current, I_{sensor}, and the circuit's in-band integrated noise as expressed in (4.20), and (ii). the SNR of the highest-frequency harmonic in the TIA output relative to the noise floor, determined via an FFT.

The parameters I_{sensor}, R_{ct}, and CPE are obtained by selecting different DC operating points in the Verilog-A model fitted to the data in Figure 4.3. For noise integration, the bandwidth is chosen to be 0.1 Hz to 1 kHz, which is twice the range of 0.1 Hz to 500 Hz for the target UMB sensor in this work



(a).



(b).

Figure 4.15. The noise analysis considering the FFT demodulation; (a). the simulated time-domain response of the Verilog-A model, with a DC potential ($V_{WE} - V_{RE}$) of 155 mV, and an AC amplitude of 40 mV, and (b). the FFT results of the current, by converting the TIA output with an R_f of 4 $MOhm$.

$$SNR = 10\log_{10}\left[\frac{I_{sensor}^2}{\int_{\omega_b}^{\omega_h}\overline{I_{n,TIA}^2}}\right] \geq 40, \tag{4.20}$$

where $\int_{\omega_b}^{\omega_h}\overline{I_{n,TIA}^2}$ is the in-band integrated noise power of the TIA, and ω_b and ω_h represent the angular frequencies corresponding to the lower and higher bounds of the target bandwidth, respectively.

The SNR was simulated by sweeping R_f from 1 MOhm to 20 MOhm at five DC sensor biases (0.125 V, 0.135 V, 0.155 V, 0.175 V and 0.185 V), covering the sensor linear region as discussed in Section 4.2.3. The in-band integrated noise is designed to be 40 dB lower than the sensor DC current power, I_{sensor}^2, to enable robust performance. The simulated SNR results, shown in Figure 4.14(a), indicate that a R_f value of at least 4 MOhm is required to achieve an SNR exceeding 40 dB.

To evaluate the SNR of the highest harmonic relative to the noise floor after performing an FFT on the TIA output, a sensor DC bias of $E_{1/2}$= 155 mV, and a 40 mV peak-to-peak, 50% duty-cycle square wave (period of 2 s) were applied to the model for three cycles. The R_f was set to 4 MOhm for the worst-case scenario identified previously, and the TIA output was sampled at 2 kHz. The applied signal to the Verilog-A model and the TIA output in time-domain are shown in Figure 4.15 (a), and the FFT of the resulting current with non-zero padding is shown in Figure 4.15(b), where the SNR between the smallest harmonic at 500 Hz and the noise floor is approximately 28 dB, thereby ensuring accurate detection for the proposed EIS technique.

The stability and bandwidth of the TIA restrict the decision of C_f and R_f, and a simplified equivalent model for the stability and bandwidth analysis is shown in Figure 4.13(b). The Verilog-A model provides a more realistic sensor behavior for simulations; however, due to the fact the CPE contains a fractional term, $(j\omega)^{\gamma}$, no analytical solution in terms of frequency response can be obtained for a straightforward analysis. Therefore,

the CPE in circuit analysis calculation is expressed with an equivalent capacitor, C_{eq}, aimed to provide an "intuitive" design trade-off.

The loop gain without a compensation capacitor, $LG_{w/o,C_f}$, as described in (4.21), indicates that two poles located at $1/2\pi R_{out}C_{load}$ and $(1+R_f/R_{ct})/2\pi R_f C_{eq}$ yield poor stability.

$$LG_{w/o,C_f} = A_v(j\omega)\,\beta(j\omega) = \frac{A_{op}}{(1+j\omega R_{out}C_{load})} \cdot \frac{1}{\left[\left(1+\frac{R_f}{R_{ct}}\right)+j\omega R_f C_{eq})\right]} \tag{4.21}$$

where $A_{op}(j\omega)$ is the gain of the amplifier, which is designed to be a first-order linear system within the Unit Gain Bandwidth (UGB). A_{op}, R_{out} and C_{load} are the DC gain, equivalent output resistance and load capacitance of the amplifier respectively.

It can be seen that the instability occurs at the intercept frequency, f_{int}, when $A_v(j\omega) = 1/\beta(j\omega)$, as is expressed in (4.22), assuming A_{op} is large.

$$f_{int} \approx \frac{1}{2\pi}\sqrt{\frac{A_{op}}{C_{eq}R_f C_{load}R_{out}}} \tag{4.22}$$

The compensation capacitor, C_f, introduces a zero of $1/2\pi C_f R_f$ for TIA compensation, and the loop gain of the TIA with C_f is expressed with (4.23):

$$LG_{w/,C_f} = \frac{A_{op}R_{ct}\left(1+j\omega C_f R_f\right)}{\left(R_f+R_{ct}+j\omega\left(C_f+C_{eq}\right)R_f R_{ct}\right)(1+j\omega C_{load}R_{out})}. \tag{4.23}$$

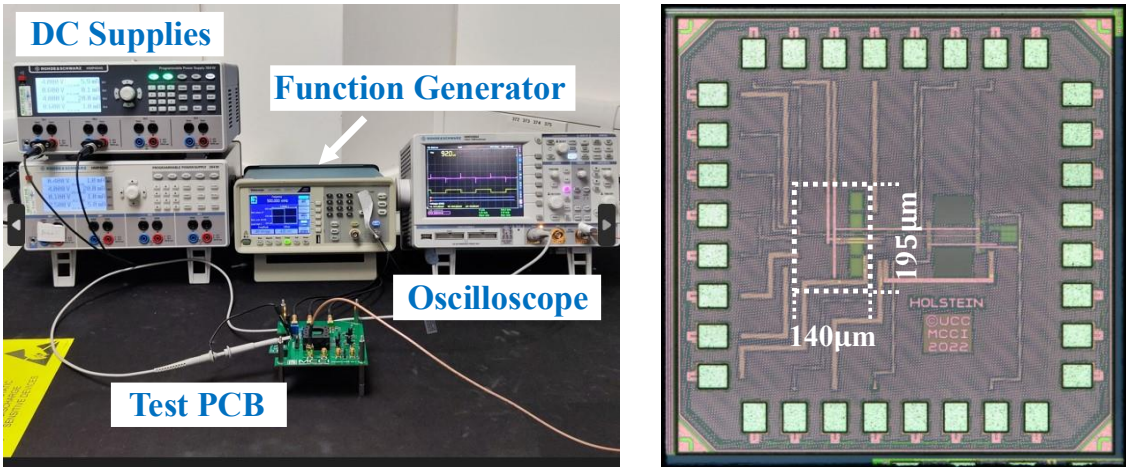
Consequently, the zero of the TIA should be placed before the intercept frequency f_{int}, namely, $1/2\pi C_f < f_{int}$, where the feedback capacitor is thus determined by (4.24):

$$C_f \geq \sqrt{\frac{C_{eq}C_{load}R_{out}}{A_{op}R_f}}. \tag{4.24}$$

By evaluating the transfer function of the TIA, the 3-dB bandwidth, f_{3db}, is obtained by examining its dominant pole, as is expressed in (4.25), if the TIA is overcompensated.

In practice, considering variations in the CPE across different chemical tests, C_f should be chosen to exceed $\sqrt{C_{eq}C_{op}R_{op}/A_{op}R_f}$ substantially for overcompensation, and the CPE should be set to a relatively large value when designing circuity with simulations. For UMB electrode sensors, the values of Q and γ of CPE are empirically chosen to be 10 nF and 0.8 respectively, and the CPE is approximated in a frequency range of 0.0001 Hz to 1 GHz for stability and bandwidth simulations. It can be observed from (4.22) and (4.25) that the sensor small-signal charge-transfer resistance has negligible impact on stability and bandwidth; hence the R_{ct} is fixed at a DC bias of 0.155 V in the Verilog-A model (the middle of the sensor linear region). A stability analysis and an AC small-signal analysis are performed by sweeping R_f from 4 MOhm to 20 MOhm with C_f in a range of 1 pF to 10 pF. The simulated results of transimpedance gain, loop gain, loop phase, amplifier gain, and $1/\beta$ are shown in Figure 4.14(b), with an R_f and C_f of 10 MOhm and 5 pF respectively, and a valid bandwidth of 3.3 kHz with overcompensation.

$$f_{3db} \approx \frac{1}{2\pi C_f R_f} \tag{4.25}$$



(a). (b).

Figure 4.16. The measurement setup and the die micrograph: (a). The test setup, and (b). the die micrograph.

4.4. Experimental Results

The designed chip was fabricated in a 65 nm CMOS technology with an active area of 140 µm × 195 µm. The sensor excitations for both CV and square-wave EIS are generated using a Tektronix AFG1062. The potentials of the RE (as the sensor input) and the TIA output are synchronously sampled by a Rohde & Schwarz HMO3004, serving as an Analog-to-Digital Convertor (ADC). The test setup and the die micrograph are shown in Figure 4.16(a) and (b).

4.4.1. Electrical Validation of the Chip with Dummy Sensor

Electrical validation of the chip is performed using a dummy sensor, where $R_{ct} = 50$ MOhm and $C_{eq} = 1$ nF, as is shown in Figure 4.17. A 5 MOhm resistor is added in the signal path to prevent the low impedance looking into the dummy sensor. A square wave

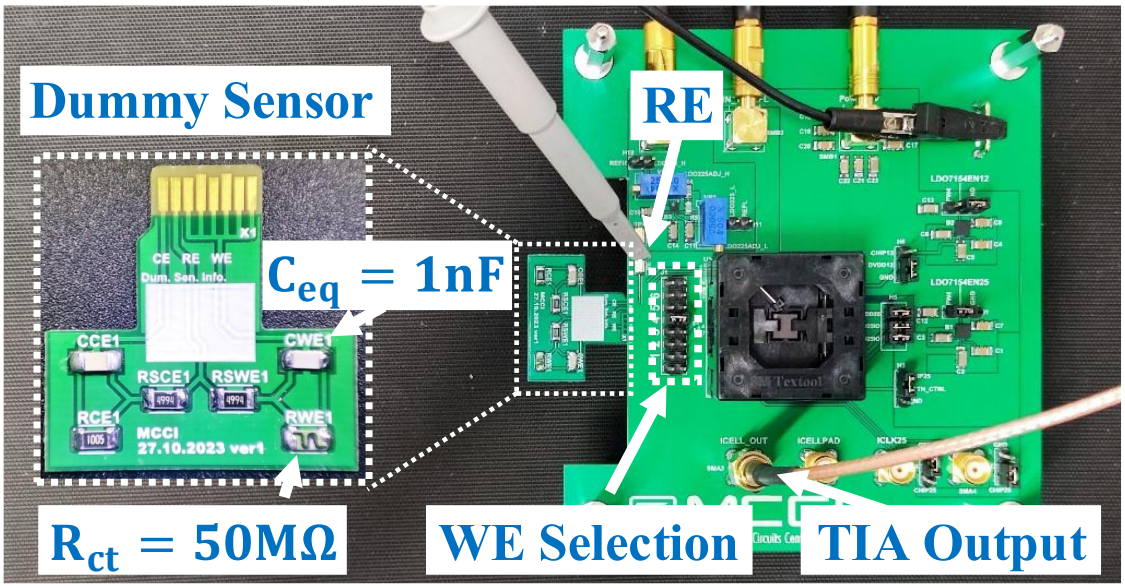


Figure 4.17. The PCB setup for electrical validation, with an R_{ct} = 50 MOhm, and a C_{eq} = 1 nF.

at a frequency of 0.5 Hz with an AC magnitude of 40 mV is applied to the dummy sensor via a function generator Tektronix AFG1062, and the signals at the RE and TIA output are sampled via Rohde & Schwarz HMO3004 at a sampling rate of 1 kHz. The dummy sensor current, I_{dum}, is given by (4.26):

$$I_{dum}(t) = -\frac{V_{TIA,out}(t)}{R_f} + \frac{V_{CM,TIA}}{R_f} \tag{4.26}$$

where $V_{TIA,out}(t)$ is the TIA output and $V_{CM,TIA}$ is the TIA common-mode DC level.

Figure 4.18 shows the time-domain sampled input and output signals, and Figure 4.19 (a) shows the FFT results of the applied potential at RE, and Figure 4.19(b) shows the FFT results of the TIA output. Figure 4.20 compares the dummy sensor's square-wave-based EIS measurement results with simulated EIS data. It can be observed that the

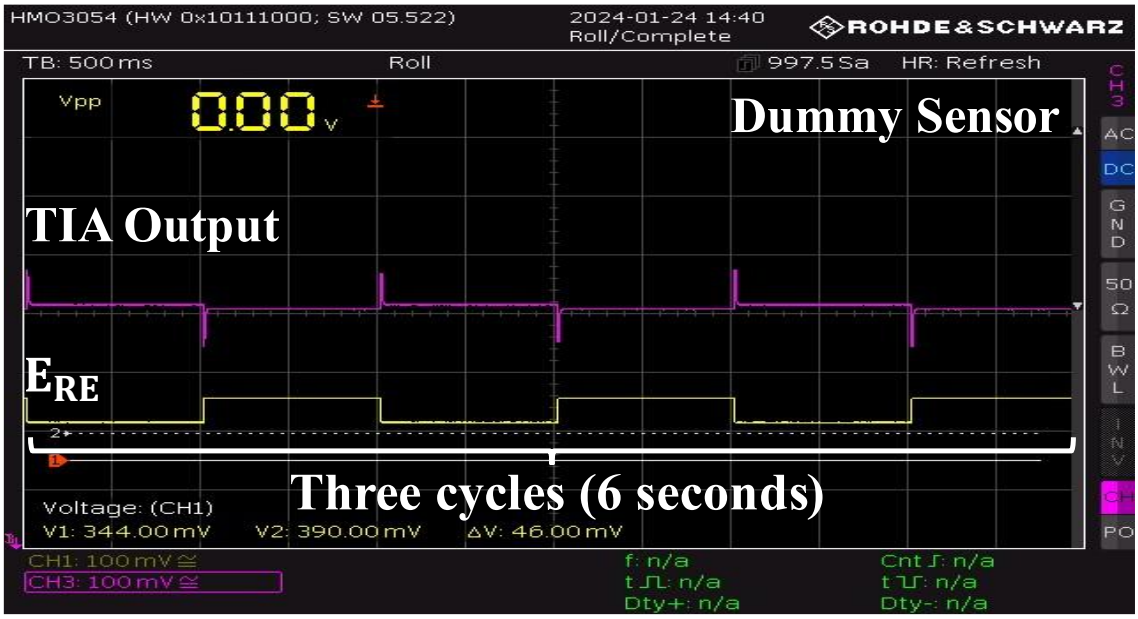


Figure 4.18. The time-domain results of the sensor input and TIA output for a dummy sensor, with an R_{ct} = 50 MOhm, and a C_{eq} =1 nF.

highest frequency harmonic is at 500 Hz, with a magnitude of -230 dBA of the sensor output, and a magnitude of --95 dBV of the applied potential. At higher frequency, the SNR becomes worse due to the decreasing amplitude of the square wave harmonics, while the close agreement between the tested EIS and simulated EIS confirms that the designed potentiostat and TIA satisfy the expected bandwidth, noise, and stability requirements, but limits the frequency band to 500 Hz as target.

4.4.2. The Pre-modification of the UMB Electrodes

Five pre-modified WEs, denoted as E1 to E5, featuring progressively thicker gold deposits that decrease R_{ct} while increasing the CPE, are tested across 1 mM to 4 mM concentrations of FcCOOH at room temperature for validating the feasibility of the proposed square-wave EIS for biomedical applications.

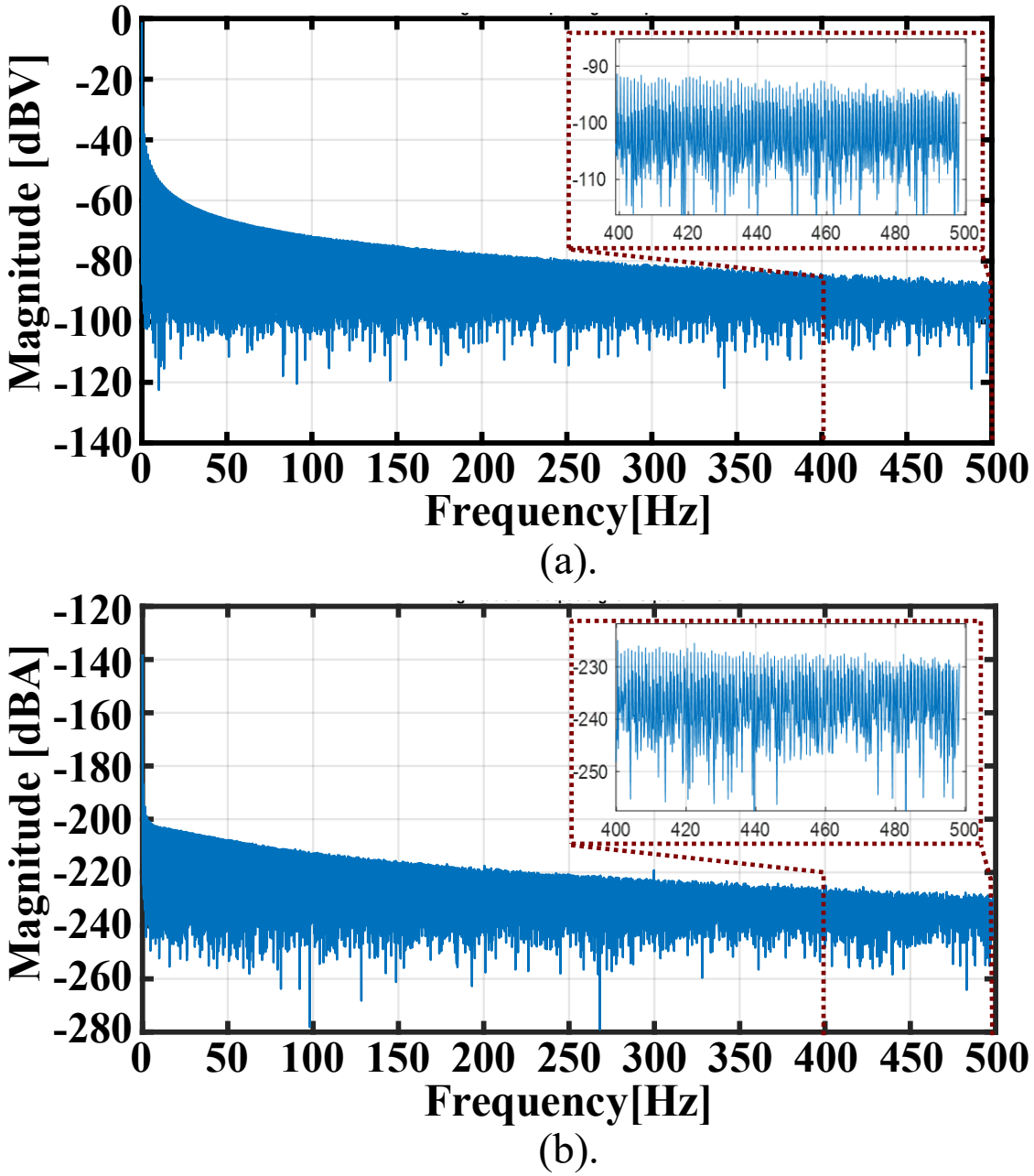


Figure 4.19. The FFT results of the measured square-wave EIS, with an applied 0.5 Hz, 40 mV swing square wave to a dummy sensor: (a). the FFT results of the applied potential at RE, and (b). the FFT results of the current converted from TIA output.

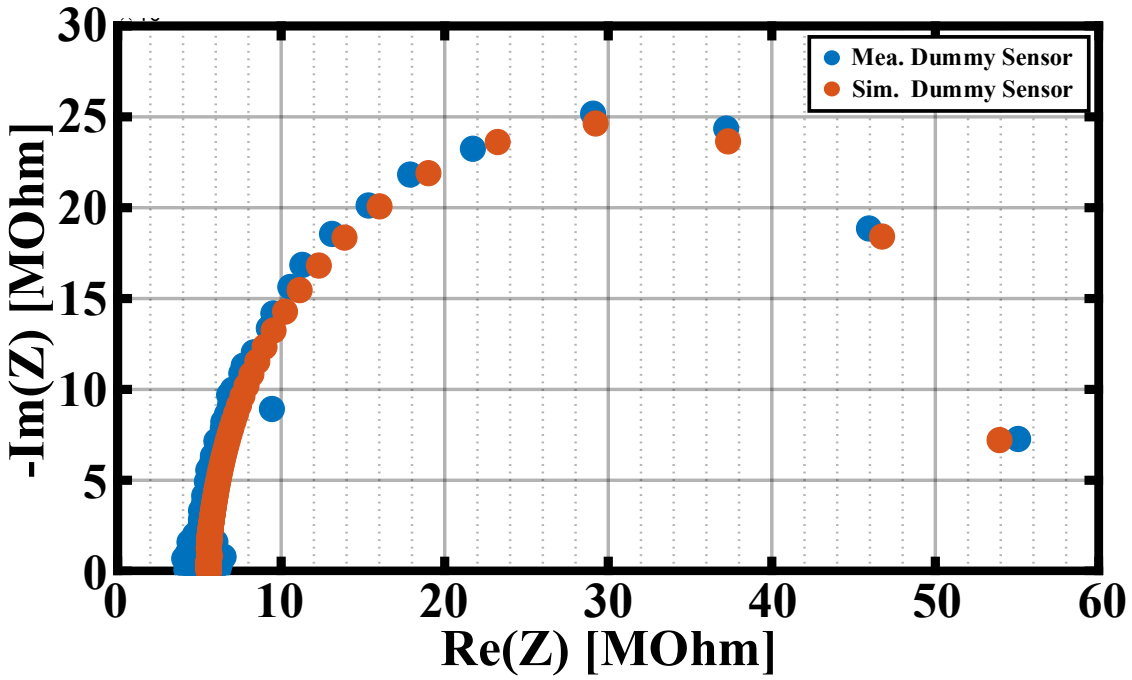


Figure 4.20. The chip-tested results of square-wave EIS and simulated results of a dummy sensor, with an $R_{ct} = 50$ MOhm, and a $C_{eq} = 1$ nF.

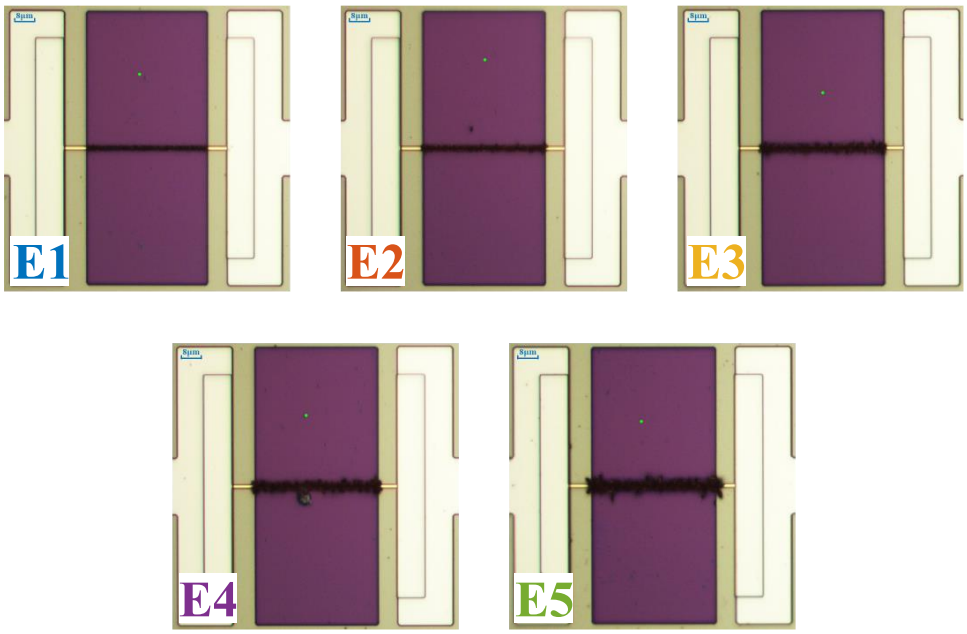


Figure 4.21. Microscopic images of five electrodes with different deposited thicknesses of gold.

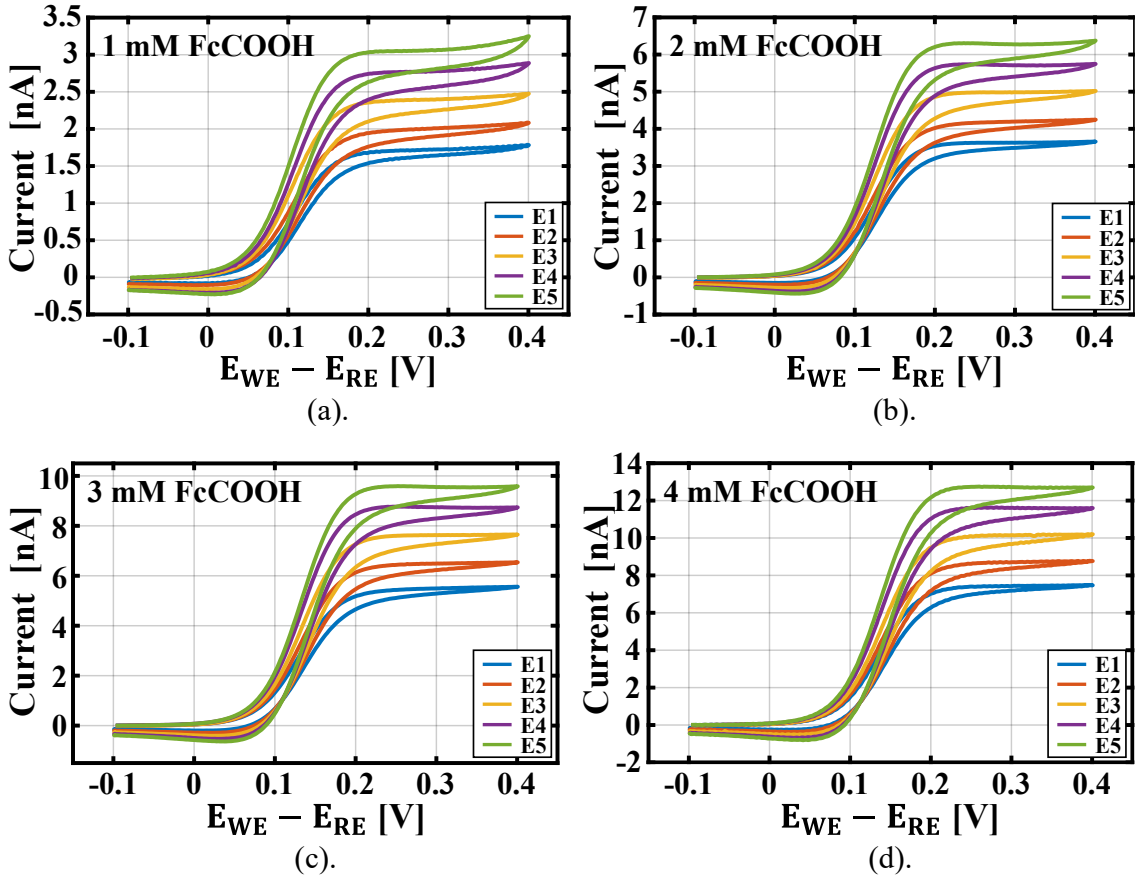


Figure 4.22. The CV results performed by AutoLab in (a). 1 mM FcCOOH, (b). 2 mM FcCOOH, (c). 3 mM FcCOOH, and (d). 4 mM FcCOOH, in a 10 mM PBS supporting electrolyte at 25°, with a SR of 50 mV/s from -0.1 V to 0.4 V, showing different electrode characteristics for the electrochemical validation.

The pre-modification of the electrode involves the deposition of gold (Au) onto the electrode surface, which yields different characteristics for both the CPE and R_{ct}. The deposition occurs in the solution dissolving 5 mM $HAuCl_3$in 0.25 M H_2SO_4 at 25°. The chemical formula of this reaction is described by (4.27):

$$Au^{2+} + 2e^{-} \rightarrow Au. \tag{4.27}$$

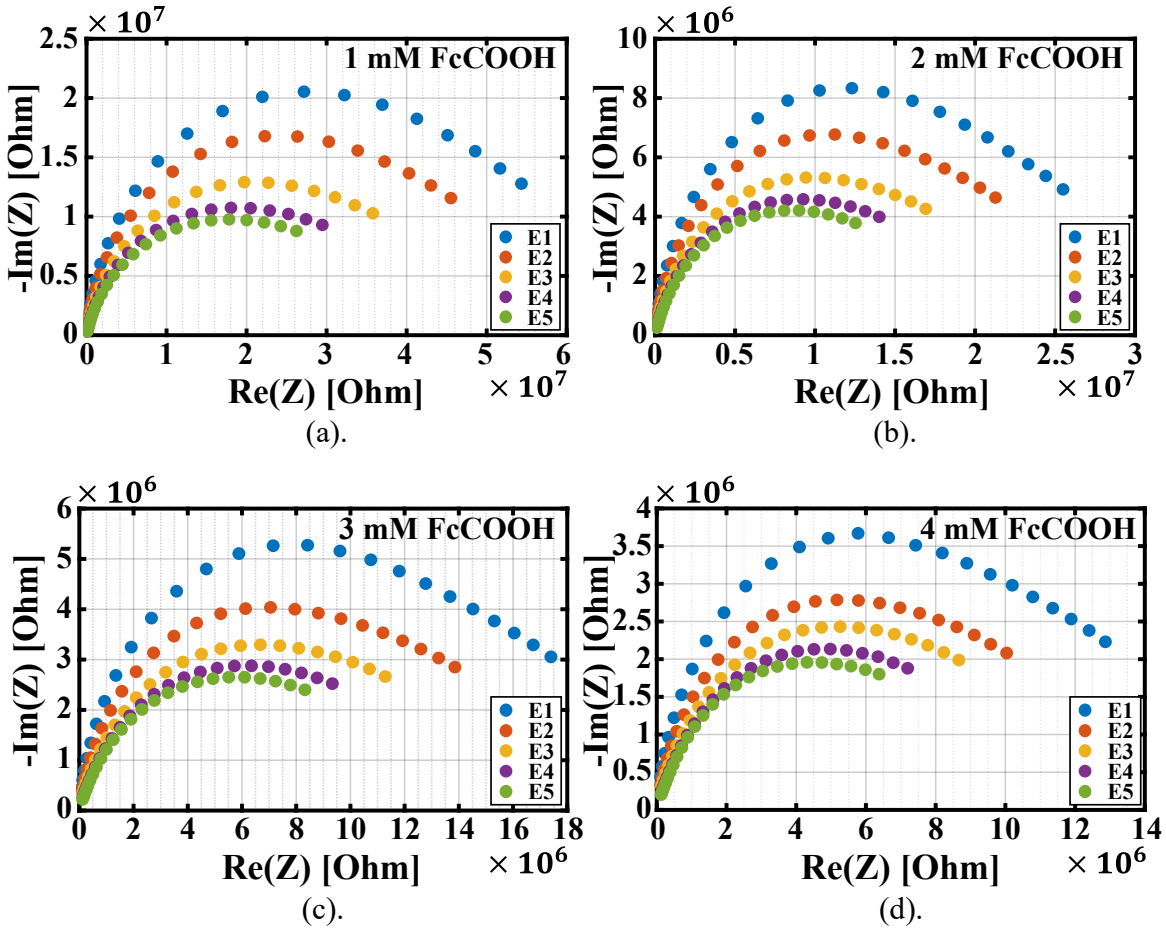


Figure 4.23. The EIS results performed by AutoLab in (a). 1 mM FcCOOH, (b). 2 mM FcCOOH, (c). 3 mM FcCOOH, and (d). 4 mM FcCOOH, in a 10 mM PBS supporting

The deposition is done with Chronoamperometry based on AutoLab, where the thickness is controlled by the deposition duration with a given fixed electrode potential (-0.1V this case). In this test, five UMB electrodes, designated E1 to E5, are deposited with five different durations: 4s, 8s, 10s, 14s and 18s, respectively. The microscopic images of the electrodes, E1 to E5, after the deposition are depicted in Figure 4.21

CV and EIS are then conducted using AutoLab to inspect the performance of the deposited UMB electrodes. Figure 4.22(a) to (d) show the CV results of each deposited

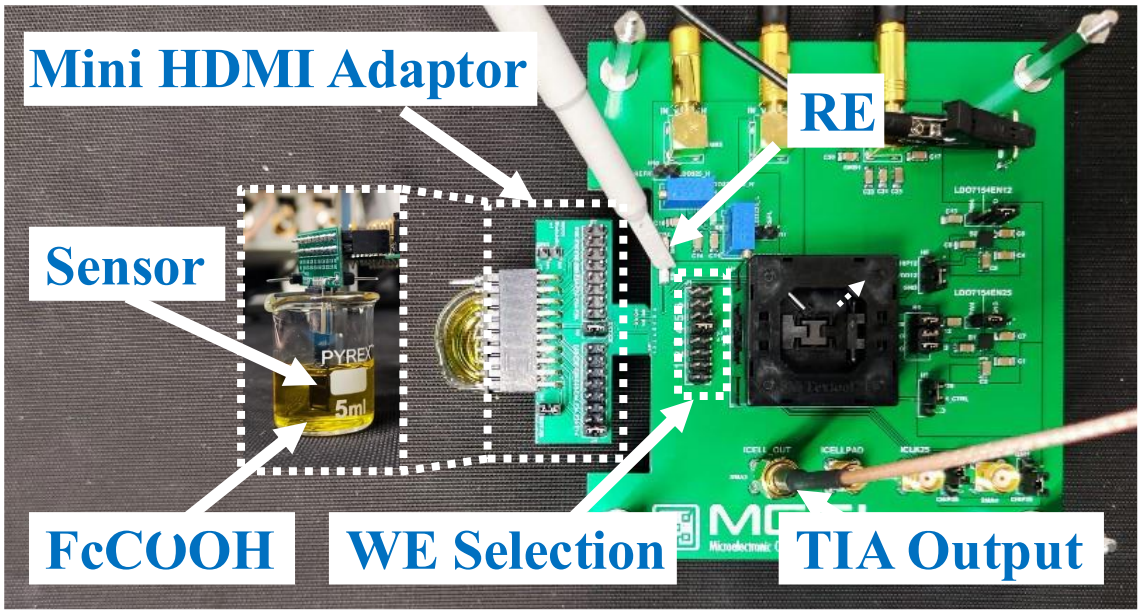


Figure 4.24 The PCB setup for chemistry test with deposited UMB electrodes.

electrode across 1 mM to 4 mM concentrations of FcCOOH in a 10 mM PBS supporting electrolyte at 25°, with a SR of 50 mV/s from -0.1 V to 0.4 V, and the EIS measurement results with DC at each $E_{1/2}$ are shown from Figure 4.23(a) to (d). It can be seen that after doing the deposition, five electrodes show different characteristics in different concentration of FcCOOH, which can be used to conduct the electrochemical validation.

4.4.3. Electrochemical Validation of the Proposed Square-wave EIS with Pre-deposited UMB Electrodes

The test setup for the electrochemical validation of the proposed square-wave EIS is shown in Figure 4.24. The sensor communicates with the designed chip through a Micro-SD-to-Mini-HDMI PCB adaptor.

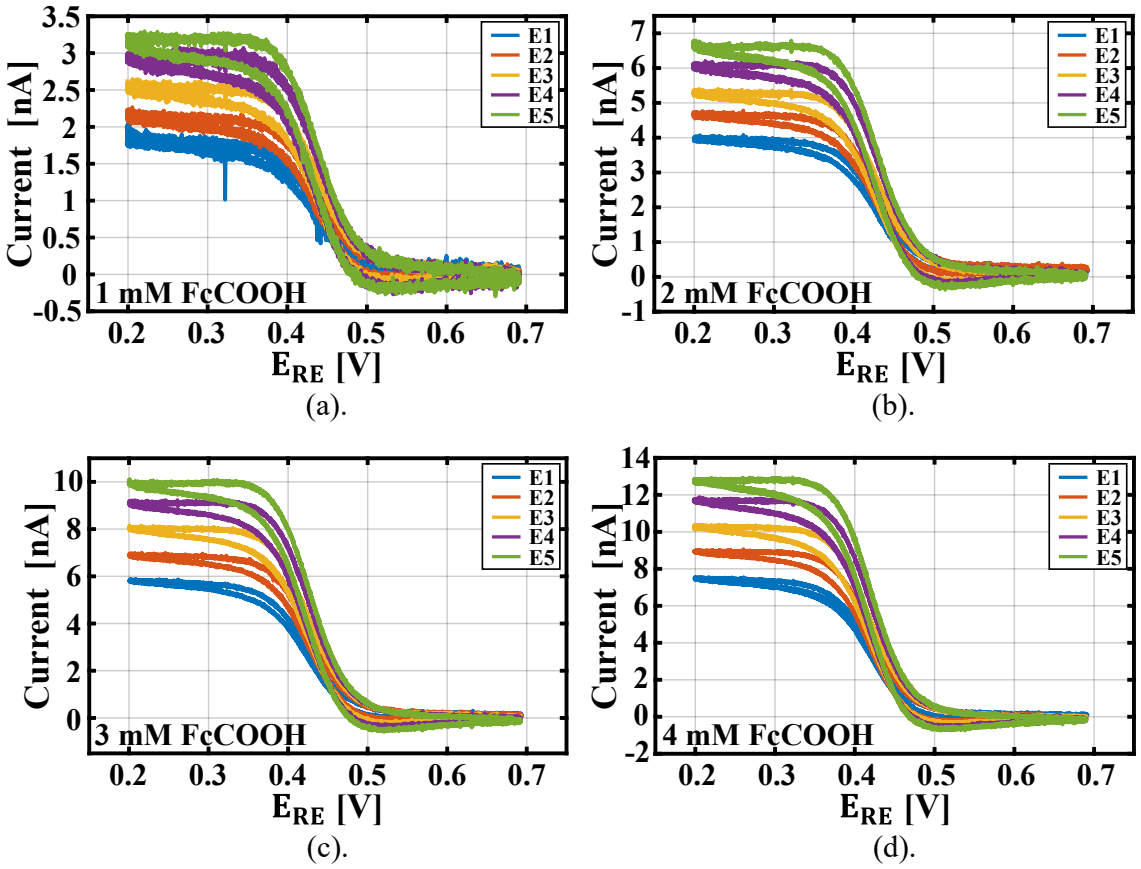


Figure 4.25. The chip-tested results of CV across (a). 1 mM FcCOOH, (b). 2 mM FcCOOH, (c). 3 mM FcCOOH, and (d). 4 mM FcCOOH, in a 10 mM PBS supporting electrolyte at 25°, with a SR of 50 mV/s for electrode potential from -0.1 V to 0.4 V. The results shows that the UMB sensor is working as expected.

In the measurement of CV, a triangle wave at a frequency of 0.05 Hz is applied, which ensures the potential of the WE has a scan rate of 50 mV/s sweeping from -0.1 V to 0.4 V with respect to the TIA common mode potential, 0.6 V. The chip-tested results of CV across 1 mM to 4 mM FcCOOH are shown from Figure 4.25(a) to (d), and the DC bias of the sensor is chosen where the conductance of the sensor reaches minimum, namely, the half potential, and the AC amplitude is chosen to be 40 mV as mentioned in Section 4.2.3, where the sensor works in a linear region, as shown in Figure 4.26(a) to (d).

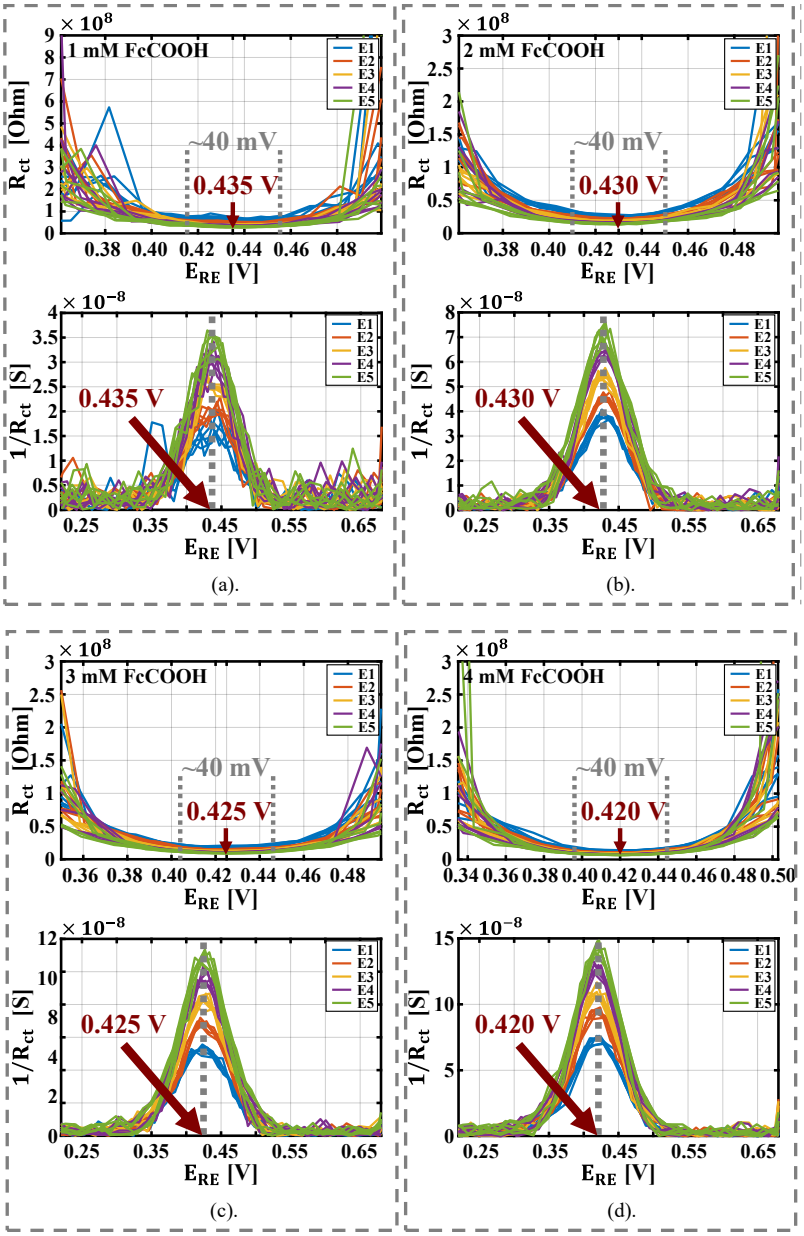


Figure 4.26. The determination of AC and DC conditions for square-wave EIS across a). 1 mM FcCOOH, b). 2 mM FcCOOH, c). 3 mM FcCOOH, and d). 4 mM FcCOOH, in a 10 mM PBS supporting electrolyte at 25°. The DC bias of the sensor is chosen where the conductance of the sensor reaches minimum, namely, the half potential, and the AC amplitude is chosen to be 40 mV as mentioned in Section 4.2.3, where the sensor working in a linear region.

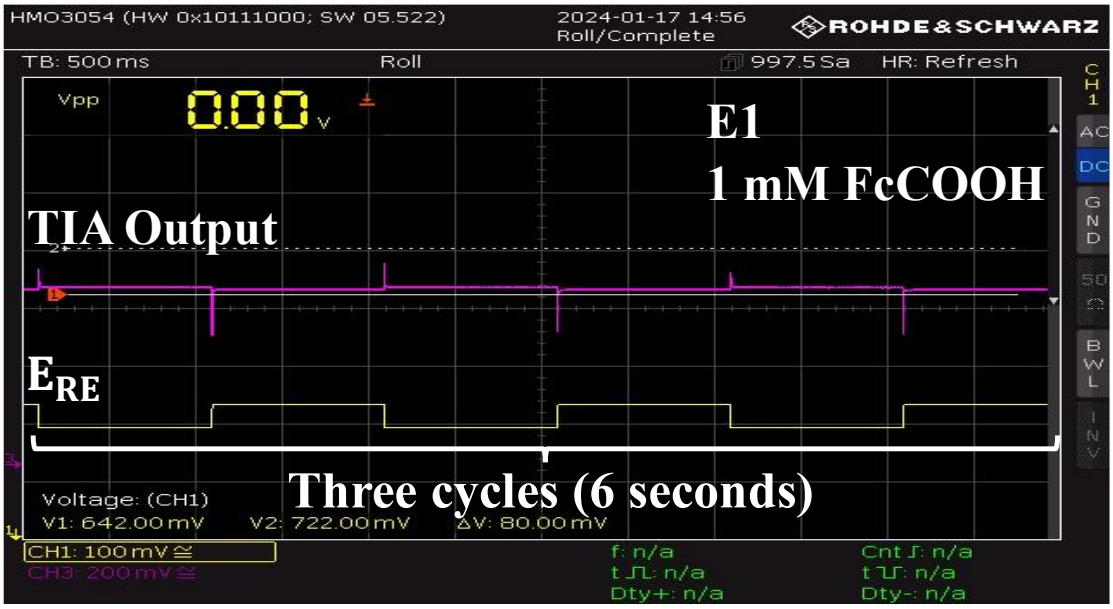


Figure 4.27. The time-domain results of the sensor input and TIA output for E1.

The frequency of the square wave for EIS is chosen to be 0.5 Hz and the swing of the square wave is 40 mV. The input and output are sampled for three cycles with a sampling rate of 1,000 samples per second for a Nyquist bandwidth of 500 Hz. The time-domain chip-tested results of E1 in 1 mM FcCOOH are shown in Figure 4.27, and FFT results of E1 in 1-4 mM FcCOOH are shown in Figure 4.28, then the same measurement is repeated for the remaining electrodes and concentrations. It can be seen that, for the E1 in 1 mM FcCOOH, the highest frequency harmonic is at 500 Hz, with a magnitude -218 dBA of the sensor output, and a magnitude of - 95 dBV of the applied potential. Figure 4.29(a) to (d) compare the tested square wave EIS, the traditional EIS from Autolab, and the fitted EIS model for five electrodes across four FcCOOH concentrations. The optimized fitted EIS model is obtained using AutoLab based on the traditional EIS.

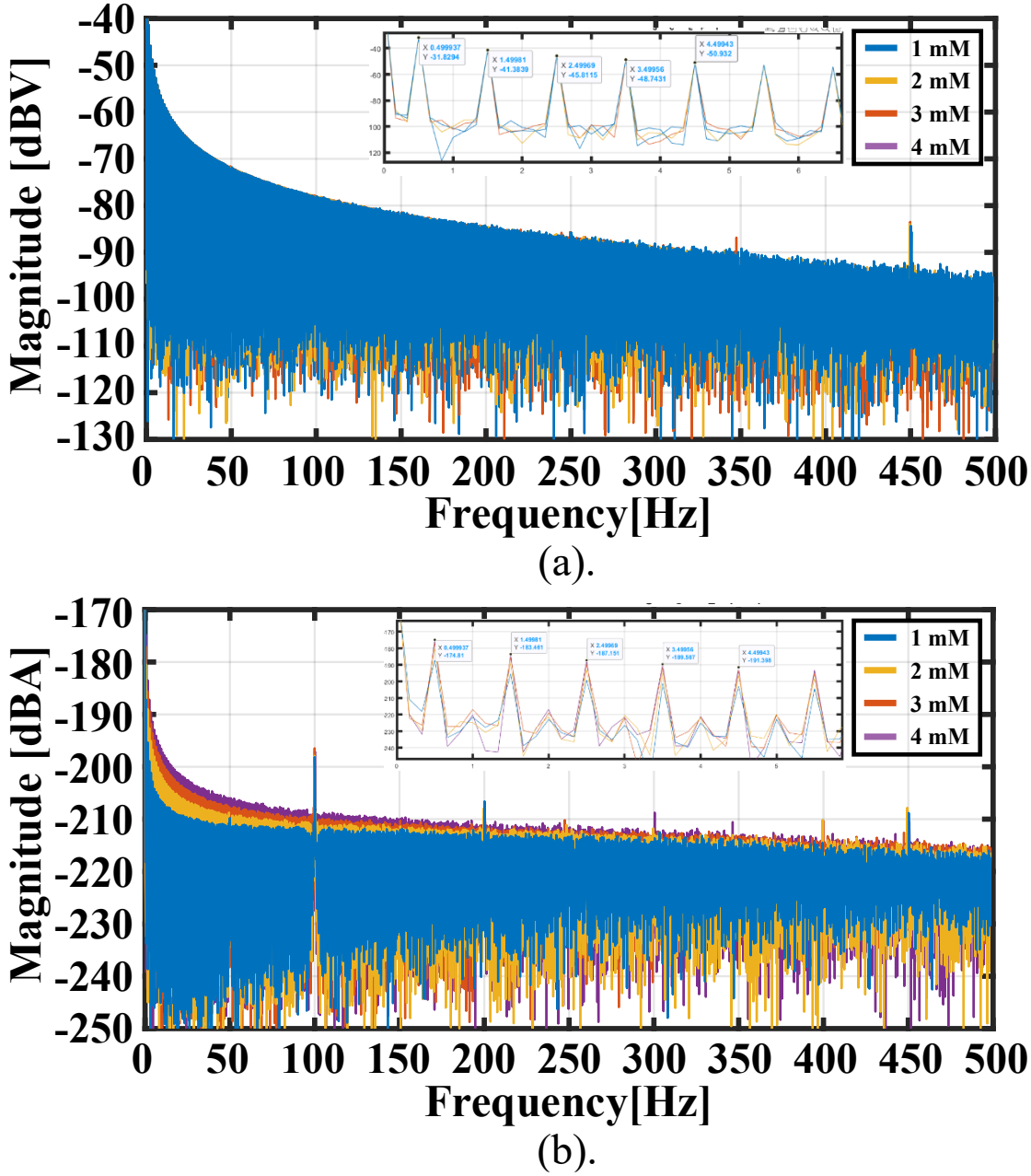
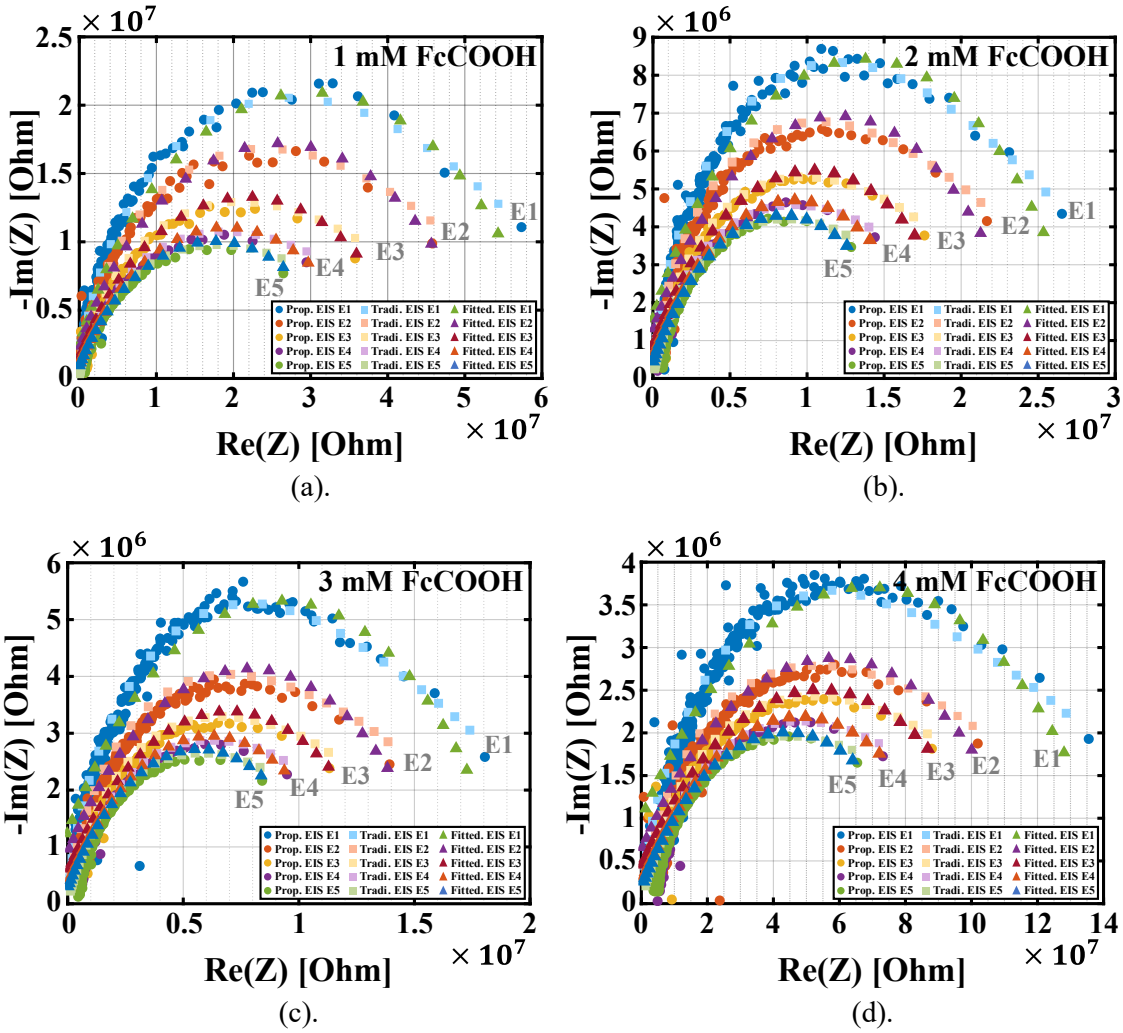


Figure 4.28. The FFT results of the chip-measured square-wave EIS with E1 in 1 - 4 mM FcCOOH: (a). the FFT results of the applied potential at RE, and (b). the FFT results of the current converted from the TIA output



(a). (b). (c). (d).

Figure 4.29. The comparison of EIS results of the square wave EIS, the traditional EIS performed by AutoLab, and the EIS optimized fitted model. The square wave EIS and the traditional EIS employ the same AC and DC conditions as indicated in Figure 4.26.

It can be seen that the proposed chip-tested square wave EIS has high consistency with the traditional EIS based on AutoLab, while only consuming 6 seconds, shortened by 91.7% from 72 seconds in a conventional way [114].

4.5. Error Evaluation

The error was investigated by comparing the absolute difference between the Mean

Absolute Percentage Error (MAPE) of traditional EIS and the model fitted using traditional EIS data, against the MAPE between square wave EIS and the model fitted using traditional EIS, as expressed in (4.28):

$$Error = \left| \underbrace{\frac{1}{m}\sum_{i=1}^{m}\left|\frac{Z_{i,fit.} - Z_{i,mea.}}{Z_{i,fit.}}\right|}_{\substack{\text{MAPE1:} \\ \text{Traditional EIS vs. fitted model}}} - \underbrace{\frac{1}{n}\sum_{j=1}^{n}\left|\frac{Z_{j,fit.} - Z_{j,mea.}}{Z_{j,fit.}}\right|}_{\substack{\text{MAPE2:} \\ \text{Proposed EIS vs. fitted model}}} \right| \cdot 100\% \quad (4.28)$$

where m and n are the number of the frequencies in traditional EIS data and square wave EIS data, respectively. $Z_{i,mea.}$ and $Z_{j,mea.}$ represent the measured impedance magnitudes of the traditional EIS and square wave EIS, respectively, where $i \in [1, m]$ and $j \in [1, n]$ are integer numbers. $Z_{i,fit}$ and $Z_{j,fit}$ represent the calculated impedance magnitudes from the optimized fitted EIS model. The calculated errors are listed in Table IV.

It can be seen that the average MAPE between chip-tested square-wave EIS and the traditional EIS conducted by the commercial instrument AutoLab is 2.73%, and the measurement time is reduced by 91.7% (from 72 seconds to 6 seconds), 12 times faster than single frequency sweep. Compare to other relevant published works shown in Table V, the proposed square wave EIS shows fair competitive coherency and accuracy but much less measurement time. These tested results successfully validate the feasibility for applying the proposed square-wave EIS technique to portable, real-time label-free impedance-based biomedical applications.

Table IV. Error evaluation

		MAPE1 (%)	MAPE2 (%)	Error (%)
1mM	E1	13.27	10.95	2.32
	E2	13.47	13.49	0.02
	E3	11.31	10.82	0.49
	E4	10.44	13.23	2.79
	E5	9.60	9.20	0.40
1 mM Ave.			**1.20**	
2mM	E1	11.35	15.26	3.91
	E2	10.87	13.05	2.18
	E3	8.52	9.41	0.89
	E4	7.09	8.33	1.24
	E5	6.52	8.84	2.32
2 mM Ave.			**2.11**	
3mM	E1	9.79	16.25	6.46
	E2	8.71	7.57	1.14
	E3	5.88	8.91	3.03
	E4	4.85	10.40	5.55
	E5	4.53	9.81	5.28
3 mM Ave.			**4.29**	
4mM	E1	8.46	13.42	4.96
	E2	7.20	7.98	0.78
	E3	4.74	7.38	2.64
	E4	3.64	7.44	3.80
	E5	3.54	7.99	4.45
4 mM Ave.			**3.33**	
Total Ave.			**2.73**	

Table V. Comparison with relevant published works

	[27]	[31]	[28]	[30]	[88]	[20]	[37]	[34]	[36]	[94]	[95]	[96]	[97]	This work
Technology	0.13 µm	0.5 µm	130 nm	180 nm	0.35 µm	N/A	N/A	N/A	N/A	40 nm	N/A	N/A	0.11 µm	**65 nm**
Supply Voltage	1.2 V	3 V	0.6 V	1.8 V	3.3 V	N/A	N/A	N/A	N/A	0.9 V	N/A	N/A	1.2 V	**2.5 V**
Power	0.35 mW	6 µW	14.6 µW	344.3 µW to 479.3 µW	0.32 mW	N/A	N/A	N/A	N/A	135 µW	N/A	14.4 mW	1.28 mW	**1.25 mW / Amplifier**
Core Area	1.68 mm²	0.06 mm²	0.004 mm²	5.4 mm²	0.07 mm²	N/A	N/A	N/A	N/A	0.6 mm²	N/A	N/A	6 mm²	**0.027 mm²**
Excitation Type	Sinusoidal	Sinusoidal	Sinusoidal	Sinusoidal	Sinusoidal	Multi-sine Excitation	Chirp signals	Structured Gaussian White Noise	Pseudo-Random Binary Sequence	Square-wave (i)	Square-wave (i)	Square-wave (i)	Square-wave (i)	**Square-wave (v)**
Signal Generation	On-chip 8-bit R-2R DAC and SRAM	External Signal Generator	External Signal Generator	On-chip Direct Digital-Synthesis	External Signal Generator	External Signal Generator	External Signal Generator	External Signal Generator	External Signal Generator	External Signal Generator	External Signal Generator	External Signal Generator	On-Chip Switched Current Stimulus	**1-bit DAC (External Signal Generator)**
Chemical Verification	Yes (Potassium Ferricyanide DNA)	Yes (Protein)	Yes (Potassium)	Yes (Biological Tissue)	Yes (ZoBell's ORP/redox Standard Solution and Melatonin Solutions)	Yes (18650-29E Battery)	Yes (Sealed Lead Acid battery and Lithium Nickel-Cobalt Anganese Oxide)	No	Yes (Lithium-iron-phosphate and Battery cell)	Yes (Biological Tissue)	Yes (Biological Tissue)	Yes (Biological Tissue)	Yes (Biological Tissue)	**Yes (Ferrocene Carboxylic Acid)**
Measurement Time	N/A	N/A	N/A	N/A	N/A	N/A	5-12 times faster than single-sine frequency sweep	**6.08 times faster than single-sine frequency sweep**	**12 times faster than single-sine frequency sweep**	N/A	N/A	N/A	N/A	**12 times faster than single-sine frequency sweep**
Error	**8.4% (Real) 7.5% (Imag) (Relative Error, Impedance Model)**	N/A	< 2%	< 3%	0.28% (Mag., 10 kHz) 0.12% (Pha., 10 Hz) (RMS Error)	< 4.5%	N/A	**< 2.69% (Relative Error)**	**< 8.3% (RMS)**	N/A	< 1% (Mag.) < 0.5° (Pha.)	7.2%	N/A	**2.73% (MAPE)**

4.6. Conclusion

This work demonstrates a square wave-based EIS method with the advantages of simplicity of implementation and fast measurement time. The theories under which the sensor is linearized as an LTI system lay the groundwork for using square wave as the EIS excitation signal, also potentially bringing opportunities for novel EIS circuitry. The successful validation of the proposed EIS on a taped-out chip yields an average MAPE of 2.73%, compared to the results from a commercial instrument, while the measurement time is shortened to 6 seconds from 72 seconds, by 91.7%, in a frequency range of 0.5 Hz to 500 Hz. The high accuracy and fast measurement time ensure the feasibility for applying this technique to portable, real-time impedance-based biomedical applications.

Chapter 5

5. Discussion and Future Work

5.1. Contributions/Outputs of this Work

This study proposes a novel EIS methodology that employs a square-wave excitation signal. Experimental results demonstrate that the proposed method achieves faster measurement times and high accuracy compared to those obtained with a commercial chemical analysis instrument, indicating its potential for application in advanced EIS circuit designs.

Furthermore, this study presents a dynamic model of a UMB-electrode electrochemical sensor implemented in Verilog-A, which supports different simulations. This model is able to reproduce the sensor's dynamic behavior, thereby facilitating the design of high-precision electrochemical sensor interfaces.

The outputs of this work:

1. **Z. Wang**, A. Murphy, A. O'Riordan, and I. O'Connell, "Equivalent Impedance Models for Electrochemical Nanosensor-Based Integrated System Design," *Sensors (Basel, Switzerland)*, vol. 21, no. 9, 2021, doi: 10.3390/s21093259.
2. **Z. Wang**, A. Wall, A. O'Riordan, D. O'Hare, G. M. Salgado, and I. O'Connell, "Models and Interfaces for Electrochemical Sensors: Architectures and

Implementations," in *Biomedical Electronics, Noise Shaping ADCs, and Frequency References*, P. Harpe, A. Baschirotto, and K. A. Makinwa, Eds., Cham: Springer International Publishing, 2023, pp. 79–103.

3. **Z. Wang**, H. Shao, A. O'Riordan, J. Higes-Marquez, I. O'Connell, and D. O'Hare, "A Fast Square Wave-based Electrochemical Impedance Spectroscopy for Impedance-based Biomedical Applications," in *2024 IEEE Biomedical Circuits and Systems Conference (BioCAS)*, Xi'an, China, 2024, pp. 1–5.

4. **Z. Wang**, H. Shao, A. O'Riordan, J. Higes-Marquez, I. O'Connell, and D. O'Hare, "A Fast Square Wave-based Electrochemical Impedance Spectroscopy for Impedance-based Biomedical Applications," in *IEEE Trans. Biomed. Circuits Syst.*, vol. xx, no. x, pp. xxx–yyy, 2025. (**Under Review**)

5. X. Chen, T. Siriburanon, **Z. Wang**, J. Du, Y. Hu, A. Zhu, "A Digital-to-Time Converter Based on Crystal Oscillator Waveform Achieving 86-fs Jitter in 22-nm FD-SOI CMOS," in *2022 IEEE Radio Frequency Integrated Circuits Symposium (RFIC)*, Denver, CO, USA, 2022, pp. 319–322.

5.2. The Applicability of the Proposed Square Wave-based EIS.

The accuracy and feasibility of the proposed square wave-based EIS for biomedical applications are validated with UMB electrode sensors, whose charge-transfer rate model can be described with Butler Volmer relationships theoretically, owing to its highly

efficient three-dimensional mass diffusion mechanism. In the case of an UMB electrode sensor, a linear region is determined, which provides the applicability of this technique. Based on this fact, it can be inferred that other types of micro electrodes that have highly efficient radial mass diffusion transport, such as micro disk electrodes, can potentially use this technique for performing EIS. However, due to the different electrode shapes, a different charge-transfer rate model should be proposed and validated [101], and further chemical tests would need to be followed. The proposed square-wave EIS provides a new angle to develop new techniques and circuits for conducting fast, and high-accurate EIS with UMB electrode sensors, particularly, for sensor-on-chip and implantable biomedical applications [81, 100, 115–118].

The limited frequency range restricts this technique for wider applications; however, depending on the application, by applying square waves with different frequencies, the frequency range can be extended to enhance spectral coverage. Apart from that, different excitation signals such as a duty-cycle controlled square wave potentially can provide more harmonic tones for wider applications. The AC amplitude used in this work with a UMB sensor is 40 mV, where the sensor shows linearity. Due to the fact that this type of sensor, whose mass transport is dominated by a radial diffusion, the R_{ct} can be fitted with (4.9); therefore, the 40 mV should be applicable as well. However, the like a normal EIS measurement, a CV should be conducted before the EIS test, to find the AC and DC conditions practically, and in order to accommodate different sensors, strategies to optimize the AC amplitude can be investigated further.

5.3. The Impact of the Proposed Verilog-A model.

Owing to the fact that the UMB sensor behavior, namely, the relation between the electrode potential and sensor current, sensor transconductance and impedance, double-layer effect (or CPE), etc., are mathematically modeled, a dynamic Verilog-A model is implemented and utilized in this work. This dynamic model has advantages in accuracy and convenience in terms of the bandwidth and stability analysis, as well as the transient analysis, for designing different potentiostats, such as control amplifier-based potentiostat [119–121], current-mirror-based potentiostat [83], Delta-sigma modulation potentiostat [73, 122], Amplifier-less potentiostat [123, 124], etc., and current readout ICs of UMB electrochemical sensors. However, a future work of modelling different types of electrochemical sensor will popularize this analysis methodology in electrochemical sensor interface design field.

5.4. The Required Specification of the Amplifier and TIA.

The loop gain and its bandwidth are dominated by the pole of the amplifier, and the pole introduced by a low-pass filter formed by the CPE and the feedback network, as described in (4.21). It indicates that a larger electrode active surface, or a higher concentration of the solution may attenuate the loop gain at high-frequency harmonics and cause instability, which ultimately results in errors at the TIA output. Therefore, when applying this technique, the amplifier should be designed to have low-noise and a high bandwidth, in order to compensate the attenuated loop gain and bandwidth at higher frequencies caused by the varying CPE and the overcompensation of the TIA. This

proposes the challenges in amplifier design techniques. In addition, this work is aimed to validate the proposed square wave EIS; therefore, the power consumption was not considered. However, in the practically application, the power of the amplifier should be optimized.

6. Reference

[1] Z. Xiao *et al.,* "An Implantable RFID Sensor Tag toward Continuous Glucose Monitoring," *IEEE journal of biomedical and health informatics*, vol. 19, no. 3, pp. 910–919, 2015, doi: 10.1109/JBHI.2015.2415836.

[2] C. Barrett *et al.,* "Novel Surface Modified Polymer Microneedle based Biosensors for Interstitial Fluid Glucose Detection," in *2019 IEEE SENSORS*, Montreal, QC, Canada, 2019, pp. 1–4.

[3] N. Creedon, C. Robinson, E. Kennedy, and A. O. Riordan, "Agriculture 4.0: Development of Seriological on-Farm Immunosensor for Animal Health Applications," in *2019 IEEE SENSORS*, Montreal, QC, Canada, 2019, pp. 1–4.

[4] J. P. de Da Campos Costa, W. B. Bastos, P. I. Da Costa, M. A. Zaghete, E. Longo, and J. P. Carmo, "Portable Laboratory Platform With Electrochemical Biosensors for Immunodiagnostic of Hepatitis C Virus," *IEEE Sensors J.*, vol. 19, no. 22, pp. 10701–10709, 2019, doi: 10.1109/JSEN.2019.2930957.

[5] J. Baranwal, B. Barse, G. Gatto, G. Broncova, and A. Kumar, "Electrochemical Sensors and Their Applications: A Review," *Chemosensors*, vol. 10, no. 9, p. 363, 2022, doi: 10.3390/chemosensors10090363.

[6] D. F. Katowah, G. I. Mohammed, D. A. Al-Eryani, T. R. Sobahi, and M. A. Hussein, "Rapid and sensitive electrochemical sensor of cross-linked polyaniline/oxidized carbon nanomaterials core-shell nanocomposites for determination of 2,4-dichlorophenol," *PloS one*, vol. 15, no. 6, e0234815, 2020, doi: 10.1371/journal.pone.0234815.

[7] H. S. Stevenson, S. S. Shetty, N. J. Thomas, V. N. Dhamu, A. Bhide, and S. Prasad, "Ultrasensitive and Rapid-Response Sensor for the Electrochemical Detection of Antibiotic Residues within Meat Samples," *ACS omega*, vol. 4, no. 4, pp. 6324–6330, 2019, doi: 10.1021/acsomega.8b03534.

[8] J. Wang, "Electrochemical Sensing of Explosives," *Electroanalysis*, vol. 19, no. 4, pp. 415–423, 2007, doi: 10.1002/elan.200603748.

[9] F. Ponzio and G. Jonsson, "A rapid and simple method for the determination of picogram levels of serotonin in brain tissue using liquid chromatography with electrochemical detection," *Journal of neurochemistry*, vol. 32, no. 1, pp. 129–132, 1979, doi: 10.1111/j.1471-4159.1979.tb04519.x.

[10] G. Hanrahan, D. G. Patil, and J. Wang, "Electrochemical sensors for environmental monitoring: design, development and applications," *Journal of environmental monitoring : JEM*, vol. 6, no. 8, pp. 657–664, 2004, doi: 10.1039/B403975K.

[11] W.-D. Huang, S. Deb, Y.-S. Seo, S. Rao, M. Chiao, and J. C. Chiao, "A Passive Radio-Frequency pH-Sensing Tag for Wireless Food-Quality Monitoring," *IEEE Sensors J.*, vol. 12, no. 3, pp. 487–495, 2012, doi: 10.1109/JSEN.2011.2107738.

[12] X. Yu *et al.,* "An impedance array biosensor for detection of multiple antibody-antigen interactions," *The Analyst*, vol. 131, no. 6, pp. 745–750, 2006, doi: 10.1039/B517148B.

[13] K. M. Al-Qaoud *et al.,* "The development of an electrochemical immunosensor utilizing chicken IgY anti-spike antibody for the detection of SARS-CoV-2," *Scientific reports*, vol. 14, no. 1, p. 748, 2024, doi: 10.1038/s41598-023-50501-w.

[14] J.-Y. Park and S.-M. Park, "DNA hybridization sensors based on electrochemical impedance spectroscopy as a detection tool," *Sensors (Basel, Switzerland)*, vol. 9, no. 12, pp. 9513–9532, 2009, doi: 10.3390/s91209513.

[15] F. Asphahani and M. Zhang, "Cellular impedance biosensors for drug screening and toxin detection," *The Analyst*, vol. 132, no. 9, pp. 835–841, 2007, doi: 10.1039/B704513A.

[16] R. Ehret, W. Baumann, M. Brischwein, A. Schwinde, K. Stegbauer, and B. Wolf, "Monitoring of cellular behaviour by impedance measurements on interdigitated electrode structures," *Biosensors & bioelectronics*, vol. 12, no. 1, pp. 29–41, 1997, doi: 10.1016/0956-5663(96)89087-7.

[17] M. Arabnejad, I. E. Tothill, and I. Chianella, "Impedimetric Biosensors for the Quantification of Serum Biomarkers for Early Detection of Lung Cancer," *Biosensors*, vol. 14, no. 12, 2024, doi: 10.3390/bios14120624.

[18] I. A. Nemeir, L. Mouawad, J. Saab, W. Hleihel, A. Errachid, and N. Zine, "Electrochemical Impedance Spectroscopy Characterization of Label-Free Biosensors for the Detection of HER2 in Saliva," in *The 1st International Electronic Conference on Biosensors*, 2020, p. 17.

[19] Z. Lu *et al.,* "A point of care electrochemical impedance spectroscopy device," in *2015 28th IEEE International System-on-Chip Conference (SOCC)*, Beijing, China, 2015, pp. 240–244.

[20] Y.-R. Wang, S. C. Chien, Y. C. Lin, and J.-C. Chen, "Portable Electrochemical Impedance Spectroscopy Device Implementation for Alzheimer's Disease-Related

Protein," *Meet. Abstr.*, MA2023-01, no. 34, p. 1892, 2023, doi: 10.1149/MA2023-01341892mtgabs.

[21] I. Mostafa and R. Brederlow, "Trends, Challenges, and Recent Advances in Electrochemical Impedance Spectroscopy," *IEEE Sens. Lett.*, vol. 6, no. 5, pp. 1–4, 2022, doi: 10.1109/LSENS.2022.3162773.

[22] M. Haberler, I. Siegl, C. Steffan, and M. Auer, "A Bidirectional Current-Mirror-Based Potentiostat Using a Slice-Based Class-AB Amplifier," *IEEE Solid-State Circuits Lett.*, vol. 3, pp. 298–301, 2020, doi: 10.1109/LSSC.2020.3013667.

[23] N. T. Kemp, "A Tutorial on Electrochemical Impedance Spectroscopy and Nanogap Electrodes for Biosensing Applications," *IEEE Sensors J.*, vol. 21, no. 20, pp. 22232–22245, 2021, doi: 10.1109/JSEN.2021.3084284.

[24] A. K. P. Souza, C. A. de Moraes Cruz, G. C. Marques, L. S. O. de Castro, and T. B. Bezerra, "A Compact Current Conveyor CMOS Potentiostat Circuit for Electrochemical Sensors," in *2019 4th International Symposium on Instrumentation Systems, Circuits and Transducers (INSCIT)*, Sao Paulo, Brazil, 2019, pp. 1–6.

[25] J.-H. Tsai, Y.-C. Chen, and Y.-T. Liao, "A Power-efficient Bidirectional Potentiostat-based Readout IC for Wide-range Electrochemical Sensing," in *2018 IEEE International Symposium on Circuits and Systems (ISCAS)*, Florence, 2018, pp. 1–5.

[26] Z. Wang, A. Murphy, A. O'Riordan, and I. O'Connell, "Equivalent Impedance Models for Electrochemical Nanosensor-Based Integrated System Design," *Sensors (Basel, Switzerland)*, vol. 21, no. 9, 2021, doi: 10.3390/s21093259.

[27] *AD5933 Datasheet and Product Info | Analog Devices.* [Online]. Available: https://www.analog.com/en/products/ad5933.html (accessed: Mar. 21 2025).

[28] M. ElAnsary *et al.,* "50nW Opamp-Less ΔΣ-Modulated Bioimpedance Spectrum Analyzer for Electrochemical Brain Interfacing," *IEEE J. Solid-State Circuits*, vol. 55, no. 7, pp. 1971–1983, 2020, doi: 10.1109/JSSC.2020.2981033.

[29] H. Mazhab-Jafari, L. Soleymani, and R. Genov, "16-channel CMOS impedance spectroscopy DNA analyzer with dual-slope multiplying ADCs," *IEEE transactions on biomedical circuits and systems*, vol. 6, no. 5, pp. 468–478, 2012, doi: 10.1109/TBCAS.2012.2226334.

[30] A. D. F. Schrunder, Y.-K. Huang, S. Rodriguez, and A. Rusu, "A Bioimpedance Spectroscopy Interface for EIM Based on IF-Sampling and Pseudo 2-Path SC Bandpass ΔΣ ADC," *IEEE transactions on biomedical circuits and systems*, vol. 18, no. 5, pp. 1001–1013, 2024, doi: 10.1109/TBCAS.2024.3370399.

[31] C. Yang, S. R. Jadhav, R. M. Worden, and A. J. Mason, "Compact Low-Power Impedance-to-Digital Converter for Sensor Array Microsystems," *IEEE J. Solid-State Circuits*, vol. 44, no. 10, pp. 2844–2855, 2009, doi: 10.1109/JSSC.2009.2028054.

[32] O. Alao and P. Barendse, "Online Condition Monitoring of Sealed Lead Acid & Lithium Nickel-Cobalt-Manganese Oxide Batteries using Broadband Impedance Spectroscopy," in *2018 IEEE Energy Conversion Congress and Exposition (ECCE)*, Portland, OR, USA, 2018, pp. 2026–2032.

[33] A. de Angelis, E. Buchicchio, F. Santoni, A. Moschitta, and P. Carbone, "Uncertainty Characterization of a Practical System for Broadband Measurement of Battery EIS," *IEEE Trans. Instrum. Meas.*, vol. 71, pp. 1–9, 2022, doi: 10.1109/TIM.2022.3156994.

[34] S. Majzoub, A. Allagui, and A. S. Elwakil, "Fast Spectral Impedance Measurement Method Using a Structured Random Excitation," *IEEE Sensors J.*, vol. 20, no. 15, pp. 8637–8642, 2020, doi: 10.1109/JSEN.2020.2984005.

[35] R. S. Robinson, "System noise as a signal source for impedance measurements on batteries connected to operating equipment," *Journal of Power Sources*, vol. 42, no. 3, pp. 381–388, 1993, doi: 10.1016/0378-7753(93)90005-L.

[36] J. Sihvo, D.-I. Stroe, T. Messo, and T. Roinila, "Fast Approach for Battery Impedance Identification Using Pseudo-Random Sequence Signals," *IEEE Trans. Power Electron.*, vol. 35, no. 3, pp. 2548–2557, 2020, doi: 10.1109/TPEL.2019.2924286.

[37] X. Wang *et al.,* "Online Detection of Lithium Plating Onset for Lithium-Ion Batteries Based on Impedance Changing Trend Identification During Charging Processes," *IEEE Trans. Transp. Electrific.*, vol. 9, no. 2, pp. 3487–3497, 2023, doi: 10.1109/TTE.2022.3224965.

[38] Detective store - spy equipment and surveillance gear, *Home breathalyzer PRO X-5+*. [Online]. Available: https://www.detective-store.com/home-electrochemical-breathalyzer-pro-x-5-634.html (accessed: Mar. 16 2025).

[39] Screwfix.ie, *Kidde K4MCO Mains Interlinked Carbon Monoxide Alarm - Screwfix.* [Online]. Available: https://www.screwfix.ie/p/kidde-k4mco-mains-interlinked-carbon-monoxide-alarm/180ku (accessed: Mar. 6 2025).

[40] M. Penza, D. Suriano, M. G. Villani, L. Spinelle, and M. Gerboles, "Towards air quality indices in smart cities by calibrated low-cost sensors applied to networks," in *IEEE SENSORS 2014 Proceedings*, Valencia, Spain, 2014, pp. 2012–2017.

[41] L. A. Wasiewska *et al.,* "Reagent free electrochemical-based detection of silver ions at interdigitated microelectrodes using in-situ pH control," *Sensors and Actuators B: Chemical*, vol. 333, p. 129531, 2021, doi: 10.1016/j.snb.2021.129531.

[42] L. A. Wasiewska, F. G. Diaz, H. Shao, C. M. Burgess, G. Duffy, and A. O'Riordan, "Highly sensitive electrochemical sensor for the detection of Shiga toxin-producing E. coli (STEC) using interdigitated micro-electrodes selectively modified with a chitosan-gold nanocomposite," *Electrochimica Acta*, vol. 426, p. 140748, 2022, doi: 10.1016/j.electacta.2022.140748.

[43] A. Wahl, S. Barry, K. Dawson, J. MacHale, A. J. Quinn, and A. O'Riordan, "Electroanalysis at Ultramicro and Nanoscale Electrodes: A Comparative Study," *J. Electrochem. Soc.*, vol. 161, no. 2, B3055-B3060, 2014, doi: 10.1149/2.010402jes.

[44] A. A. Arrocha-Arcos, R. Cervantes-Alcalá, G. A. Huerta-Miranda, and M. Miranda-Hernández, "Electrochemical reduction of Bicarbonate to Formate with Silver Nanoparticles and Silver Nanoclusters supported on Multiwalled Carbon Nanotubes," *Electrochimica Acta*, vol. 246, pp. 1082–1087, 2017, doi: 10.1016/j.electacta.2017.06.147.

[45] F. van Rossem *et al.,* "Sensing oxygen at the millisecond time-scale using an ultra-microelectrode array (UMEA)," *Sensors and Actuators B: Chemical*, vol. 238, pp. 1008–1016, 2017, doi: 10.1016/j.snb.2016.06.156.

[46] P. Ramnani, N. M. Saucedo, and A. Mulchandani, "Carbon nanomaterial-based electrochemical biosensors for label-free sensing of environmental pollutants," *Chemosphere*, vol. 143, pp. 85–98, 2016, doi: 10.1016/j.chemosphere.2015.04.063.

[47] K. Dawson *et al.,* "Fully integrated on-chip nano-electrochemical devices for electroanalytical applications," *Electrochimica Acta*, vol. 115, pp. 239–246, 2014, doi: 10.1016/j.electacta.2013.10.144.

[48] F. J. Vidal-Iglesias, J. Solla-Gullón, A. Rodes, E. Herrero, and A. Aldaz, "Understanding the Nernst Equation and Other Electrochemical Concepts: An Easy Experimental Approach for Students," *J. Chem. Educ.*, vol. 89, no. 7, pp. 936–939, 2012, doi: 10.1021/ed2007179.

[49] A.-S. Feiner and A. J. McEvoy, "The Nernst Equation," *J. Chem. Educ.*, vol. 71, no. 6, p. 493, 1994, doi: 10.1021/ed071p493.

[50] J. Roscher and R. Holze, "Reference Electrodes," *Encyclopedia*, vol. 3, no. 2, pp. 478–489, 2023, doi: 10.3390/encyclopedia3020033.

[51] A. J. Bard, L. R. Faulkner, and H. S. White, *Electrochemical methods: Fundamentals and applications*. Hoboken NJ: Wiley, 2022.

[52] N. Elgrishi, K. J. Rountree, B. D. McCarthy, E. S. Rountree, T. T. Eisenhart, and J. L. Dempsey, "A Practical Beginner's Guide to Cyclic Voltammetry," *J. Chem. Educ.*, vol. 95, no. 2, pp. 197–206, 2018, doi: 10.1021/acs.jchemed.7b00361.

[53] H. YAMADA, K. YOSHII, M. ASAHI, M. CHIKU, and Y. KITAZUMI, "Cyclic Voltammetry Part 1: Fundamentals," *Electrochemistry*, vol. 90, no. 10, p. 102005, 2022, doi: 10.5796/electrochemistry.22-66082.

[54] H. YAMADA, K. YOSHII, M. ASAHI, M. CHIKU, and Y. KITAZUMI, "Cyclic Voltammetry Part 2: Surface Adsorption, Electric Double Layer, and Diffusion Layer," *Electrochemistry*, vol. 90, no. 10, p. 102006, 2022, doi: 10.5796/electrochemistry.22-66084.

[55] O. A. González-Meza, E. R. Larios-Durán, A. Gutiérrez-Becerra, N. Casillas, J. I. Escalante, and M. Bárcena-Soto, "Development of a Randles-Ševčík-like equation to predict the peak current of cyclic voltammetry for solid metal hexacyanoferrates," *J Solid State Electrochem*, vol. 23, no. 11, pp. 3123–3133, 2019, doi: 10.1007/s10008-019-04410-6.

[56] R. S. Nicholson and I. Shain, "Theory of Stationary Electrode Polarography. Single Scan and Cyclic Methods Applied to Reversible, Irreversible, and Kinetic Systems," *Anal. Chem.*, vol. 36, no. 4, pp. 706–723, 1964, doi: 10.1021/ac60210a007.

[57] J. E. B. Randles, "Kinetics of rapid electrode reactions," *Discuss. Faraday Soc.*, vol. 1, p. 11, 1947, doi: 10.1039/df9470100011.

[58] A. Ševčík, "Oscillographic polarography with periodical triangular voltage," *Collect. Czech. Chem. Commun.*, vol. 13, pp. 349–377, 1948, doi: 10.1135/cccc19480349.

[59] F. G. Cottrell, "Der Reststrom bei galvanischer Polarisation, betrachtet als ein Diffusionsproblem," *Zeitschrift für Physikalische Chemie*, 42U, no. 1, pp. 385–431, 1903, doi: 10.1515/zpch-1903-4229.

[60] J. Gu, H. Yao, K. Wang, B. Parviz, and B. Otis, "A 10μA on-chip electrochemical impedance spectroscopy system for wearables/implantables," in *2014 IEEE Asian Solid-State Circuits Conference (A-SSCC)*, KaoHsiung, Taiwan, 2014, pp. 309–312.

[61] A. C. Lazanas and M. I. Prodromidis, "Electrochemical Impedance Spectroscopy-A Tutorial," *ACS measurement science au*, vol. 3, no. 3, pp. 162–193, 2023, doi: 10.1021/acsmeasuresciau.2c00070.

[62] M. Dunwell, Y. Yan, and B. Xu, "Understanding the influence of the electrochemical double-layer on heterogeneous electrochemical reactions," *Current Opinion in Chemical Engineering*, vol. 20, pp. 151–158, 2018, doi: 10.1016/j.coche.2018.05.003.

[63] "VI. Experimental researches in electricity.-Seventh Series," *Phil. Trans. R. Soc.*, vol. 124, pp. 77–122, 1834, doi: 10.1098/rstl.1834.0008.

[64] R. G. Ehl and A. J. Ihde, "Faraday's electrochemical laws and the determination of equivalent weights," *J. Chem. Educ.*, vol. 31, no. 5, p. 226, 1954, doi: 10.1021/ed031p226.

[65] D. M. G. Preethichandra and P. Sonar, "Electrochemical Impedance Spectroscopy and its Applications in Sensor Development and Measuring Battery Performance," *IEEE Sensors J.*, vol. 22, no. 11, pp. 10152–10162, 2022, doi: 10.1109/JSEN.2021.3119650.

[66] J. S. Meráz, F. Fernández, and L. F. Magaña, "A Method for the Measurement of the Resistance of Electrolytic Solutions," *J. Electrochem. Soc.*, vol. 152, no. 4, E135, 2005, doi: 10.1149/1.1867612.

[67] L. Su, X. Liao, and Z. Huang, "A theoretical study on resistance of electrolytic solution: Measurement of electrolytic conductivity," *Results in Physics*, vol. 13, p. 102274, 2019, doi: 10.1016/j.rinp.2019.102274.

[68] M. M. Ahmadi and G. A. Jullien, "A wireless-implantable microsystem for continuous blood glucose monitoring," *IEEE transactions on biomedical circuits and systems*, vol. 3, no. 3, pp. 169–180, 2009, doi: 10.1109/TBCAS.2009.2016844.

[69] S. M. M. Alavi, A. Mahdi, S. J. Payne, and D. A. Howey, "Identifiability of Generalized Randles Circuit Models," *IEEE Trans. Contr. Syst. Technol.*, vol. 25, no. 6, pp. 2112–2120, 2017, doi: 10.1109/TCST.2016.2635582.

[70] H. M. Jafari and R. Genov, "Bidirectional current conveyer with chopper stabilization and dynamic element matching," in *2012 IEEE International Symposium on Circuits and Systems*, Seoul, Korea (South), 2012, pp. 1079–1082.

[71] H. M. Jafari and R. Genov, "Chopper-Stabilized Bidirectional Current Acquisition Circuits for Electrochemical Amperometric Biosensors," *IEEE Trans. Circuits Syst. I*, vol. 60, no. 5, pp. 1149–1157, 2013, doi: 10.1109/TCSI.2013.2248771.

[72] K. A. A. Mamun and N. McFarlane, "A CMOS potentiostatic glucose monitoring system for VACNF amperometric biosensors," in *2015 IEEE International Symposium on Circuits and Systems (ISCAS)*, Lisbon, Portugal, 2015, pp. 477–480.

[73] S. Sutula, J. Pallares Cuxart, J. Gonzalo-Ruiz, F. X. Munoz-Pascual, L. Teres, and F. Serra-Graells, "A 25-µW All-MOS Potentiostatic Delta-Sigma ADC for Smart Electrochemical Sensors," *IEEE Trans. Circuits Syst. I*, vol. 61, no. 3, pp. 671–679, 2014, doi: 10.1109/TCSI.2013.2284179.

[74] H. Yin, E. Ashoori, X. Mu, and A. J. Mason, "A Compact Low-Power Current-to-Digital Readout Circuit for Amperometric Electrochemical Sensors," *IEEE Trans. Instrum. Meas.*, vol. 69, no. 5, pp. 1972–1980, 2020, doi: 10.1109/tim.2019.2922053.

[75] K. Darowicki and L. Gawel, "Impedance Measurement and Selection of Electrochemical Equivalent Circuit of a Working PEM Fuel Cell Cathode," *Electrocatalysis*, vol. 8, no. 3, pp. 235–244, 2017, doi: 10.1007/s12678-017-0363-0.

[76] R. N. Vyas, K. Li, and B. Wang, "Modifying Randles circuit for analysis of polyoxometalate layer-by-layer films," *The journal of physical chemistry. B*, vol. 114, no. 48, pp. 15818–15824, 2010, doi: 10.1021/jp105075t.

[77] R. N. Vyas and B. Wang, "Electrochemical analysis of conducting polymer thin films," *International journal of molecular sciences*, vol. 11, no. 4, pp. 1956–1972, 2010, doi: 10.3390/ijms11041956.

[78] K. Nam, G. Choi, H. Kim, M. Yoo, and H. Ko, "A Potentiostat Readout Circuit with a Low-Noise and Mismatch-Tolerant Current Mirror Using Chopper Stabilization and Dynamic Element Matching for Electrochemical Sensors," *Applied Sciences*, vol. 11, no. 18, p. 8287, 2021, doi: 10.3390/app11188287.

[79] Z. Wang, H. Shao, A. O'Riordan, J. Higes-Marquez, I. O'Connell, and D. O'Hare, "A Fast Square Wave-based Electrochemical Impedance Spectroscopy for Impedance-based Biomedical Applications," in *2024 IEEE Biomedical Circuits and Systems Conference (BioCAS)*, Xi'an, China, 2024, pp. 1–5.

[80] N. Creedon, R. sayers, B. O'sullivan, E. Kennedy, P. Lovera, and A. O'Riordan, *Label-Free Impedimetric Nanoband Sensor for Detection of Both Bovine Viral Diarrhoea Virus (BVDV) and Antibody (BVDAb) in Serum*, 2018.

[81] P. M. Levine, P. Gong, R. Levicky, and K. L. Shepard, "Active CMOS Sensor Array for Electrochemical Biomolecular Detection," *IEEE J. Solid-State Circuits*, vol. 43, no. 8, pp. 1859–1871, 2008, doi: 10.1109/JSSC.2008.925407.

[82] P. G. A. Jespers and B. Murmann, *Systematic Design of Analog CMOS Circuits*: Cambridge University Press, 2017.

[83] M. M. Ahmadi and G. A. Jullien, "Current-Mirror-Based Potentiostats for Three-Electrode Amperometric Electrochemical Sensors," *IEEE Trans. Circuits Syst. I*, vol. 56, no. 7, pp. 1339–1348, 2009, doi: 10.1109/TCSI.2008.2005927.

[84] R. Turner, D. J. Harrison, and H. P. Baltes, "A CMOS potentiostat for amperometric chemical sensors," *IEEE J. Solid-State Circuits*, vol. 22, no. 3, pp. 473–478, 1987, doi: 10.1109/JSSC.1987.1052753.

[85] Q. Zhu *et al.,* "Electrochemical preparation of polyaniline capped Bi2S3 nanocomposite and its application in impedimetric DNA biosensor," *Sensors and Actuators B: Chemical*, vol. 207, pp. 819–826, 2015, doi: 10.1016/j.snb.2014.10.120.

[86] W. M. Hassen, V. Duplan, E. Frost, and J. J. Dubowski, "Quantitation of influenza A virus in the presence of extraneous protein using electrochemical impedance spectroscopy," *Electrochimica Acta*, vol. 56, no. 24, pp. 8325–8328, 2011, doi: 10.1016/j.electacta.2011.07.009.

[87] R. K. Shervedani, A. H. Mehrjardi, and N. Zamiri, "A novel method for glucose determination based on electrochemical impedance spectroscopy using glucose oxidase self-assembled biosensor," *Bioelectrochemistry (Amsterdam, Netherlands)*, vol. 69, no. 2, pp. 201–208, 2006, doi: 10.1016/j.bioelechem.2006.01.003.

[88] T.-A. Chen, W.-J. Wu, C.-L. Wei, R. B. Darling, and B.-D. Liu, "Novel 10-Bit Impedance-to-Digital Converter for Electrochemical Impedance Spectroscopy Measurements," *IEEE transactions on biomedical circuits and systems*, vol. 11, no. 2, pp. 370–379, 2017, doi: 10.1109/TBCAS.2016.2592511.

[89] J. A. A. Qahouq and Z. Xia, "Single-Perturbation-Cycle Online Battery Impedance Spectrum Measurement Method With Closed-Loop Control of Power Converter," *IEEE Trans. Ind. Electron.*, vol. 64, no. 9, pp. 7019–7029, 2017, doi: 10.1109/TIE.2017.2686324.

[90] S.-I. Cheon *et al.,* "Impedance-Readout Integrated Circuits for Electrical Impedance Spectroscopy: Methodological Review," *IEEE transactions on biomedical circuits and systems*, vol. 18, no. 1, pp. 215–232, 2024, doi: 10.1109/TBCAS.2023.3319212.

[91] S.-J. Kweon, A. K. Rafi, S.-I. Cheon, M. Je, and S. Ha, "On-Chip Sinusoidal Signal Generators for Electrical Impedance Spectroscopy: Methodological Review," *IEEE transactions on biomedical circuits and systems*, vol. 16, no. 3, pp. 337–360, 2022, doi: 10.1109/TBCAS.2022.3171163.

[92] H. Ha *et al.,* "A Bio-Impedance Readout IC With Digital-Assisted Baseline Cancellation for Two-Electrode Measurement," *IEEE J. Solid-State Circuits*, vol. 54, no. 11, pp. 2969–2979, 2019, doi: 10.1109/JSSC.2019.2939077.

[93] C. S. Park, H. Kim, K. Lee, D. S. Keum, D. P. Jang, and J. J. Kim, "A Baseline-Tracking Single-Channel I/Q Impedance Plethysmogram IC for Neckband-Based Blood Pressure and Cardiovascular Monitoring," *IEEE J. Solid-State Circuits*, vol. 58, no. 7, pp. 2040–2052, 2023, doi: 10.1109/JSSC.2022.3221478.

[94] T.-T. Zhang, H. Son, J. Zhao, C.-H. Heng, and Y. Gao, "A 26.6–119.3-μW 101.9-dB SNR Direct Digitization Bio-Impedance Readout IC," *IEEE J. Solid-State Circuits*, vol. 58, no. 9, pp. 2619–2631, 2023, doi: 10.1109/JSSC.2023.3269671.

[95] S. Subhan and S. Ha, "A Harmonic Error Cancellation Method for Accurate Clock-Based Electrochemical Impedance Spectroscopy," *IEEE transactions on biomedical circuits and systems*, vol. 13, no. 4, pp. 710–724, 2019, doi: 10.1109/TBCAS.2019.2923719.

[96] S. Lee *et al.,* "A Low-power and Compact-sized Wearable Bio-impedance Monitor with Wireless Connectivity," *J. Phys.: Conf. Ser.*, vol. 434, p. 12013, 2013, doi: 10.1088/1742-6596/434/1/012013.

[97] W. Lee and S. Cho, "Integrated All Electrical Pulse Wave Velocity and Respiration Sensors Using Bio-Impedance," *IEEE J. Solid-State Circuits*, vol. 50, no. 3, pp. 776–785, 2015, doi: 10.1109/JSSC.2014.2380781.

[98] I. Jiménez, C. Pérez-Ràfols, N. Serrano, M. Del Valle, and J. Manuel Díaz-Cruz, "Carbon based electrodes for the voltammetric determination of capsaicin in spicy samples," *Microchemical Journal*, vol. 191, p. 108757, 2023, doi: 10.1016/j.microc.2023.108757.

[99] A. Wahl, K. Dawson, J. MacHale, S. Barry, A. J. Quinn, and A. O'Riordan, "Gold nanowire electrodes in array: simulation study and experiments," *Faraday discussions*, vol. 164, pp. 377–390, 2013, doi: 10.1039/C3FD00025G.

[100] H. Jiang, X. Zhou, S. Kulkarni, M. Uranian, R. Seenivasan, and D. A. Hall, "A Sub-1 μW multiparameter injectable BioMote for continuous alcohol monitoring,"

in *2018 IEEE Custom Integrated Circuits Conference (CICC)*, San Diego, CA, 2018, pp. 1–4.

[101] P. Vanýsek, *Modern techniques in electroanalysis*. New York: Wiley, 1996.

[102] M. J. A. Shiddiky, A. A. J. Torriero, J. M. Reyna-González, and A. M. Bond, "Nonadditivity of faradaic currents and modification of double layer capacitance in the voltammetry of mixtures of ferrocene and ferrocenium salts in ionic liquids," *Anal. Chem.*, vol. 82, no. 5, pp. 1680–1691, 2010, doi: 10.1021/ac9020159.

[103] I. Heller, J. Kong, H. A. Heering, K. A. Williams, S. G. Lemay, and C. Dekker, "Individual single-walled carbon nanotubes as nanoelectrodes for electrochemistry," *Nano letters*, vol. 5, no. 1, pp. 137–142, 2005, doi: 10.1021/nl048200m.

[104] R. C. Kubendran, S. Kim, and R. F. Yazicioglu, "Error correction algorithm for high accuracy bio-impedance measurement in wearable healthcare applications," in *2013 IEEE International Symposium on Circuits and Systems (ISCAS2013)*, Beijing, 2013, pp. 1292–1295.

[105] A. Lasia, "The Origin of the Constant Phase Element," *The journal of physical chemistry letters*, vol. 13, no. 2, pp. 580–589, 2022, doi: 10.1021/acs.jpclett.1c03782.

[106] M. R. Shoar Abouzari, F. Berkemeier, G. Schmitz, and D. Wilmer, "On the physical interpretation of constant phase elements," *Solid State Ionics*, vol. 180, 14-16, pp. 922–927, 2009, doi: 10.1016/j.ssi.2009.04.002.

[107] H. Ren, Y. Zhao, S. Chen, and L. Yang, "A comparative study of lumped equivalent circuit models of a lithium battery for state of charge prediction," *Int J Energy Res*, 2019, doi: 10.1002/er.4759.

[108] T. Heil and A. Jossen, "Continuous approximation of the ZARC element with passive components," *Meas. Sci. Technol.*, vol. 32, no. 10, p. 104011, 2021, doi: 10.1088/1361-6501/ac0466.

[109] E. Kuhn, C. Forgez, P. Lagonotte, and G. Friedrich, "Modelling Ni-mH battery using Cauer and Foster structures," *Journal of Power Sources*, vol. 158, no. 2, pp. 1490–1497, 2006, doi: 10.1016/j.jpowsour.2005.10.018.

[110] Y. Hou, T. Guo, M. Bance, and C. Jiang, "A High-Precision Circuit-Simulator-Compatible Model for Constant Phase Element Using Rational Function Approximation," *IEEE J. Electron Devices Soc.*, vol. 11, pp. 726–733, 2023, doi: 10.1109/JEDS.2023.3292824.

[111] M. Berljafa and S. Güttel, "The RKFIT Algorithm for Nonlinear Rational Approximation," *SIAM J. Sci. Comput.*, vol. 39, no. 5, A2049-A2071, 2017, doi: 10.1137/15m1025426.

[112] W. Hendrickx and T. Dhaene, "A Discussion of “Rational Approximation of Frequency Domain Responses by Vector Fitting”," *IEEE Trans. Power Syst.*, vol. 21, no. 1, pp. 441–443, 2006, doi: 10.1109/TPWRS.2005.860905.

[113] D. Xue, C. Zhao, and Y. Chen, "A Modified Approximation Method of Fractional Order System," in *2006 International Conference on Mechatronics and Automation*, Luoyang, Henan, 2006, pp. 1043–1048.

[114] *NOVA.* [Online]. Available: https://www.metrohm.com/en_gb/service/software-center/nova.html (accessed: Jan. 29 2025).

[115] Y. Chao, H. Yue, B. L. Hassler, R. M. Worden, and A. J. Mason, "Amperometric electrochemical microsystem for a miniaturized protein biosensor array," *IEEE transactions on biomedical circuits and systems*, vol. 3, no. 3, pp. 160–168, 2009, doi: 10.1109/TBCAS.2009.2015650.

[116] A. Manickam, A. Chevalier, M. McDermott, A. D. Ellington, and A. Hassibi, "A CMOS Electrochemical Impedance Spectroscopy (EIS) Biosensor Array," *IEEE transactions on biomedical circuits and systems*, vol. 4, no. 6, pp. 379–390, 2010, doi: 10.1109/TBCAS.2010.2081669.

[117] A. Manickam *et al.,* "A CMOS Electrochemical Biochip With 32$\times$ 32 Three-Electrode Voltammetry Pixels," *IEEE J. Solid-State Circuits*, vol. 54, no. 11, pp. 2980–2990, 2019, doi: 10.1109/JSSC.2019.2941020.

[118] M. Schienle *et al.,* "A fully electronic DNA sensor with 128 positions and in-pixel A/D conversion," *IEEE J. Solid-State Circuits*, vol. 39, no. 12, pp. 2438–2445, 2004, doi: 10.1109/JSSC.2004.837084.

[119] D. Djekic, G. Fantner, K. Lips, M. Ortmanns, and J. Anders, "A 0.1% THD, 1-M Ω to 1-G Ω Tunable, Temperature-Compensated Transimpedance Amplifier Using a Multi-Element Pseudo-Resistor," *IEEE J. Solid-State Circuits*, vol. 53, no. 7, pp. 1913–1923, 2018, doi: 10.1109/JSSC.2018.2820701.

[120] M. Haberle, D. Djekic, G. E. Fantner, K. Lips, M. Ortmanns, and J. Anders, "An Integrator-Differentiator TIA Using a Multi-Element Pseudo-Resistor in its DC Servo Loop for Enhanced Noise Performance," in *ESSCIRC 2018 - IEEE 44th European Solid State Circuits Conference (ESSCIRC)*, Dresden, 2018, pp. 294–297.

[121] Z. Wang, A. Wall, A. O'Riordan, D. O'Hare, G. M. Salgado, and I. O'Connell, "Models and Interfaces for Electrochemical Sensors: Architectures and Implementations," in *Biomedical Electronics, Noise Shaping ADCs, and Frequency References*, P. Harpe, A. Baschirotto, and K. A. Makinwa, Eds., Cham: Springer International Publishing, 2023, pp. 79–103.

[122] M. Rajabzadeh, M. Haberle, A. Jain, and M. Ortmanns, "An Integrated Readout for Current Sensing based on a ΣΔ Modulator with Switched Capacitor Feedback," in *ESSCIRC 2019 - IEEE 45th European Solid State Circuits Conference (ESSCIRC)*, Cracow, Poland, 2019, pp. 321–324.

[123] M. A. Akram, A. Aberra, S.-J. Kweon, and S. Ha, "An Ultra-low-power Amplifier-less Potentiostat Design Based on Digital Regulation Loop," *IEEE transactions on biomedical circuits and systems*, PP, 2025, doi: 10.1109/TBCAS.2025.3527652.

[124] M. A. Akram, A. Aberra, S.-J. Kweon, and S. Ha, "3.6 An Amplifier-Less CMOS Potentiostat IC Consuming 3.7nW Power all over 129.5dB Dynamic Range for Electrochemical Biosensing," in *2024 IEEE International Solid-State Circuits Conference (ISSCC)*, San Francisco, CA, USA, 2024, pp. 64–66.

7. Appendices

7.1. MATLAB Code for Computing Impedance

```
function
[IOUT_Mag_FFT_SQ,IOUT_Pha_FFT_SQ,VIN_Mag_FFT_SQ,VIN_Pha_FFT_SQ,Z_real_SQ_SL
, Z_IMG_SQ_SL,Freq_FFT_SQ_SL,Freq_FFT_SQ]=SQEIS_Fun(TIME_RAW_SQ,
VIN_RAW_SQ, IOUT_RAW_SQ, Rs_SQ)
%CREATEFIGURE(X1, Y1, X2, Y2)function
Fig17SquareVSEISFun(TIME_RAW_squareE1, VIN_RAW_squareE1, IOUT_RAW_squareE1,
Rs_squareE1, ZRe, ZIm)

%%
Down_Sample_Factor_SQ = 1;

VIN_RAW_SAM_SQ = VIN_RAW_SQ(1:Down_Sample_Factor_SQ:end);
IOUT_RAW_SAM_SQ = IOUT_RAW_SQ(1:Down_Sample_Factor_SQ:end);
TIME_RAW_SAM_SQ = TIME_RAW_SQ(1:Down_Sample_Factor_SQ:end);

%%
Fs_SQ = 1/(TIME_RAW_SAM_SQ(2)-TIME_RAW_SAM_SQ(1));
L_SQ=length(TIME_RAW_SAM_SQ);
N_SQ=L_SQ;

VIN_FFT_SQ = fft(VIN_RAW_SAM_SQ,N_SQ)/N_SQ;
IOUT_FFT_SQ = fft(IOUT_RAW_SAM_SQ./Rs_SQ,N_SQ)/N_SQ;

VIN_FFT_SQ_oneSide = VIN_FFT_SQ(1:(N_SQ)/2);
IOUT_FFT_SQ_oneSide = IOUT_FFT_SQ(1:(N_SQ)/2);
Freq_FFT_SQ = Fs_SQ*(0:N_SQ/2-1)/N_SQ;
S1_SQ = 4;
S2_SQ = 10;
Step_SQ = S2_SQ-S1_SQ;
EndSL_SQ = 2992;

Freq_FFT_SQ_SL =
abs([Freq_FFT_SQ(S1_SQ),Freq_FFT_SQ(S2_SQ:Step_SQ:EndSL_SQ)]);


VIN_Mag_FFT_SQ = 2*abs(VIN_FFT_SQ_oneSide);
VIN_Pha_FFT_SQ = angle(VIN_FFT_SQ_oneSide);

IOUT_Mag_FFT_SQ = 2*abs(IOUT_FFT_SQ_oneSide);
IOUT_Pha_FFT_SQ = angle(IOUT_FFT_SQ_oneSide);

Z_SQ = VIN_FFT_SQ_oneSide./IOUT_FFT_SQ_oneSide;

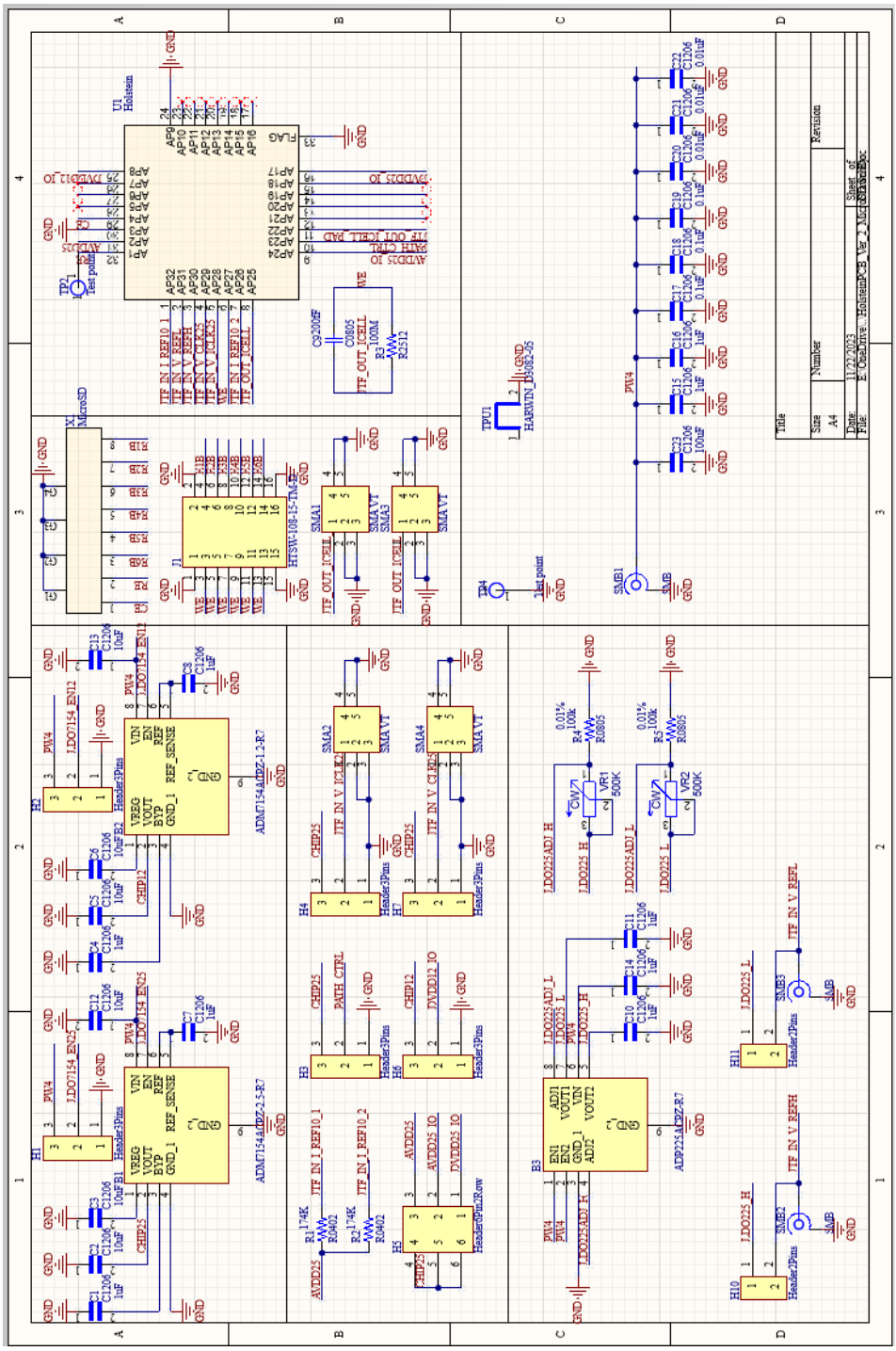
Z_img_SQ = abs(imag(Z_SQ));
Z_real_SQ = abs(real(Z_SQ));
```

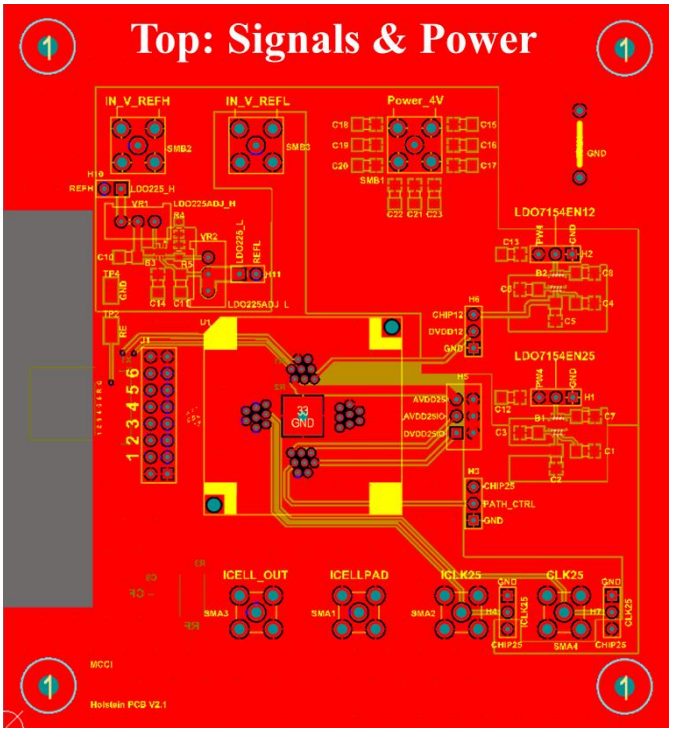
```
Z_IMG_SQ_SL = abs([Z_img_SQ(S1_SQ); Z_img_SQ(S2_SQ:Step_SQ:EndSL_SQ)]);
Z_real_SQ_SL = abs([Z_real_SQ(S1_SQ); Z_real_SQ(S2_SQ:Step_SQ:EndSL_SQ)]);

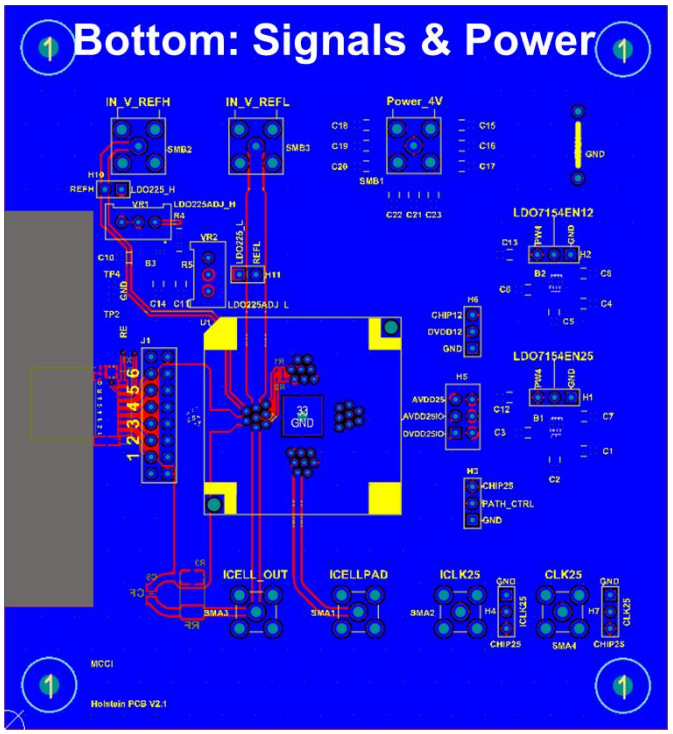
return
end
```

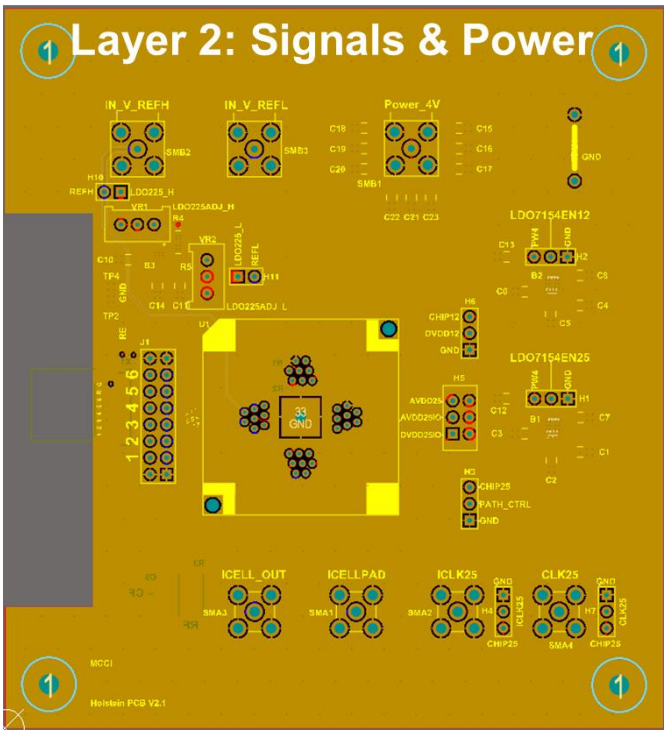
7.2. Measurement PCB Schematics and Layouts

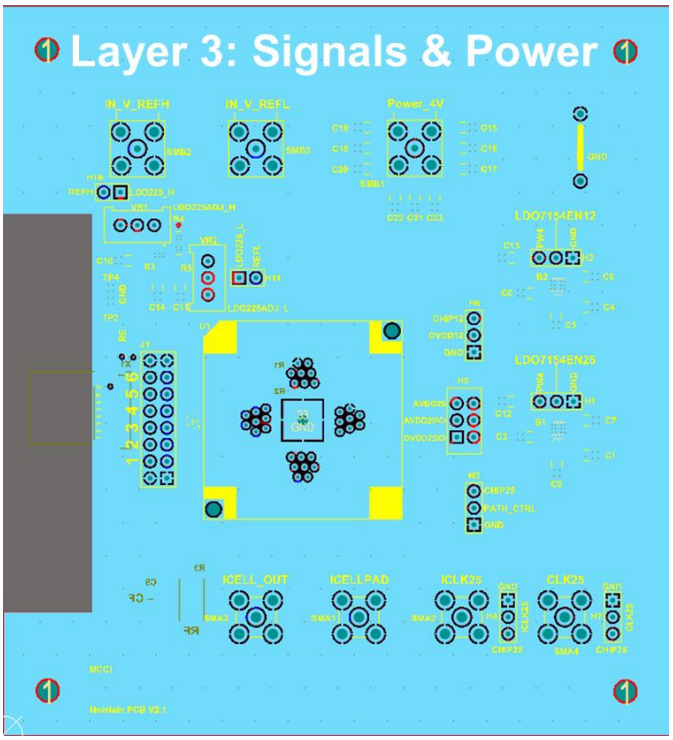
7.2.1. Chip Measurement PCB



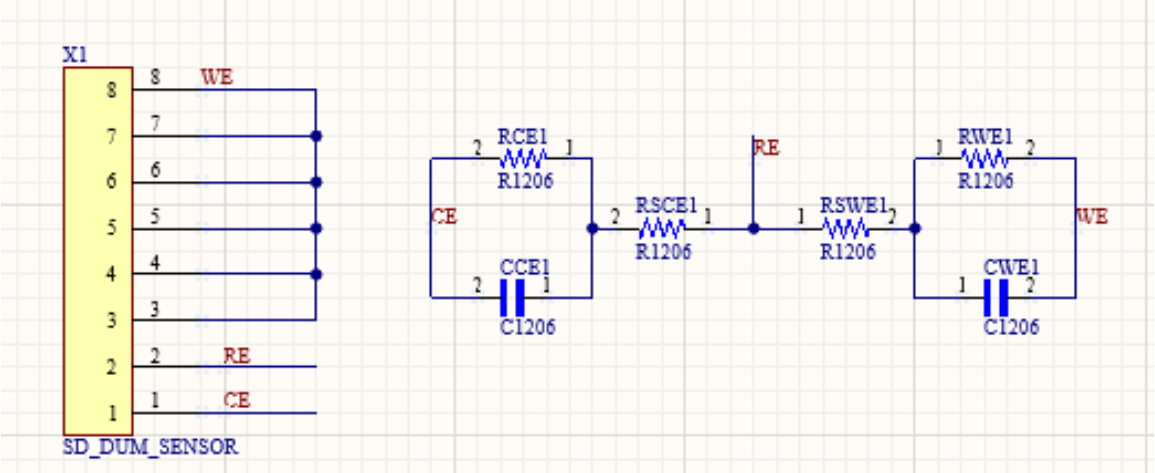

Top: Signals & Power
IN_V_REFH
IN_V_REFL
Power_4V
LDO7154EN12
LDO7154EN25
ICELL_OUT
ICELLPAD
ICLK25
CLK25
GND
MCCI
Holstein PCB V2.1

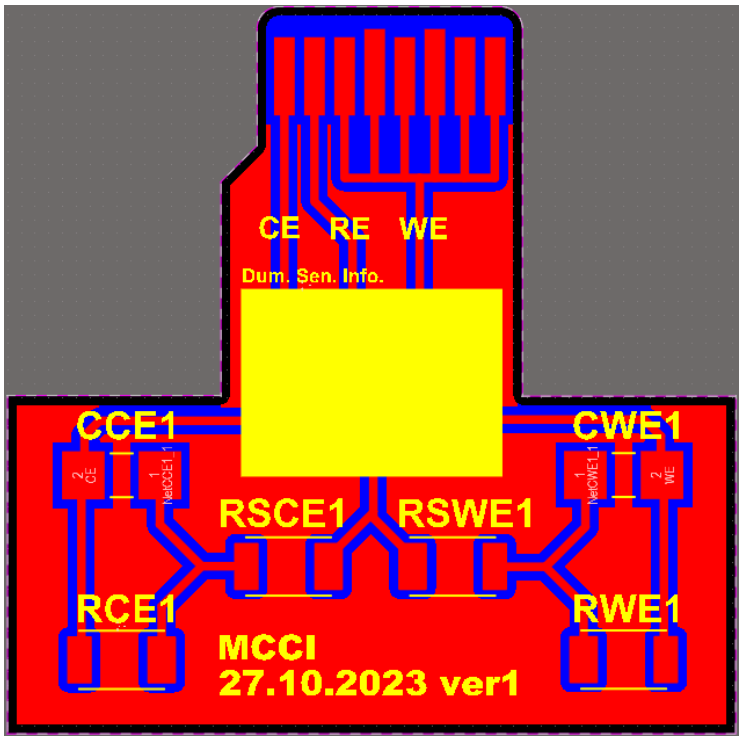

Bottom: Signals & Power
IN_V_REFH
IN_V_REFL
Power_4V
LDO7154EN12
LDO7154EN25
ICELL_OUT
ICELLPAD
ICLK25
CLK25
GND
MCCI
Holstein PCB V2.1

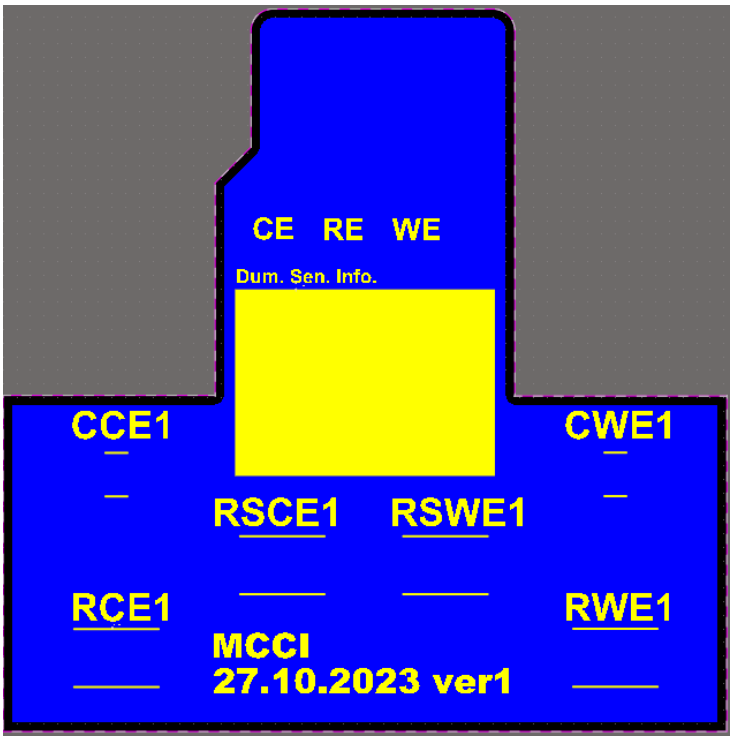

Layer 2: Signals & Power
IN_V_REFH
IN_V_REFL
Power_4V
GND
LDO7154EN12
LDO7154EN25
ICELL_OUT
ICELLPAD
ICLK25
CLK25
MCCI
Holstein PCB V2.1


Layer 3: Signals & Power
IN_V_REFH
IN_V_REFL
Power_4V
GND
LDO7154EN12
LDO7154EN25
ICELL_OUT
ICELLPAD
ICLK25
CLK25
MCCI
Holstein PCB V2.1

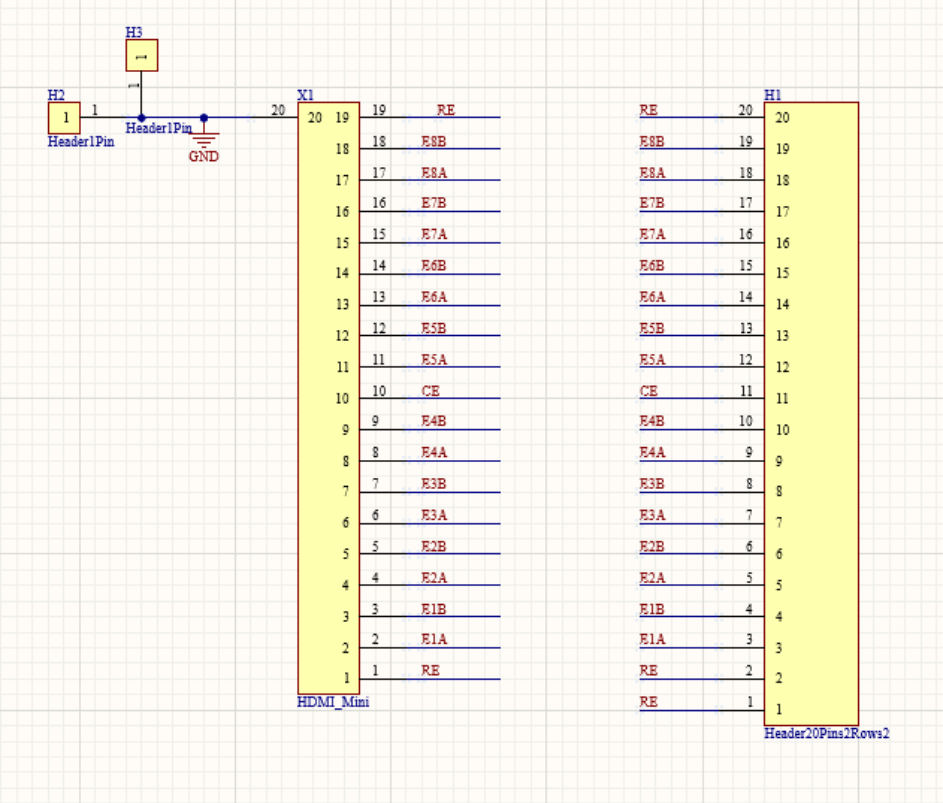
7.2.2. Dummy Sensor PCB

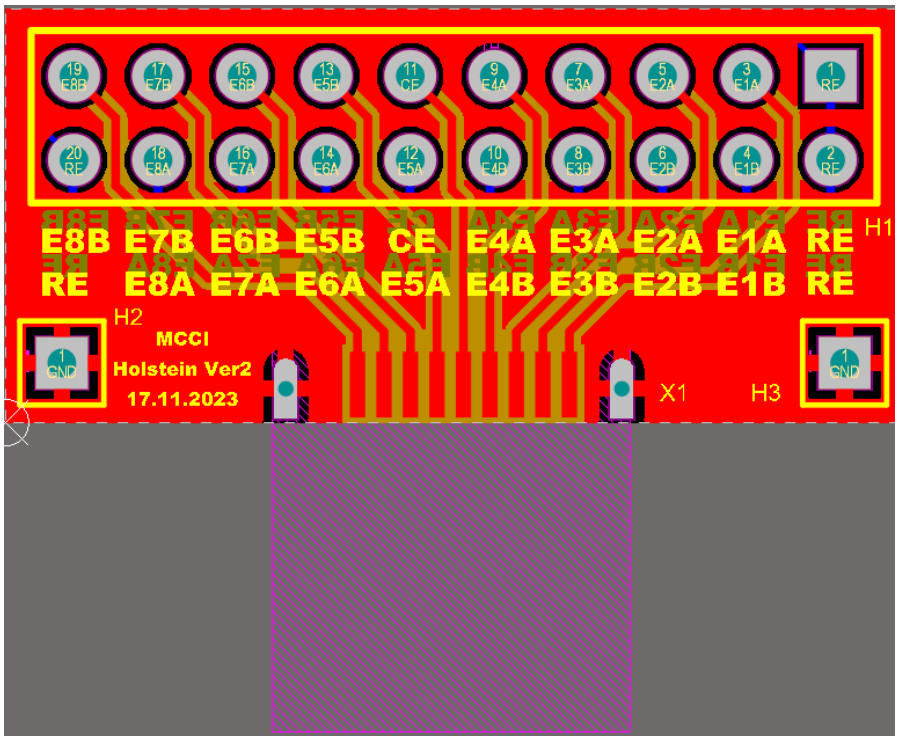


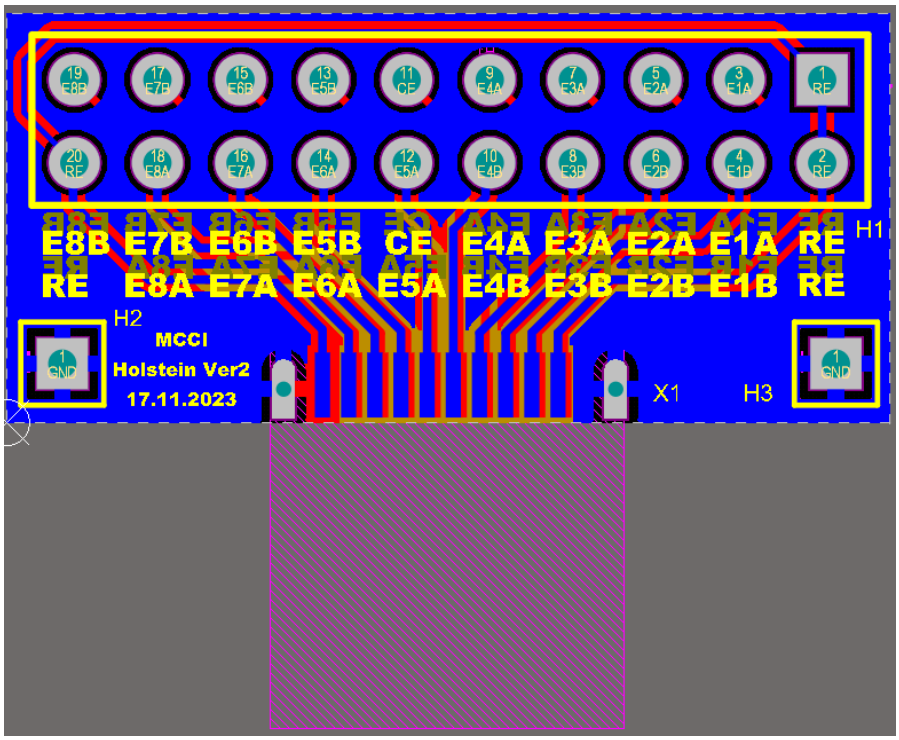

CE RE WE
Dum. Sen. Info.
CCE1
CWE1
RSCE1
RSWE1
RCE1
RWE1
MCCI
27.10.2023 ver1

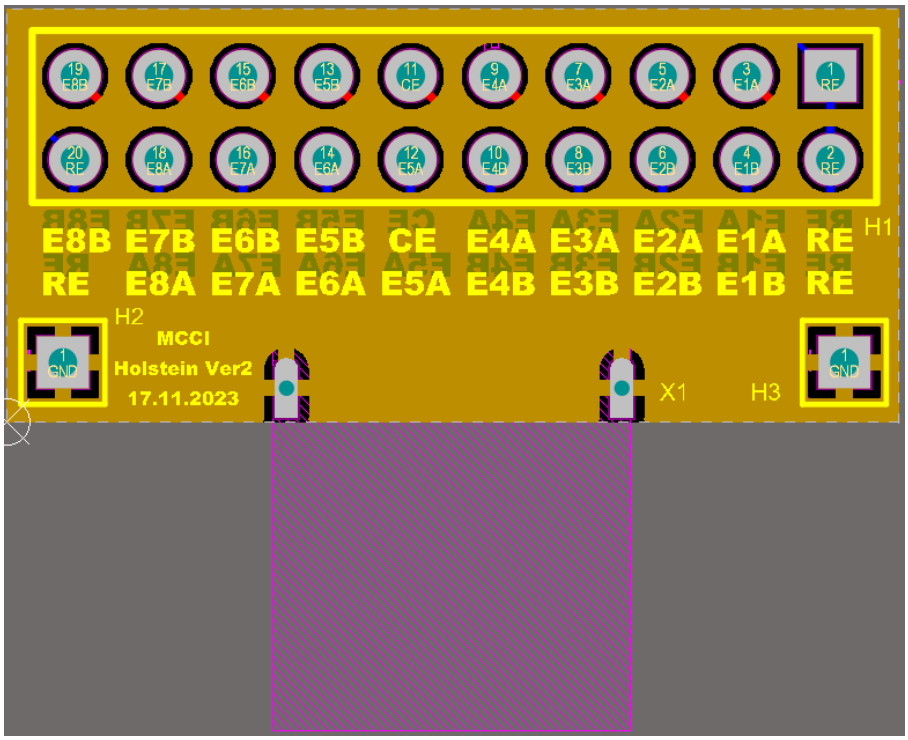

CE RE WE
Dum. Sen. Info.
CCE1
CWE1
RSCE1
RSWE1
RCE1
RWE1
MCCI
27.10.2023 ver1

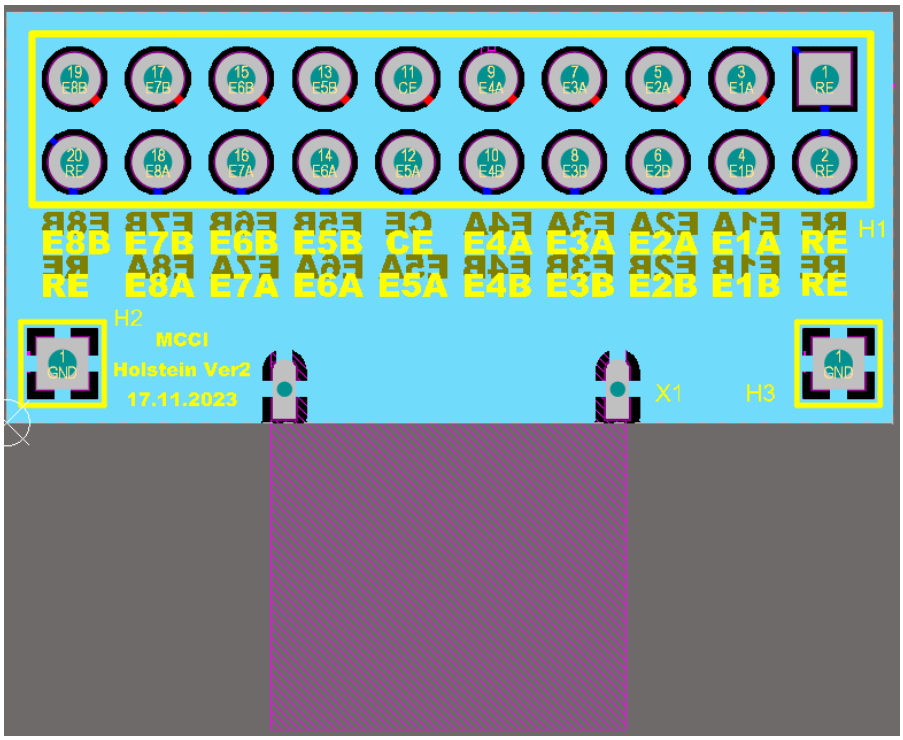
7.2.3. Mini-HDMI UMB Sensor PCB Adaptor



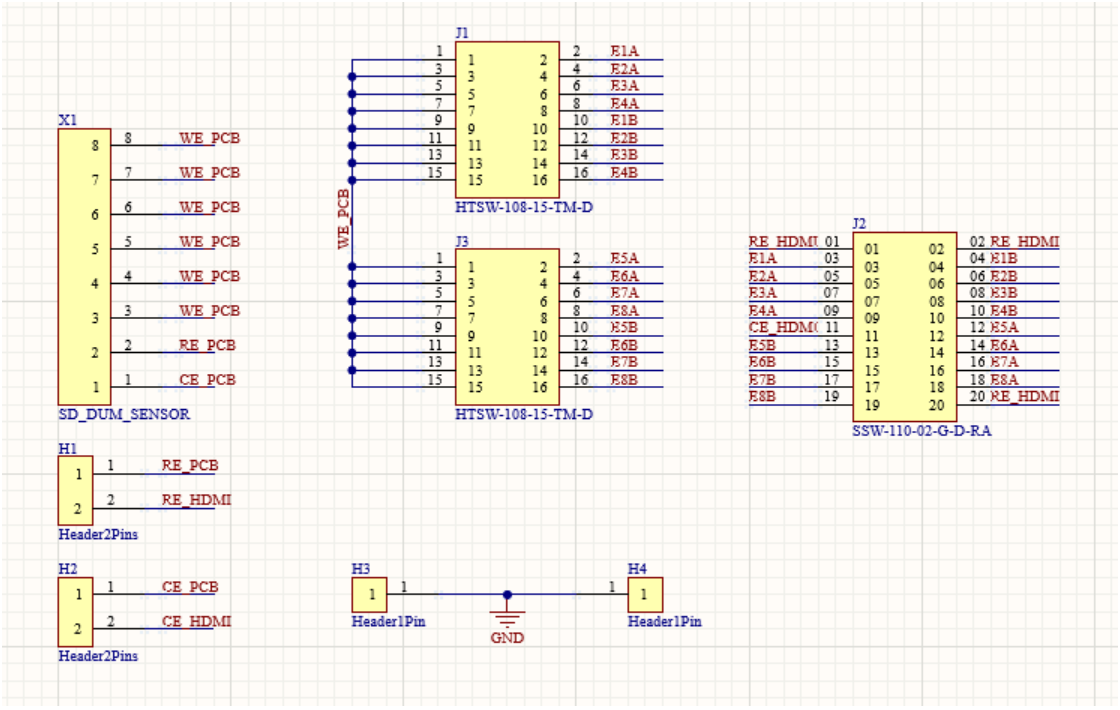

19 E8B
17 E7B
15 E6B
13 E5B
11 CE
9 E4A
7 E3A
5 E2A
3 E1A
1 RE
20 RE
18 E8A
16 E7A
14 E6A
12 E5A
10 E4B
8 E3B
6 E2B
4 E1B
2 RE
E8B E7B E6B E5B CE E4A E3A E2A E1A RE
RE E8A E7A E6A E5A E4B E3B E2B E1B RE
H1
H2
MCCI
Holstein Ver2
17.11.2023
1 GND
X1
H3
1 GND

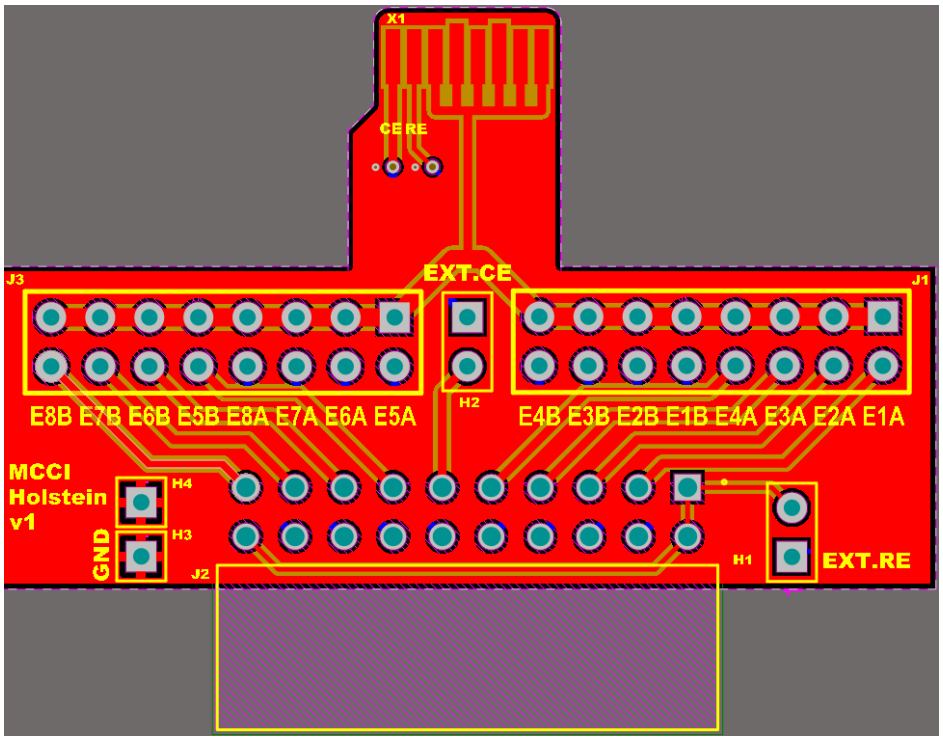

19 E8B
17 E7B
15 E6B
13 E5B
11 CE
9 E4A
7 E3A
5 E2A
3 E1A
1 RE
20 RE
18 E8A
16 E7A
14 E6A
12 E5A
10 E4B
8 E3B
6 E2B
4 E1B
2 RE
E8B E7B E6B E5B CE E4A E3A E2A E1A RE
RE E8A E7A E6A E5A E4B E3B E2B E1B RE
H1
H2
MCCI
Holstein Ver2
17.11.2023
1 GND
X1
H3
1 GND

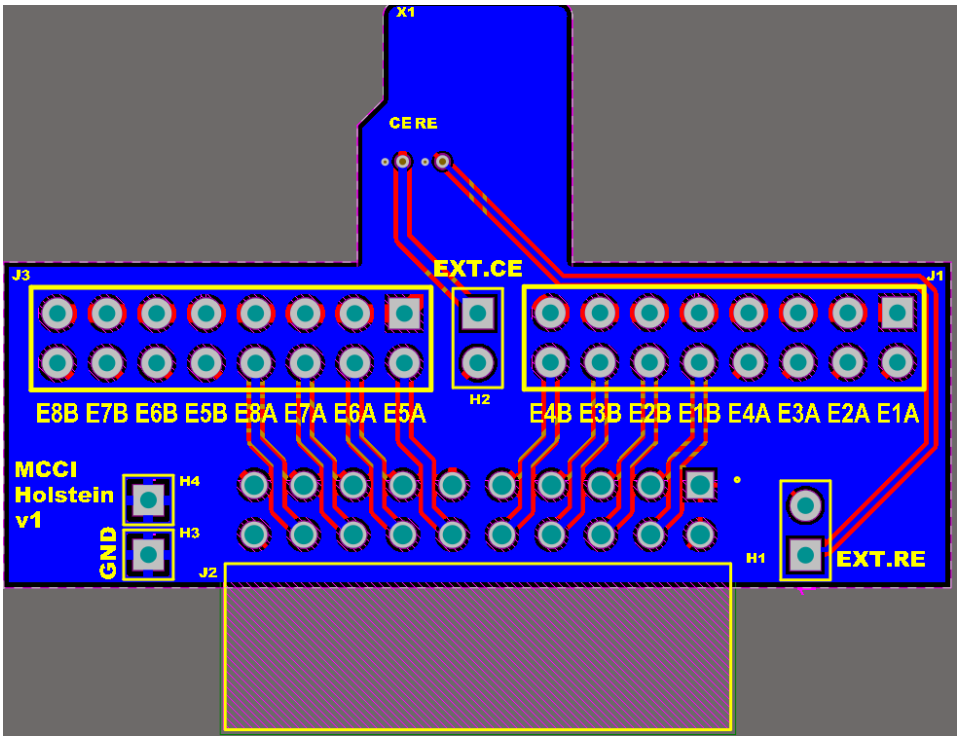

19 E8P
17 E7P
15 E6P
13 E5P
11 CE
9 E4A
7 E3A
5 E2A
3 E1A
1 RE
20 RE
18 E8A
16 E7A
14 E6A
12 E5A
10 E4B
8 E3B
6 E2B
4 E1B
2 RE
E8B E7B E6B E5B CE E4A E3A E2A E1A RE
RE E8A E7A E6A E5A E4B E3B E2B E1B RE
H1
H2
MCCI
Holstein Ver2
17.11.2023
1 GND
X1
H3
1 GND

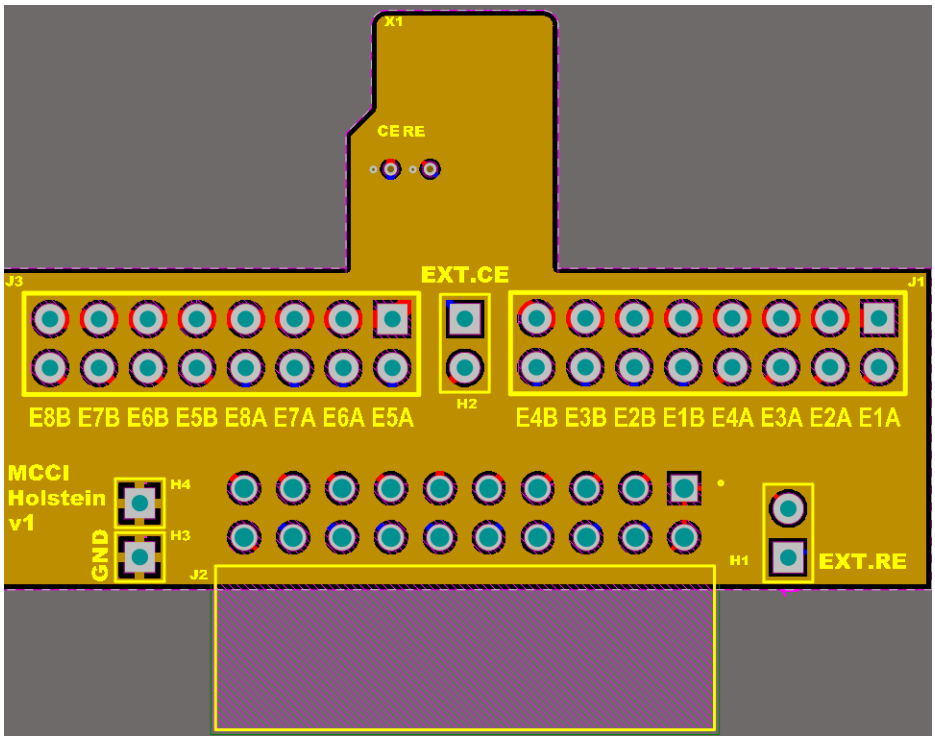

19 E8P
17 E7P
15 E6P
13 E5P
11 CE
9 E4A
7 E3A
5 E2A
3 E1A
1 RE
20 RE
18 E8A
16 E7A
14 E6A
12 E5A
10 E4B
8 E3B
6 E2B
4 E1B
2 RE
E8B E7B E6B E5B CE E4A E3A E2A E1A RE
RE E8A E7A E6A E5A E4B E3B E2B E1B RE
H1
H2
MCCI
Holstein Ver2
17.11.2023
1 GND
X1
H3
1 GND

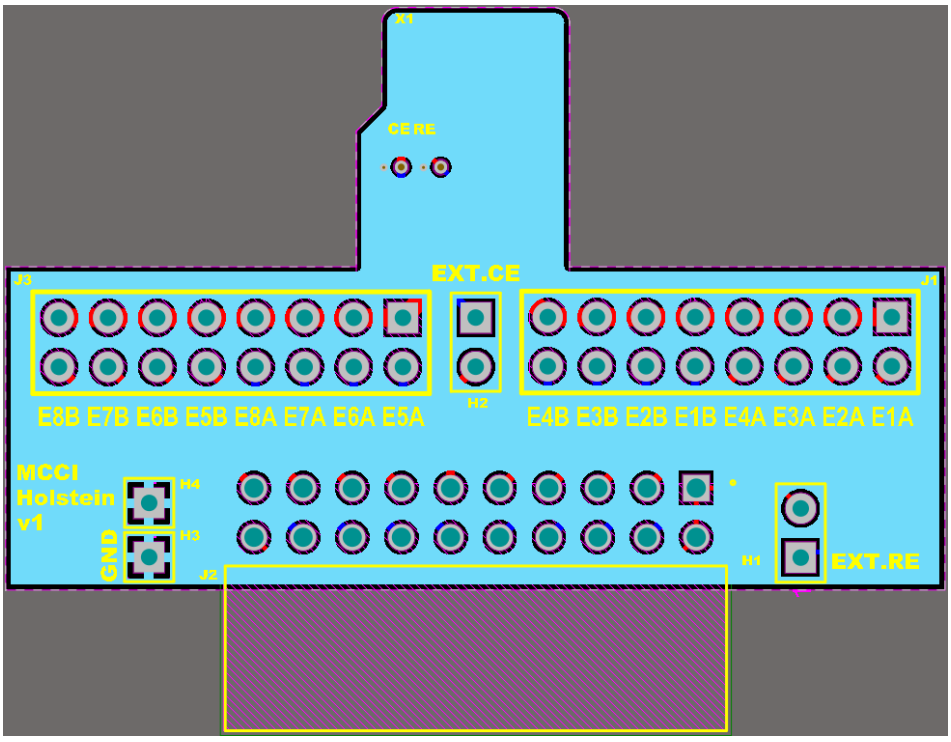
7.2.4. Mini-HDMI to Micro SD Adaptor




X1
CE RE
EXT.CE
J3
J1
H2
E8B E7B E6B E5B E8A E7A E6A E5A
E4B E3B E2B E1B E4A E3A E2A E1A
MCCI
Holstein
v1
H4
H3
GND
J2
H1
EXT.RE


X1
CE RE
EXT.CE
J3
J1
H2
E8B E7B E6B E5B E8A E7A E6A E5A
E4B E3B E2B E1B E4A E3A E2A E1A
MCCI
Holstein
v1
H4
H3
GND
J2
H1
EXT.RE


X1
CE RE
EXT.CE
J3
J1
E8B E7B E6B E5B E8A E7A E6A E5A
H2
E4B E3B E2B E1B E4A E3A E2A E1A
MCCI
Holstein
v1
H4
H3
GND
J2
H1
EXT.RE


X1
CE RE
EXT.CE
J3
J1
E8B E7B E6B E5B E8A E7A E6A E5A
H2
E4B E3B E2B E1B E4A E3A E2A E1A
MCCI
Holstein
v1
H4
H3
GND
J2
H1
EXT.RE